Carderock Division, Naval Surface Warfare Center

West Bethesda, Maryland 20817-5700
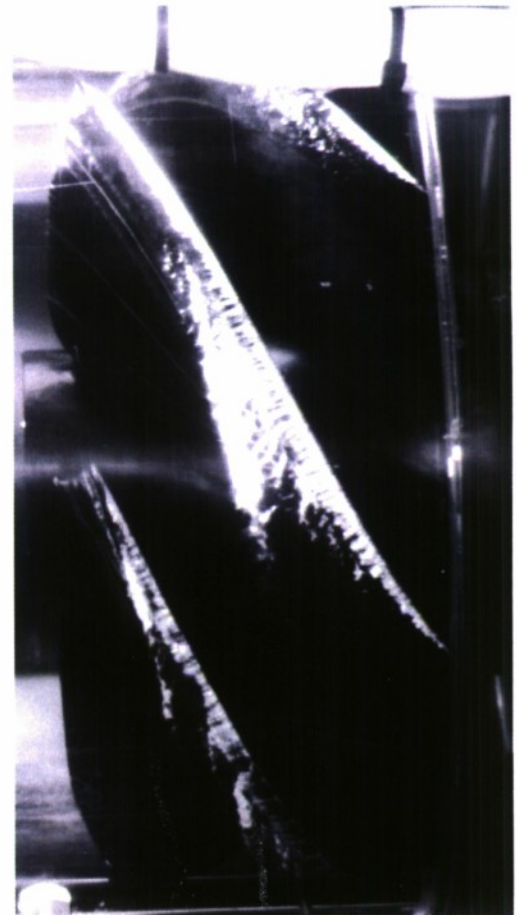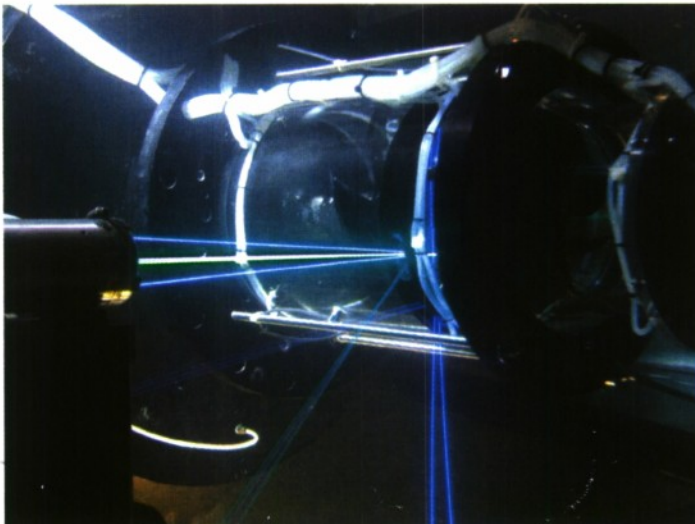
Performance Evaluation of the ONR Axial Waterjet 2 (AxWJ-2)

by

Christopher J. Chesnakas
Martin J. Donnelly
Don W. Pfitsch
Alan J. Becnel
Seth D. Schroeder

REPORT DOCUMENTATION PAGE

1. REPORT DATE (DD-MM-YYYY) December 2009	2. REPORT TYPE Technical	3. DATES COVERED (From - To) August 2007 to July 2008

4. TITLE AND SUBTITLE Performance Evaluation of the ONR Axial Waterjet 2 (AxWJ-2)	5a. CONTRACT NUMBER
	5b. GRANT NUMBER
	5c. PROGRAM ELEMENT NUMBER

6. AUTHOR(S) Christopher J. Chesnakas, Martin J. Donnelly Don W. Pfitsch, Alan J. Becnel, Seth D. Schroeder	5d. PROJECT NUMBER
	5e. TASK NUMBER
	5f. WORK UNIT NUMBER 08-1-5030-101

7. PERFORMING ORGANIZATION NAME(S) AND ADDRESS(ES) AND ADDRESS(ES) Naval Surface Warfare Center Carderock Division 9500 Macarthur Boulevard West Bethesda, MD 20817-5700	8. PERFORMING ORGANIZATION REPORT NUMBER NSWCCD-50-TR-2009/089

9. SPONSORING / MONITORING AGENCY NAME(S) AND ADDRESS(ES) Office of Naval Research 331 Ship Systems and Engineering Research Division 875 North Randolph Street Arlington, Virginia 22203	10. SPONSOR/MONITOR'S ACRONYM(S) ONR 331
	11. SPONSOR/MONITOR'S REPORT NUMBER(S)

12. DISTRIBUTION / AVAILABILITY STATEMENT
Approved for public release. Distribution Unlimited.

13. SUPPLEMENTARY NOTES

20100325260

14. ABSTRACT

Testing of a new design waterjet, the ONR Axial Flow Waterjet 2, was performed in the 36-Inch Variable Pressure Water Tunnel at the Naval Surface Warfare Center, Carderock Division. These tests measured the pump powering performance and the pump cavitation performance. The test hardware, methodology, and results are presented here, along with comparisons to computational predictions. The test results are used to make predictions of the performance of four 9-foot diameter pumps installed in a notional 970 foot long JHSS, Joint High Speed Sealift, hullform with a maximum available power of 36 MW at each pump. The results are also used to predict the performance of the same ship using smaller 7.4-foot diameter pumps. A method is also presented for making full-scale powering predictions using more detailed information from tow tank tests than is generally available.

15. SUBJECT TERMS Waterjet

16. SECURITY CLASSIFICATION OF:			17. LIMITATION OF ABSTRACT	18. NUMBER OF PAGES	19a. NAME OF RESPONSIBLE PERSON Christopher Chesnakas
a. REPORT UNCLASSIFIED	b. ABSTRACT UNCLASSIFIED	c. THIS PAGE UNCLASSIFIED	Unlimited	92	19b. TELEPHONE NUMBER (include area code) (301) 227-5833

(THIS PAGE INTENTIONALLY LEFT BLANK)

CONTENTS

FIGURES

TABLES

SYMBOLS

C_{pc6}	Pressure coefficient correction at station 6
D	Diameter of the inlet, same as D_3
D_3	Diameter of the inlet, same as D
D_6	Diameter of the nozzle exit
g	Gravitational constant
G^*_{rms}	Non-dimensional casing acceleration
H^*	Head coefficient, $H^* = \dfrac{(p_{t6} - p_{t3})}{\rho(nD)^2}$ (same as Ψ)
I	Cavitation intensity
I^*	Non-dimensional cavitation intensity

IVR	Inlet velocity ratio = V_3 / V_1
JVR	Jet velocity ratio = V_6 / V_0
K	Nozzle or bellmouth flow coefficient
n	Revolutions per second
N^*	Cavitation coefficient, $N^* = \dfrac{(p_{t3} - p_v)}{\rho(nD)^2} = \dfrac{g \cdot NPSH}{(nD)^2}$
$NPSH$	Net positive suction head, $NPSH = (p_{t3} - p_v)/\rho g$
$NPSH(A)$	Available net positive suction head
$NPSH(1\%)$	Net positive suction head at 1% loss in torque from cavitation
p	Pressure
p_t	Total pressure
p_v	Vapor pressure of water
P_w	Shaft power
P^*	Power coefficient, $P^* = \dfrac{2\pi\, n\, Q}{\rho n^3 D^5}$
PC	Propulsive coefficient = effective power / delivered power
$PSIA$	Static pressure in tunnel test section
$PSID$	Static pressure difference across bellmouth contraction
Q	Torque
Q_J	Volumetric flow rate
Q^*	Flow coefficient $Q^* = Q_J / nD^3$ (same as Φ)
r	Propeller radius at a section
R	Overall propeller radius
t	Thrust deduction, $1 - t$ = resistance / thrust
U	Velocity in stationary frame
U_x	Axial velocity
U_x	Tangential velocity
U_x	Radial velocity
V_c	Crossflow velocity, rotor coordinates
V_{rel}	Relative velocity
V_S	Ship speed
V_s	Streamwise velocity, rotor coordinates
V_s^*	Streamwise velocity, rotor coordinates, normalized by relative inflow velocity
V_n	average velocity at ITTC Station n

V_0	Water tunnel freestream speed or ship speed
w	Wake fraction, $1 - w$ = velocity in propeller plane / ship speed
x	Axial position, from leading edge of inlet
β_E	Energy non-uniformity factor
β_M	Momentum non-uniformity factor
δ	Boundary layer thickness
$\delta*$	Boundary layer displacement thickness
ζ_{13}	inlet loss coefficient from ITTC Station 1 to 3, $\zeta_{13} = \dfrac{p_{t1} - p_{t3}}{0.5 \cdot \rho V_1^2}$
η	Pump efficiency
η_H	Hull efficiency
η_J	Jet efficiency
η_P	Pump efficiency
η_R	Relative rotational efficiency
θ	Circumferential coordinate
ν	Kinematic viscosity
ρ	Mass density
ϕ	Flow pitch angle
ϕ_0	Primary flow pitch angle (function of r/R)

ABBREVIATIONS

kt.	knot, 1.6878 ft/sec (0.5144 m/s)
LCC	Large Cavitation Channel
NSWCCD	Naval Surface Warfare Center, Carderock Division
RPM	Revolutions per minute
MCR	Maximum continuous rating, 85% of full power
36VPWT	36-inch Variable Pressure Water Tunnel

(THIS PAGE INTENTIONALLY LEFT BLANK)

ABSTRACT

Testing of a new design waterjet, the ONR Axial Flow Waterjet 2, was performed in the 36-Inch Variable Pressure Water Tunnel at the Naval Surface Warfare Center, Carderock Division. These tests measured the pump powering performance and the pump cavitation performance. The test hardware, methodology, and results are presented here, along with comparisons to computational predictions. The test results are used to make predictions of the performance of four 9-foot diameter pumps installed in a notional 970 foot long JHSS, Joint High Speed Sealift, hullform with a maximum available power of 36 MW at each pump. The results are also used to predict the performance of the same ship using smaller 7.4-foot diameter pumps. A method is also presented for making full-scale powering predictions using more detailed information from tow tank tests than is generally available.

ADMINISTRATIVE INFORMATION

INTRODUCTION

In 2006, a program to develop a compact, high-power-density waterjet was initiated by the Office of Naval Research (ONR). ONR issued a Broad Agency Announcement (BAA), ONR BAA06-011[1], to request designs for these waterjets. The BAA specifies that the waterjet designs are for a notional high speed platform, designated JHSS. The JHSS or Joint High Speed Sealift is a very large, slender, high-speed ship concept for transport of a single Marine Brigade to overseas theaters. The hull is 970' long operating at a maximum transit speed of at least 36 knots. The hull form is shown in Fig 1. The hull is to be powered by four waterjets, each operating at a maximum of 36 MW. The BAA outlines specific requirements for the waterjets in terms of thrust, diameter, cavitation performance, and efficiency.
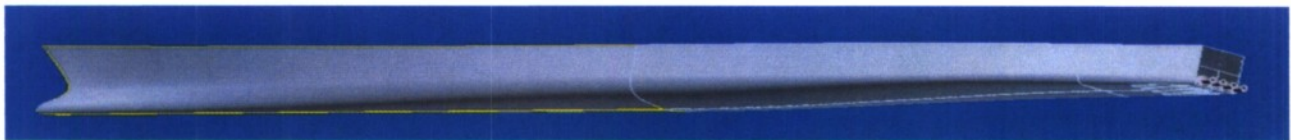
Fig. 1. JHSS hull form.

Two vendors responded to this BAA, and the pump designs submitted were tested and evaluated at NSWCCD. The designs and data were proprietary to the vendors, and so are not available for evaluation by the wider hydrodynamic community. Therefore, ONR tasked NSWCCD to design and test a new axial flow pump that would have both the geometry and the test results in the public domain. In this way, the pump could serve as a test case for pump design and analysis tools. The new pump was designed with the objectives of the BAA

as a guide, and is called the ONR Axial Flow Waterjet 2 (AxWJ-2). The design of the pump is detailed in an earlier report by Michael et al.[2].

A model scale pump was built and tested at NSWCCD. These tests included measurement of the pump powering curves, the measurement of the velocity fields through the pump, and the characterization of thrust breakdown. This report details the results of that testing.

As a part of the design process, the pump performance was calculated by NSWCCD using two different commercial Reynolds Averaged Navier Stokes (RANS) codes. The results of those calculations are also included in this report for comparison to the experimental results.

EXPERIMENTAL APPARATUS

Pump

The tested pump is an axial flow unit with an inlet diameter of 12.00 inches and is shown in Fig 2. The rotor, designated rotor 5521 by NSWCCD Code 5800, has six blades and the stator, number 5522, has eight blades. The nozzle has an exit diameter of 8.40 inches. Rotor tip gap of 0.020 inches was as small as was practical at this scale. In order to facilitate measurements of the pump performance, the pump has two features that are slightly different than is usual with waterjets. The spacing between the rotor and stator is slightly enlarged to allow measurements of the velocity field to be acquired between the blade rows. Also, the nozzle is longer than is the usual practice for a waterjet. The nozzle has a cylindrical exit section of length 3.6 inches in order to produce a uniform pressure field across the plane of the nozzle exit. Details of the pump geometry can be found in the design report of Michael et al.[2].

For testing, a 12-inch long cylindrical section is attached to the nozzle exit. This extension ensures that the pressure measurements at station 6 are in a region of low flow curvature, and thus nearly uniform pressure across the flow area. Two different nozzles (or no nozzle) can then be attached to the end of the nozzle extension to obtain coarse control over the operating point of the pump. Two nozzles were manufactured: one with an exit area 90% of the pump nozzle area, and a second with 80 % of the pump nozzle exit area. The pump with the nozzle extension and flow control nozzle is shown in Fig. 3.
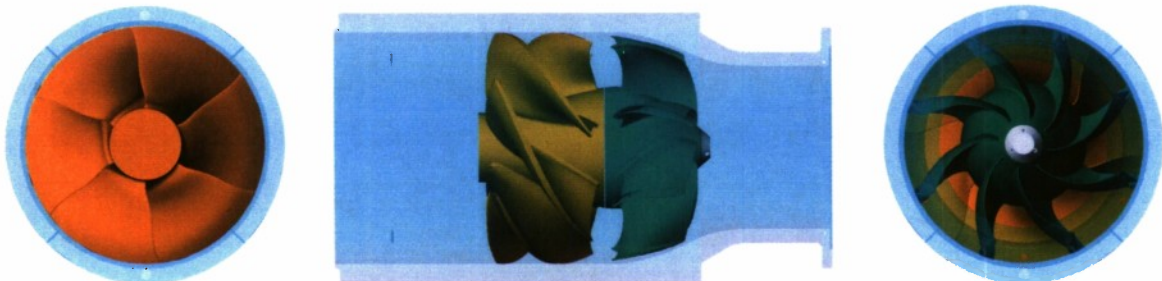
Fig. 2. ONR Axial Flow Waterjet 2.
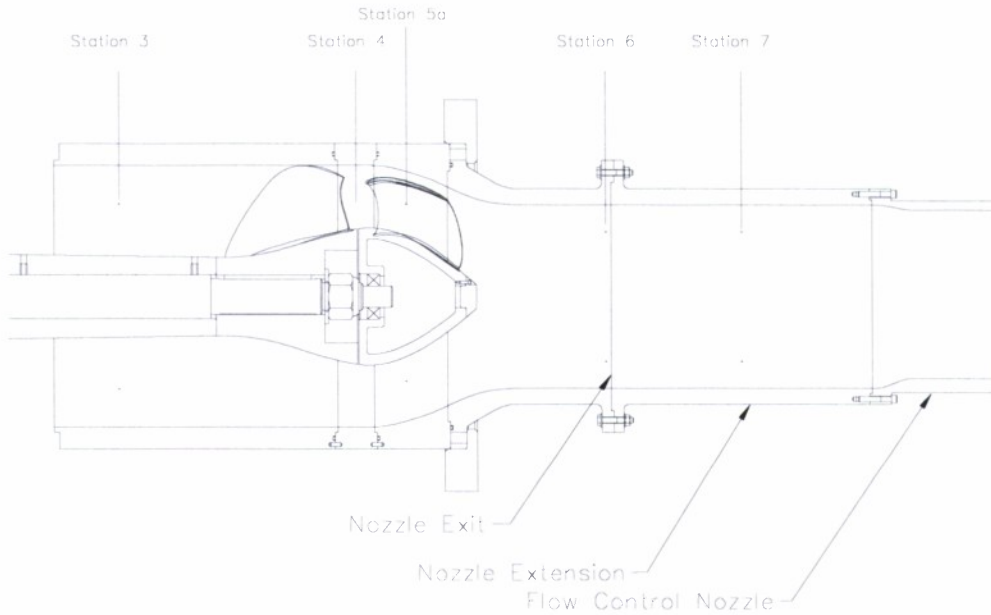
Fig. 3. ONR AxWJ2 with nozzle extension and flow control nozzle.
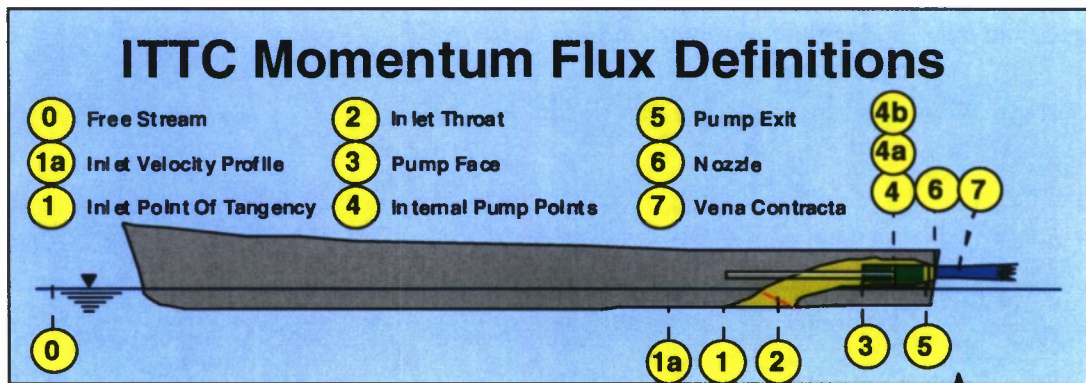
Fig. 4. ITTC waterjet reference stations.

Throughout this report, reference will be made to measurements at various stations. The station designations follow the naming conventions for waterjet stations from the 21st ITTC Quality Manual[3] as modified by the 24th ITTC Specialist Committee Report[4]. The locations of the ITTC stations is shown in Fig. 4. The locations referred to in this report are:

Station 0: Far ahead of the ship in undisturbed flow

Station 1a: One inlet width upstream of the inlet tangency point

Station 3: Just ahead of the pump blade tips, or at the pump inlet flange

Station 5: Just aft of the pump stator or at the pump discharge flange

Station 6: At the nozzle outlet plane

The specific location of the stations referred to in this test are shown in Fig. 3. The numbering of the tap locations generally follows the ITTC notation, with the exception of station 5a — which is in the stator blade passage instead of after the stator — and station 7 — which is in the nozzle extension and not aft of the waterjet

nozzle. It should also be noted that the location of the velocity measurements at station 6 is displaced from the location of the pressure measurements. Due to the need for optical access, the station 6 velocity measurements are 0.6" downstream of the nozzle exit.

Facilities

36-Inch Water Tunnel

The NSWCCD 36-inch Variable Pressure Water Tunnel (36VPWT) is a recirculating design with interchangeable test sections. A 36-inch diameter, open-jet test section was used for these tests. The tunnel allows the pressure in the test section to be varied so that cavitation behavior can be investigated. Both upstream and downstream drives are available for propeller testing. For these tests, the rotor was driven from upstream. Inflow to the pump was uniform except for the wall and shaft boundary layers.

In order to use the facility as a pump loop, a fiberglass bellmouth is installed at the exit of the 36-inch tunnel nozzle as shown in Figs. 5 and 6. This bellmouth directs the entire flow of the tunnel through the pump. In this way, flow rate through the pump is controlled by changing the pump speed, by changing the tunnel impeller speed, and by changing the flow control nozzle.
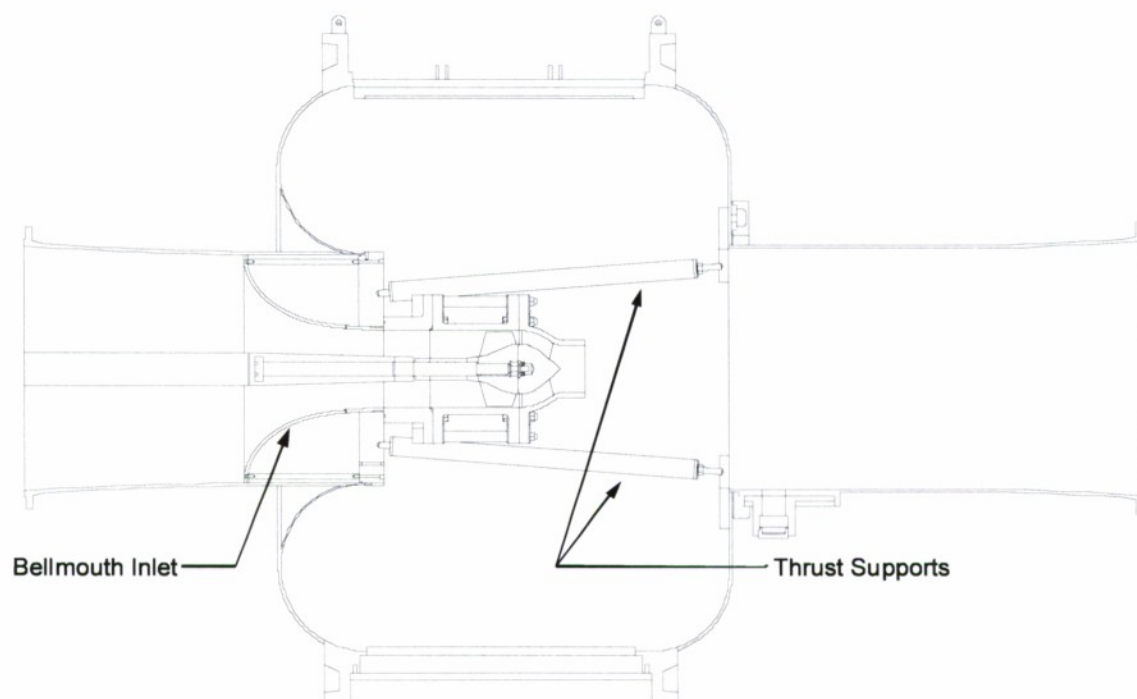
Fig. 5.   Modifications to 36-inch Variable Pressure Water Tunnel to create a pump loop.
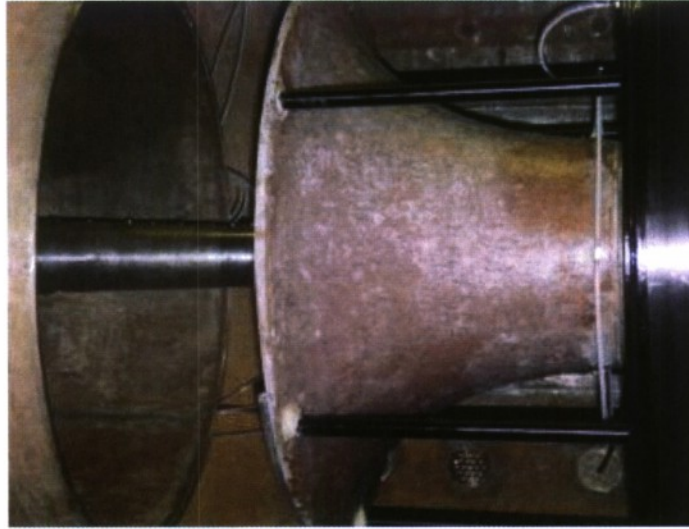
Fig. 6. Bellmouth insert in the 36-Inch VPWT.

Instrumentation

Pressure Measurements

Pressure taps are placed throughout the pump to measure the pump performance. The locations of these taps are shown in Fig. 3. Four taps are placed in the cylindrical section of the inlet ahead of the rotor, station 3; four taps are placed in the contracting section of the nozzle between the stator blades, station 5a; four taps are placed in the cylindrical section of the nozzle just forward of the exit, station 6; and four taps are placed in the middle of the nozzle extension, station 7. The taps at station 5a were placed in the stator passage instead of the normal practice of just behind the stator in order to have a greater pressure differential to station 6 which could be calibrated to the flow rate. Each tap is connected to a separate Validyne differential pressure transducer which is referenced to tunnel static pressure. By referencing each pressure measurement to tunnel static pressure instead of atmospheric pressure the range of the transducer can be appropriately sized to the expected range of the measured pressure thereby increasing the resolution of the measurement. This configuration is required for testing which requires the water tunnel static pressure to be changed. Pressure ranges of these transducers are 20 psi at station 3, 32 psi at station 5, and 10 psi at stations 6 and 7. Calibration uncertainty for these gages was 0.3% of full scale.

Torque, and RPM

Waterjet impeller torque measurements are acquired with a shaft dynamometer designated Dyno#3. The dynamometer is a strain gage base device connected to Vishay Model 2310 strain gage amplifiers through a slip-ring assembly. The maximum range of this dynamometer is 7200 lbs of thrust, and 1800 ft-lbs of torque. For this series of measurements the dynamometer was calibrated to a range of 5000 lbs of thrust, 760 ft-lbs of

torque, with a calibration uncertainty defined as two times the standard deviation of the residuals of 3.4 lbs, and 1.2 ft-lbs, or 0.07 % of full-range for both components.

RPM is determined using a magnetic pickup directed at a 60 tooth gear on the tunnel drive shaft. The output signal is converted to a voltage proportional to rpm by an Analog Devices 631 frequency to voltage convertor. The uncertainty of the rpm calibration is ± 1 rpm.

Cavitation Viewing

An upstream-mounted video camera was used to view cavitation on the suction side of the rotor blades. The camera was mounted to the top of the shaft just upstream of the bellmouth. The camera is shown mounted on the shaft without the pump in place in Fig. 7. A second camera viewed cavitation from outside the test section through one of the side windows. The second camera viewed the tip region of the rotor through the clear acrylic rotor housing.

Pump Casing Accelerometers

Three accelerometers were mounted to the pump casing, just forward of the impeller at the locations shown in Fig. 8. These accelerometers were used for quantifying cavitation intensity throughout the thrust breakdown testing. Accelerometers 1, 2, and 3 in Fig. 1 had sensitivities of 10, 10, and 100 mV/g respectively. Thirty-two, five second samples were acquired at 2000 Hz at each test condition for averaging purposes.

Fig. 7. Shaft camera mounted upstream of bellmouth in 36VPWT for cavitation viewing.
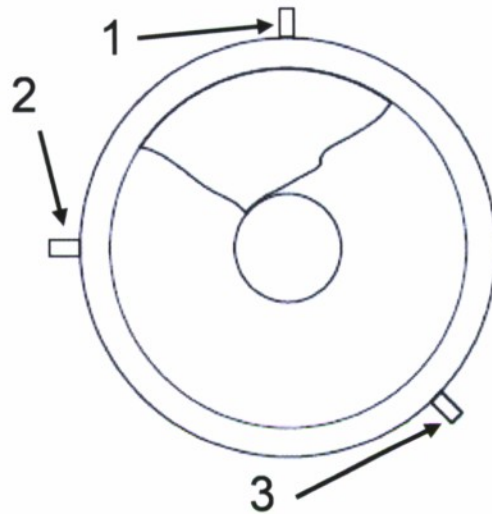
Fig. 8.   Pump casing accelerometer locations shown looking aft.

Laser Doppler Velocimetry (LDV)

Inflow, Station 3

An LDV system was used to measure the radial variation of velocity at a plane upstream of the waterjet inlet but after the bellmouth contraction. The axial velocity measurements were integrated to obtain the waterjet flow rate. To check for circumferential velocity variation, the LDV radial survey could be done at 3 equally spaced angular positions. For this test, however, only the bottom port radial line was measured, as previous PIV measurements indicated that this was sufficient. The waterjet setup includes a 7-3/4 inch long anodized aluminum entrance section. This section concludes the bellmouth contraction and transitions to a cylindrical 12 inch diameter cross-section. The LDV velocity measurements were located 2.38 inches upstream of the aluminum section flange, where the flow contraction was complete.

Three 0.85 inch holes were drilled through the entrance section near the downstream end. Bronze plugs were manufactured to fill the holes. The plug ends were contoured to exactly match the inner wall of the entrance section and cause no disturbance to the flow. An O-ring seal insured there was no flow into or out of the plugged holes.

A 1 inch (25 mm) diameter, fiber optic, LDV probe (TSI model 9812) was assembled into a linear traverse mechanism that could be mounted to any of the entrance section holes. The measurement volume was displaced from the probe end by 5.7 inches. The ellipsoidal measurement volume was 0.050" long (probe axis direction) and 0.004" across. A flat glass optical flat window 0.4" in diameter was glued into the end of the mechanism that filled the entrance section hole. The flat window was minimally recessed so that nothing extended into the section diameter. An O-ring seal insured there was no flow into or out of the velocity measurement hole. Fig. 9

shows the relationship of the LDV mechanism to the waterjet bellmouth and entrance section in a cutaway rendering.
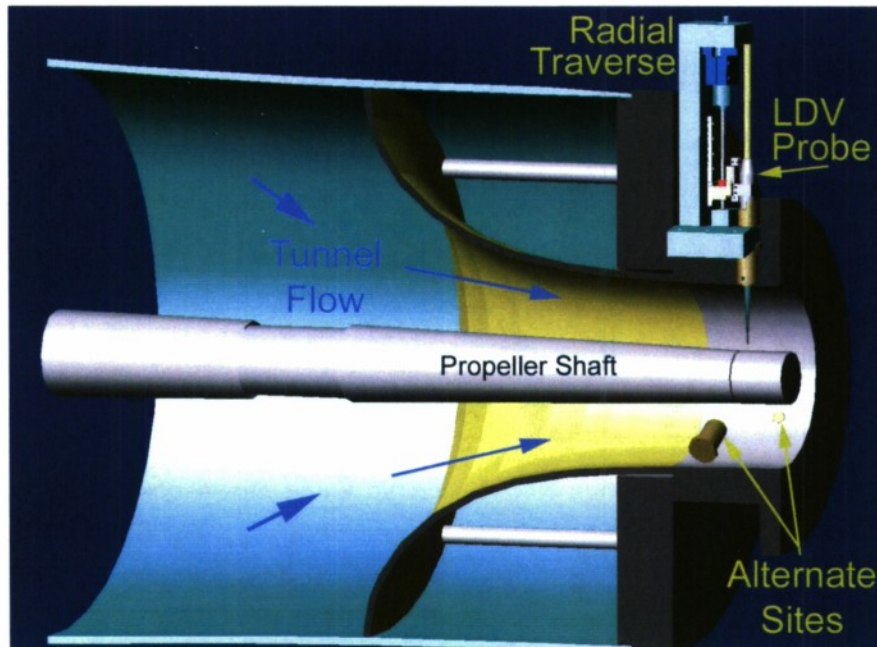
Fig. 9.   Inflow LDV measurement system for station 3.
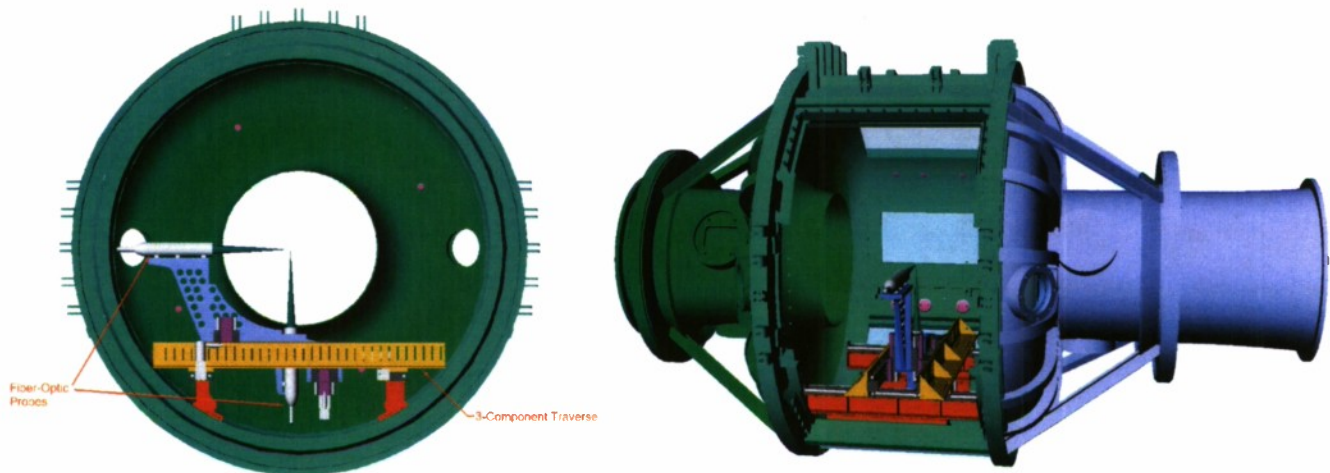
Fig. 10.   3-D LDV measurement system for stations 4 and 6.

Mid Stage and Nozzle Exit, Stations 4 and 6

A different LDV system was used to make 3-component velocity measurements between the rotor and stator, station 4, and just aft of the nozzle exit, station 6. The LDV system consisted of two TSI model 9832 fiber optic probes rigidly mounted together on a traverse which could translate in the three spatial directions. The probes and the traverse were located in the recirculating region of the test section, outside of the jet, as shown in Fig. 10. The focal distance of the probes (18.5" in water) was sufficient to place the probe bodies outside of the jet. The horizontal probe utilized the green (514.5 nm) and blue (488 nm) beams of an argon-ion

laser to measure the vertical and axial components of velocity, respectively. The vertical probe utilized the violet (476 nm) beam of the argon-ion laser to measure cross-stream horizontal component of velocity. Both probe volumes were 0.003" by 0.050".

The position of the shaft was encoded with an 8192-counts/revolution signal, which was recorded with each velocity measurement. Doppler signals were analyzed with a TSI Model IFA 655 Digital Burst Correlator. The processor performs a 256-sample, double-clipped, autocorrelation on each Doppler burst, allowing the measurement of velocity even when the signal-to-noise ratio is low. The processors were operated in the random mode.

The flow was seeded with 1500 grit silicon-carbide powder with particles 1 to 2 μm in diameter. Since the water in the tunnel recirculates, seed particles needed to be added infrequently.

In order to obtain measurements at station 4, a window was placed in the pump casing between the rotor and the stator as shown in Fig. 11. The window was made from 0.050" clear polycarbonate sheet, curved to match the inner contour of the pump casing. The thin windows ensured that the laser beams would pass through the curved windows with minimal optical distortion.
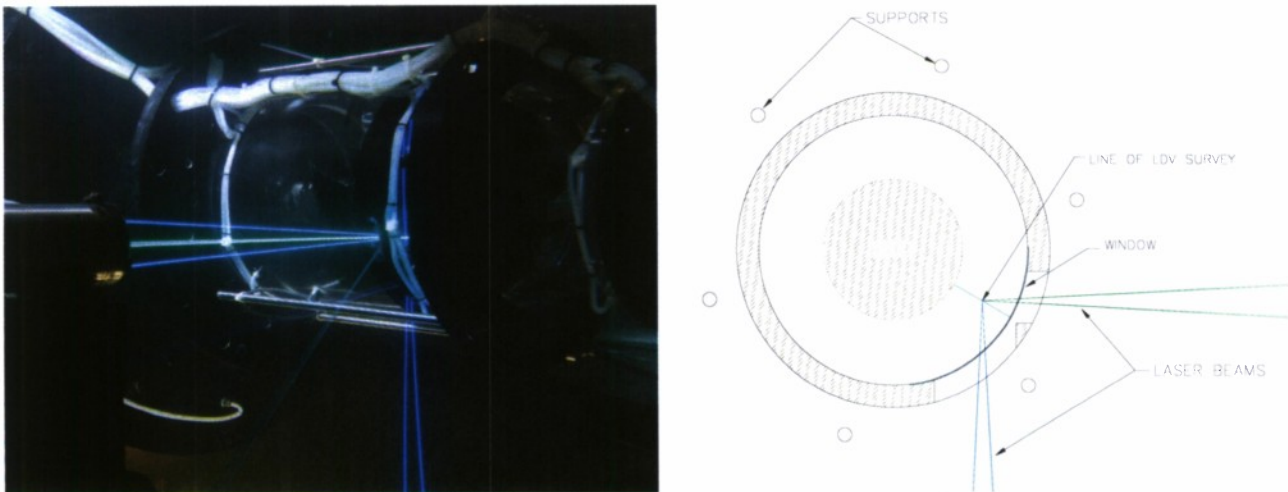
Fig. 11. LDV window in pump casing at station 4.

Bellmouth Pressure

Flowrate through the waterjet is also quantified by a differential pressure measurement, *PSID*, between a ring of taps on the water tunnel, upstream of the bellmouth and a ring of taps on the bellmouth contraction. A 10 psi Viatran differential transducer, with an uncertainty of 0.014 psi, or 0.14% of full-scale, is utilized for this measurement.

COMPUTATIONAL TOOLS

Fluent

Reynolds-Averaged Navier Stokes (RANS) computations were used for analysis during the design on the pump as documented in Michael et al.[2]. The grids were generated using Ansys IcemCFD[5] and the solution was computed using Ansys Fluent[6]. Both software packages are commercially available and have been validated for waterjet applications in Brewton et al.[7].

The simulation modeled a single rotor blade and a single stator blade, as shown in Fig. 12, taking advantage of the pump's periodicity. The rotor and stator were manually meshed in separate domains using Icem's Hexa utility. Each domain's mesh was approximately 375,000 hexahedral cells. The wall spacing was set such that the wall y^+ values were between 50-60 on the surfaces of the hub, shroud, rotor blade, and stator blade. Wall y^+ is the non-dimensional distance of the first cell from a wall boundary and is defined as:

$$y^+ = \frac{\rho u_\tau y}{\mu}$$
(1)

where u_τ = friction velocity, and y = distance to the wall. The mesh was constrained such that there was one-to-one node matching across the periodic boundaries. The mesh was non-conformal at the interface plane between the rotor and stator domains. The tip gap was modeled to be identical to the experimental model, with approximately 21 mesh points through the gap.
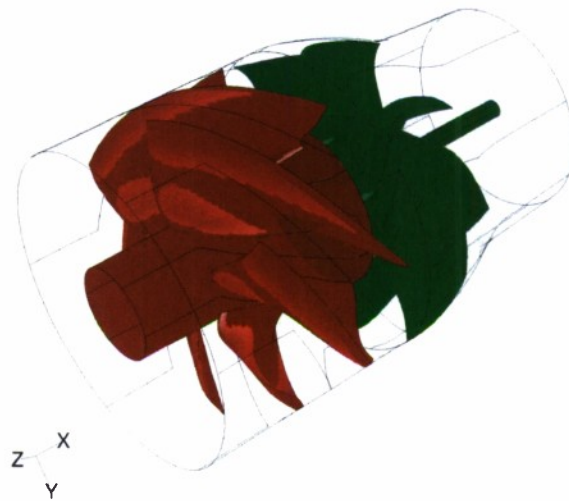
Fig. 12. Computational domain of Fluent calculation of pump.

The solutions were computed using Fluent's steady state pressure based solver. The solution included a velocity inlet, a pressure outlet, and periodic boundary conditions. A mixing plane model was used as an interface between the rotor and stator domains. This model circumferentially averaged the values as they passed from the rotor domain to the stator domain. The k-ε turbulence model was used with enhanced wall functions. Fluent[6] has shown this viscous model to be very well suited for the previously listed values of wall y^+.

Convergence was monitored through global values such as thrust and torque as well as local values such as the pressure on the blade surfaces.

CFX

CFX 12.0 is a commercially available Reynolds-Averaged Navier-Stokes fluid dynamics flow solver from ANSYS Inc. that is used to analyze the viscous performance of turbomachinery. CFX is broken into modules to perform the required tasks for the performance estimate. The geometry consisting of the hub, shroud and blade profiles were provided in the form of ASCII files. These ASCII files were read into ANSYS-Turbogrid to generate the rotor and stator structured grids. The grid size and spacing were adjusted to get a y^+ spacing from all surfaces of less than 2 for use with the Shear Stress Transport (SST) turbulence model. This grid topology was saved in a script file for use during each grid update so that each grid has essentially the same size and spacing.

ANSYS-CFX Pre was used to setup the physics of the calculation. The working fluid, RPM, steady-state or transient, non-cavitating or cavitating, mass flow and other boundary conditions, etc are setup in this module. Two types of calculations were performed, rotor only, and rotor and stator using a mixing plane between different frames of reference. The performance calculations were carried out at both model and full scale whereas the cavitation prediction was only performed at model scale.

ANSYS-CFX Solver was used to solve the RANS equations for this waterjet pump. The solver execution time was typically 15-20 minutes for a rotor only non-cavitating calculation, 2 hours for the rotor only cavitating calculation, and about 3-4 hours for a rotor-stator calculation using a single processor Dell M90 portable workstation with 2.33 GHz processor and 2 GB of RAM.

ANSYS-CFX Post was used to post process the results which included torque, headrise, cavitation coverage, pressure distributions on both the blade surfaces and hub and shroud surfaces and rotor and overall pump efficiency.

Calculations were performed on the model-scale pump with the 8.40 inch nozzle. Calculations were performed on the pump only; no modeling of the inlet or water tunnel was performed during this effort.

Two types of CFX calculations were performed for the waterjet, cavitating rotor only and non-cavitating rotor-stator. The rotor/stator calculations were used to calculate the pump's powering performance, and the rotor only calculations were used to calculate thrust breakdown. All model calculations used fresh water with a density of 62.26 pounds per cubic foot as the working fluid and a rotor speed of 1400 RPM for the performance predictions and 2000 RPM for the cavitation prediction. The full-scale predictions used saltwater as the working fluid with a density of 64.04 pounds per cubic foot at 525 RPM. The model-scale calculations were performed on a 12.00 inch diameter waterjet, shown in Fig. 13, consisting of 6 rotor and 8 stator blades. For the calculations only 1 blade passage was modeled for both rotor and stator. The rotor tip gap was modeled for both

calculations. A structured grid consisting of 193K nodes and 179K elements was used for the rotor calculations and a grid of 205K nodes and 192K elements was used for the stator calculations. A total pressure boundary condition was set on the inflow surface, a mass flow boundary condition was set on the outflow surface, a periodic boundary condition was set on the blade interface surfaces, and a viscous wall was set on all solid surfaces.

The cavitating performance of the rotor was predicted using the Rayleigh Plesset cavitation model in ANSYS CFX using the default values. The net positive suction head (NPSH) was set to a high value for the first calculation, yielding the same performance as the non-cavitating case. The NPSH was then lowered in successive steps while keeping the rotor speed constant, with the steps in NPSH selected to approximately match those of the 36-inch VPWT test. The torque or headrise breakdown value as was then determined as in the 36-inch Water Tunnel.
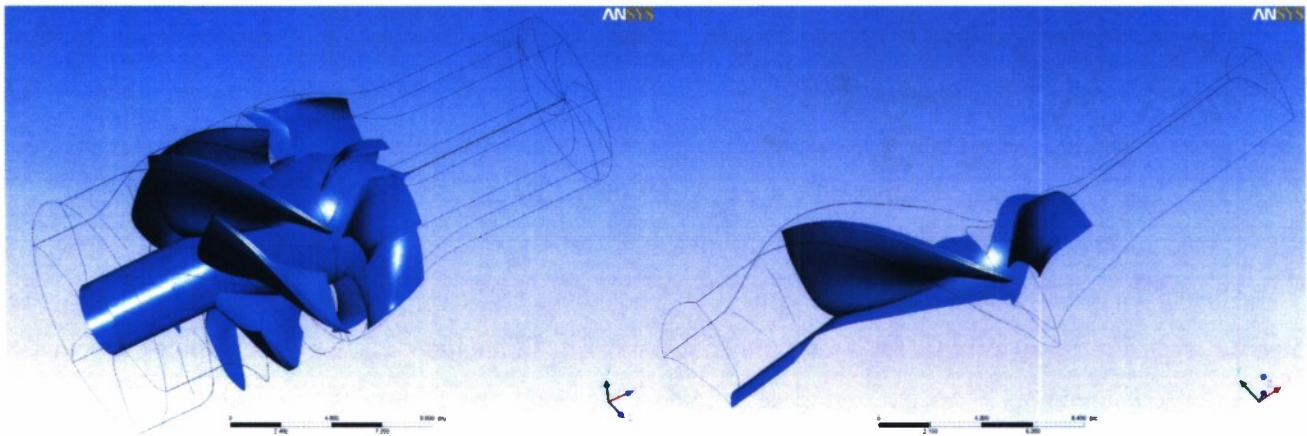
Fig. 13. Computational domain of CFX calculation of pump.

PROCEDURE

Test Conditions

Tests to measure head rise and efficiency were performed at 1400 rpm, and with total inlet pressure at 35 – 50 psia. Flow rate was adjusted in these tests by varying the tunnel impeller speed and by changing the flow control nozzle. Tests of thrust breakdown were performed at 2000 rpm. Tunnel static pressure was started at a high-pressure, non-cavitating condition and then lowered during the run.

Data Acquisition

Pressure Thrust and Torque

All pressure, thrust, and torque measurements are taken with a National Instruments PXI based data collection system. The data collection and analysis codes are written in LabVIEW v8.2 and do real-time

calculations of waterjet performance parameters for data validation. The PXI system utilizes a NI PXI-6031E data acquisition card for analog measurements. The PXI-6031E is a 64 channel, 16 bit analog to data convertor with a maximum sampling rate of 100 kHz. In order to reduce system noise the A/D board is used in a differential mode limiting the number of inputs to 32. Physical connections to the data acquisition card are made through BNC blocks (NI part numbers BNC 2110 and BNC 2115). All pressure, thrust, and torque data are acquired at a sampling rate of 100 Hz, for 10 seconds, or 1000 samples. Anti-aliasing low-pass filters are set to 10 Hz and are utilized on all analog data channels. From each ten second sample a mean and standard deviation are computed in volts, and converted to engineering units based on pre-test calibrations. Time history data is also recorded for later analysis.

Station 3 LDV

Data collection and probe positioning was performed using the FIND software package from TSI Inc. A 27 radius position matrix was measured with increased spatial resolution near the wall and shaft. Velocities were collected for 12 seconds at each radius. Away from the walls, velocity was sampled $10,000 - 20,000$ times. Near the walls, particle scattered light signals were partially masked by light scattered off the glass or shaft surfaces. Slower data rates reduced the measurement count to as low as 350. Surveys were conducted with the various flow control nozzle configurations at a variety of impeller speeds. A total of 29 flow conditions were measured from $0.714 \leq Q^* \leq 0.94$.

Station 4 LDV

Measurements were acquired at station 4 at 55 radial points on a line 30 degrees below the horizontal as shown in Fig. 11. All data was acquired in random mode. Individual velocity realizations were tagged with the angular position of the shaft at the time of acquisition, and were sorted into 1024 angular positions. At each radial position, 1 million total velocity realizations were acquired for the three velocity components, resulting in about $100 - 500$ velocity realizations in each angular bin on each channel. Three operating conditions were measured: $Q^* = 0.712, 0.772,$ and 0.850.

Station 6 LDV

Measurements at station 6 were acquired 0.6 inches behind the nozzle exit. These measurements were performed without the nozzle extension in place, since the nozzle extension blocked optical access to station 6. Velocities were measured on a the 629 point grid shown in Fig. 14. Due to the limited (approximately 5.5 inches) vertical range of the traversing system, the entire jet could not be measured. At each point in space, data were collected for six seconds, resulting in from $10,000 - 20,000$ velocity realizations on each channel at each point. Velocity measurements at station 6 were acquired at $Q^* = 0.850$ and 0.938.
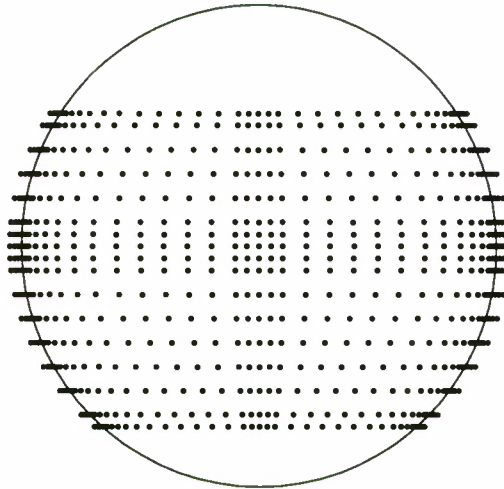
Fig. 14. Station 6 LDV measurement grid.
Circle represents the jet exit.

Thrust Breakdown

Tests of thrust breakdown were performed at 2000 rpm. Tunnel static pressure was started at a high-pressure, non-cavitating condition and then lowered during the run. Tunnel impeller speed was zero to prevent cavitation on the impeller. Pump RPM was kept constant during a thrust breakdown run, but no attempt was made to maintain constant flow rate through the pump.

Cavitation Viewing

To document and view cavitation conditions during thrust breakdown runs, two cameras were set up to image the AxWJ-2. A submersible camera imaging at 30 fps with a resolution of 640 x 480 pixels was mounted to the shaft looking aft at the suction side of the impeller. Another camera was mounted outside of the tunnel looking at the side of the impeller for viewing gap tip leakage cavitation, this camera's frame rate was synchronized with the strobe lights used to illuminate the Waterjet and had a resolution of 2000 x 2000 pixels. Synchronizing the strobe lights to the impeller shaft rate "froze" the impeller position in the camera images.

Data Reduction

Flow Rate

Flow rate through the pump in the 36-inch Variable Pressure Water Tunnel was measured using the bellmouth inlet as a flow meter. The pressure differential was measured between the water tunnel ring 2, just upstream of the bellmouth, and wall-pressure taps located at the end of the bellmouth contraction. The pressure differential was correlated with measurements of the volumetric flow using the LDV inlet line surveys. Earlier measurements with stereo PIV found the bellmouth exit flow to by highly symmetrical, indicating that a line survey was sufficient. The flow rate was then found from the following relation:

$$Q_J = 13.012 \cdot \sqrt{\frac{PSID}{\rho}} \tag{2}$$

where Q_J is in ft^3/s, $PSID$ is the pressure across the bellmouth in psi, and ρ is the water density in slugs/ft^3.

Pump Performance Curves

At each station, the mass-averaged total pressure was calculated from:

$$\overline{p_t} = p + \beta_E \cdot \frac{1}{2} \rho \left(\frac{Q_J}{A} \right)^2 \tag{3}$$

where p is the measured pressure at the station, A is the flow area, and β_E is the energy non-uniformity factor. β_E is a term that relates the mass-averaged dynamic pressure to the dynamic pressure calculated from the average velocity. It is defined as

$$\beta_E = \frac{1}{A} \int \frac{U_x U^2}{\overline{U_x}^3} dA \tag{4}$$

Values for β_E were found from integrating the LDV measured flowfields.

Total pressure rise through the pump was then $p_{t6} - p_{t3}$, where the overbar notation has been dropped, and it is understood that these are the mass-averaged total pressures. The non-dimensional head-rise coefficient was then

$$H^* = \frac{p_{t6} - p_{t3}}{\rho(nD)^2} \tag{5}$$

and the pump efficiency was

$$\eta = \frac{(p_{t6} - p_{t3})Q_J}{2\pi n Q} \tag{6}$$

Other quantities characterizing the pump performance are the non-dimensional flow rate

$$Q^* = \frac{Q_J}{nD^3} \tag{7}$$

and the non-dimensional power

$$P^* = \frac{2\pi n Q}{\rho n^3 D^5} = 2\pi K_Q \tag{8}$$

When non-dimensionalized in this way, the pump efficiency can also be expressed as

$$\eta = \frac{Q^* H^*}{P^*} \tag{9}$$

Flow Integrations

The velocity measurements using LDV at station 3 did not cover the entire flow area. The system could not measure the flow to the wall, but rather to only 0.1" from the shaft and 0.03" from the pump casing window. In order to integrate over the whole flow area, the velocities near the wall needed to be added. This was accomplished by adding to the data a point at the wall with an axial velocity with a value of 77% of the axial velocity of the closest measured point. Using this slip velocity at the wall ensures that the integrated values of velocity and the velocity products are very close to what would be calculated from a turbulent boundary layer with a 1/7th power law velocity distribution. To obtain the average quantities for the flow at station 3, radial symmetry was assumed.

To integrate the velocity field from the station 6 measurements, it was first necessary to fill in the missing data at the top and the bottom of the jet. To do this, the data was first interpolated onto a circular grid of diameter $1.02 \cdot D_6$, with 103 points in the radial direction and 129 in the circumferential direction. Data for points which were outside of the measurement zone were copied from points at some multiple of 45 degrees away (the stator blade passage width) for which there were data. The growth of the shear layer between the end of the nozzle and the measurement plane, a distance of 0.6 inches, is small but significant. To obtain the correct mass flow, the integration needs to extend to about $1.02 \cdot D_6$. To obtain the non-uniformity coefficients, the data is integrated only to the nozzle diameter. This is done since the velocity profile at the edge of the jet looks similar to a turbulent boundary layer profile up to the nozzle diameter. Integrating beyond that diameter results in undue influence from the shear layer growth.

Station 4 and 6 Velocities

The velocity measurements at stations 4 and 6 are generally normalized by nD, where n is the rotor rotation rate, and D is the inlet diameter. The exceptions to this are velocities with a superscript asterisk, which are normalized by the *relative* inflow velocity

$$V_\infty = \sqrt{\overline{U}_x^2 + (2\pi r n)^2} \tag{10}$$

Velocities at station 6 and circumferentially averaged velocities at station 4 are presented in the stationary coordinate system, while the velocity fields at station 4 are presented in the rotating coordinate system of the blades.

In order to better illustrate the features of the flow, the velocities in the rotating frame measurement planes are rotated into the primary-secondary coordinate system shown in Fig. 15. In this coordinate system, a primary, or streamwise, direction s is defined as being in the axial-tangential plane, at the circumferentially averaged pitch angle, ϕ_0. Since the flow pitch angle is different at each radius, the coordinate system is different at each radius as well. The secondary velocities are then the orthogonal velocity component in the x-t plane, V_c, and the radial velocity, V_r. These velocity components can be calculated from:

$$V_s = \quad \sin\phi_0 \cdot V_x + \cos\phi_0 \cdot V_t$$
$$V_c = -\cos\phi_0 \cdot V_x + \sin\phi_0 \cdot V_t \tag{11}$$
$$V_r = V_r$$

The flow vector in the stationary frame, U, and the flow vector in the rotating frame, V, are related by

$$V_x = U_x, \qquad V_t = U_t - 2\pi rn, \qquad V_r = U_r \tag{12}$$
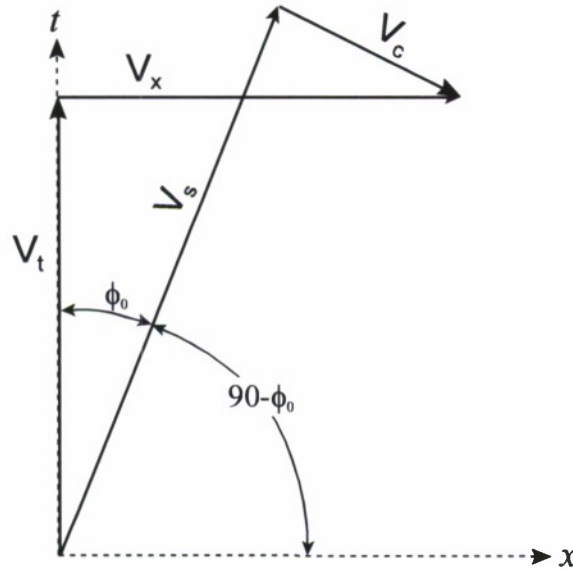
Fig. 15. Primary-secondary flow coordinate system for LDV measurements.
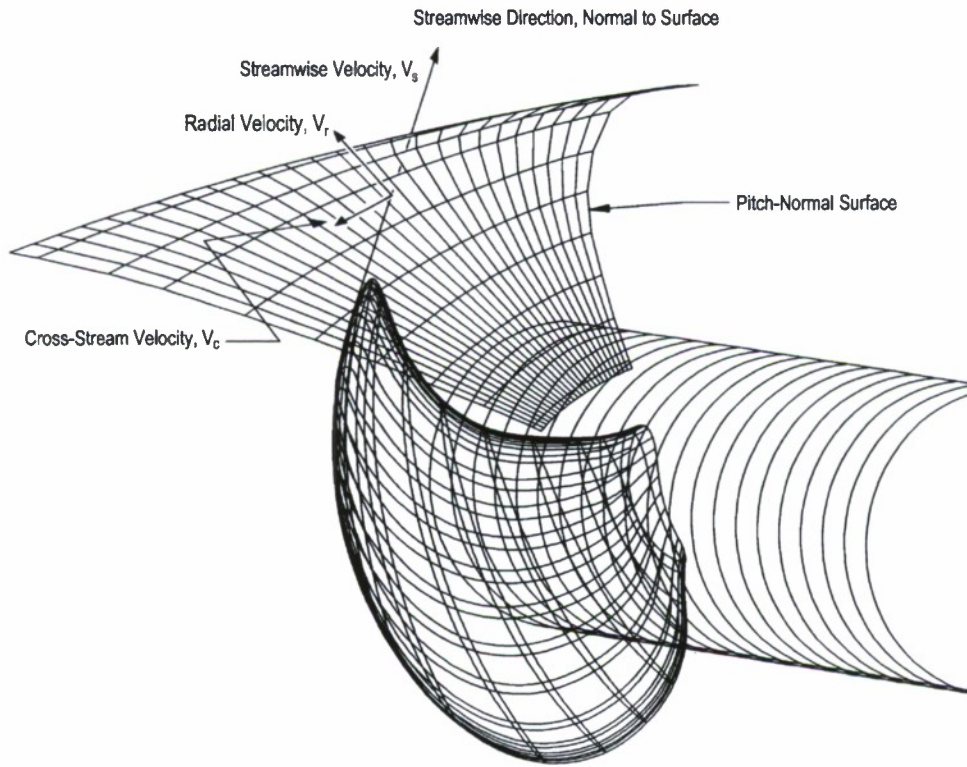
Fig. 16. Pitch-line perpendicular plane for secondary flow presentation.

In order to examine vectors of the secondary flow — particularly in the tip-vortex region — it is useful to project the vectors onto a plane perpendicular to the streamwise direction **s**, as shown in Fig. 16. To do this, the angular coordinate for each plotted point is found from:

$$\theta_p = (\theta_r - \theta_c)\sin\phi_0 \qquad (13)$$

where θ_r is the actual circumferential coordinate relative to the rotor, θ_p is the plotted circumferential coordinate, θ_c is the circumferential coordinate of the center of the plot, and ϕ_0 is the average flow pitch angle in the rotating frame (note that ϕ_0 is a function of r). This makes the cross section of the vortex circular and makes the secondary-flow vectors point in the correct direction. Plots shown in this pitch-normal projection will be labeled as "Projected".

Thrust Breakdown

Thrust breakdown values were calculated by operating the pump at a constant rpm and tunnel velocity, and decreasing the pressure until breakdown occurred. Tunnel impeller speed was zero to prevent cavitation on the impeller. Pump RPM was kept constant during a thrust breakdown run, but no attempt was made to maintain constant flow rate through the pump. Thrust breakdown was measured at three flow rates: with the nozzle extension and no flow control nozzle, with the 90% area flow control nozzle, and with the 80% area flow control nozzle.

The torque, headrise, and thrust all drop off at low pressure due to the effects of cavitation. The drop in torque and thrust are measured directly, while headrise is a calculated quantity. Loss of pump performance, or thrust breakdown, can be defined in several ways: a 1% drop in torque, a 3% drop in headrise, or a 1% drop in efficiency. Headrise and efficiency are derived quantities, while torque is a directly measured quantity and is therefore more reliable. The point of thrust breakdown was therefore defined as when the rotor torque dropped 1% from the value of the torque at high pressure. In the *Results* section, all three approaches are compared.

Blade Cavitation Area

The percentage of the blade covered by cavitation was found by analyzing shaft camera photos. The projected cavitation region was outlined in the image and the projected 2D area was measured as a percentage of total blade 2D projected area. When the cavitation region extended behind an adjacent blade (out of the view of the camera), an extended cavitation region was assumed using knowledge of the cavitation behavior from personal observation.

UNCERTAINTY ANALYSIS

LDV Velocities

The probe velocity components were calibrated in air using a spinning wheel surface. A carefully measured wheel speed and LDV measurement radius yielded a calibration bias uncertainty of 0.3%. The uncertainty in each measured velocity component at stations 3 and 6 is 0.5% of the total velocity. Velocity uncertainty in the measured components at station 4 is higher due to the smaller sample size at each point in the flow and the higher turbulence levels. Uncertainty in each velocity component at station 4 is 0.6% in the freestream and 2.3% in the high turbulence regions of the blade wakes and near the wall.

Pump curves

In order to estimate the uncertainty on the measured pump performance, it was first necessary to estimate the uncertainty in the measured quantities which were used to calculate the pump performance. These fundamental uncertainties are quantified in Table 1. In this table, uncertainties listed as a percentage are a fraction of the measured value, otherwise the uncertainties are absolute.

Table 1. Elemental uncertainties for measured quantities.

Item	Uncertainty
n	0.016%
Q	0.3%
K	0.7%
p_3	0.06 psi + 0.003·C_{p3}
p_5	0.096 psi
p_6	0.03 psi
p_v	0.013 psi
$PSID$	0.06 psi
$PSIA$	0.102 psi
β_{E3}	0.004
β_{E6}	0.006
C_{pc6}	0.004
ρ	0.0002 slugs/ft^3

Unless otherwise noted, uncertainties are non-dimensional.

The uncertainty in Q listed in Table 1 is higher than the gauge uncertainty listed in the *Instrumentation* section. The uncertainty listed here also includes the variability seen in the measurements from run to run.

The uncertainty in p_3 listed in Table 1 has two parts. The first part, listed as a fraction of a psi, is the gauge uncertainty. The second part, listed as a fraction of C_{p3}, is the uncertainty that the wall tap measurement represents the average pressure over the area of station 3. Similarly, the uncertainty in the pressure at station 6 has two parts. Here, though, the uncertainty that the wall tap measurement represents the average pressure over

station 6 is treated separately as C_{pc6} in order to better understand the influence of pressure non-uniformity at the nozzle exit.

The uncertainty for the calculated quantities is then found using standard uncertainty analysis methods. The uncertainty for Q_J is the same as the 0.7% uncertainty in the bellmouth coefficient K. The uncertainty in the non-dimensional flow coefficient, Q^*, is

$$\left(\frac{U_{Q^*}}{Q^*}\right)^2 = \left(\frac{U_{Q_J}}{Q_J}\right)^2 + \left(\frac{U_n}{n}\right)^2 \tag{14}$$

When Equation 5 is expanded, the non-dimensional head rise coefficient, H^*, found from

$$H^* = \frac{1}{\rho n D^2} \cdot \left[p_6 - p_3 + \frac{1}{2}\rho Q_J^2 \left(\frac{\beta_{E6} + C_{pc6}}{A_6^2} - \frac{\beta_{E3}}{A_3^2} \right) \right] \tag{15}$$

and the uncertainty in H^* is

$$\left(\frac{U_{H^*}}{H^*}\right)^2 = \left(\frac{U_n}{n}\right)^2 + \left(\frac{U_{p_3}}{\Delta p_t}\right)^2 + \left(\frac{U_{p_6}}{\Delta p_t}\right)^2 + \left[\frac{\rho Q_J^2}{\Delta p_t} \cdot \left(\frac{\beta_{E6} + C_{pc6}}{A_6^2} - \frac{\beta_{E3}}{A_3^2} \right) \cdot \frac{U_{Q_J}}{Q_J} \right]^2$$
$$+ \left(\frac{1}{2} \frac{\rho Q_J^2}{\Delta p_t A_3^2} \cdot U_{\beta_{E3}} \right)^2 + \left(\frac{1}{2} \frac{\rho Q_J^2}{\Delta p_t A_6^2} \cdot U_{\beta_{E6}} \right)^2 + \left(\frac{1}{2} \frac{\rho Q_J^2}{\Delta p_t A_6^2} \cdot U_{C_{pc6}} \right)^2 \tag{16}$$

where Δp_t is $p_{t6} - p_{t3}$. The uncertainty in the pump efficiency is

$$\left(\frac{U_\eta}{\eta}\right)^2 = \left(\frac{U_n}{n}\right)^2 + \left(\frac{U_Q}{Q}\right)^2 + \left(\frac{U_{p_3}}{\Delta p_t}\right)^2 + \left(\frac{U_{p_6}}{\Delta p_t}\right)^2$$
$$+ \left[\left(\frac{p_6 - p_3}{\Delta p_t} + \frac{3}{2} \frac{\rho Q_J^2}{\Delta p_t} \cdot \left(\frac{\beta_{E6} + C_{pc6}}{A_6^2} - \frac{\beta_{E3}}{A_3^2} \right) \right) \cdot \frac{U_{Q_J}}{Q_J} \right]^2 \tag{17}$$
$$+ \left(\frac{1}{2} \frac{\rho Q_J^2}{\Delta p_t A_3^2} \cdot U_{\beta_{E3}} \right)^2 + \left(\frac{1}{2} \frac{\rho Q_J^2}{\Delta p_t A_6^2} \cdot U_{\beta_{E6}} \right)^2 + \left(\frac{1}{2} \frac{\rho Q_J^2}{\Delta p_t A_6^2} \cdot U_{C_{pc6}} \right)^2$$

and the uncertainty in the power coefficient, P^*, is

$$\left(\frac{U_{P^*}}{P^*}\right)^2 = \left(\frac{U_Q}{Q}\right)^2 + \left(2\frac{U_n}{n}\right)^2 \tag{18}$$

The uncertainties were calculated for all measured data points, and the typical range of the calculated uncertainties is listed in Table 2. These uncertainties will also be shown in the results section. The lower uncertainties for H^* and η occur at lower Q^* and the higher uncertainties are at the higher flow rates. This occurs since many of the uncertainty terms are proportional to the flow rate, and inversely proportional to the head rise in the pump. The sources of the uncertainty in pump efficiency are listed in Table 3. The largest

source of uncertainty for η is the uncertainty in flow rate, Q_J. This term accounts for greater than 80% of the total uncertainty. The uncertainty in flow rate is also the single largest contributor to the uncertainty in the headrise coefficient, H^*.

Table 2. Typical range of calculated uncertainties.

Item	Uncertainty
P^*	0.3%
Q^*	0.7%
H^*	1.4 – 2.1%
η	1.5 – 2.2%

Table 3. Typical source of uncertainties in pump efficiency.

RPM	Q^*	Total Uncertainty	Uncertainty Contribution							
			n	Q	p_3	p_6	Q_J	β_{E3}	β_{E6}	C_{pc6}
1400	0.711	1.53%	0.02%	0.30%	0.37%	0.16%	1.37%	0.08%	0.39%	0.26%
1400	0.848	2.12%	0.02%	0.30%	0.48%	0.19%	1.85%	0.13%	0.68%	0.45%
1400	0.920	2.63%	0.02%	0.30%	0.58%	0.22%	2.27%	0.18%	0.92%	0.62%

Thrust Breakdown

The uncertainty for the calculated quantity N^* is found using the same standard uncertainty analysis as for the other calculated quantities.

$$\left(\frac{U_{N^*}}{N^*}\right)^2 = \left(\frac{U_\rho}{\rho}\right)^2 + \left(\frac{U_n}{n}\right)^2 + \left(\frac{U_{p_3}}{PSIA - p_3 - p_v + \frac{K \cdot V_3^2}{2}}\right)^2 + \left(\frac{U_{PSIA}}{PSIA - p_3 - p_v + \frac{K \cdot V_3^2}{2}}\right)^2$$
$$+ \left(\frac{U_{P_v}}{PSIA - p_3 - p_v + \frac{K \cdot V_3^2}{2}}\right)^2 + \left(\frac{K \cdot U_{PSID}}{2 \cdot \left(PSIA - p_3 - p_v + \frac{K \cdot V_3^2}{2}\right)}\right)^2 \tag{19}$$

The uncertainties for the measured quantities in the equation above are listed in Table 1. The results of the uncertainty analysis yield uncertainties in N^* ranging from 0.66% to 1.27% for the thrust breakdown runs with the higher uncertainties corresponding to the lower flow rate conditions.

The uncertainty in the calculation of $N^*_{1\%}$ was calculated as the greater of two quantities: the uncertainty in Q divided by the slope of the thrust breakdown curve in the region of $Q/Q_0 = 0.99$, and the uncertainty in N^*. In all cases the uncertainty in N^* was greater than the uncertainty for $N^*_{1\%}$ for each of the nozzle flow rate conditions is given in Table 4.

Table 4. Uncertainty in $N^*_{1\%}$.

Condition	$N^*_{1\%}$ Uncertainty
100% Nozzle	0.73%
90% Nozzle	0.87%
80% Nozzle	1.20%

RESULTS

Flow Rate
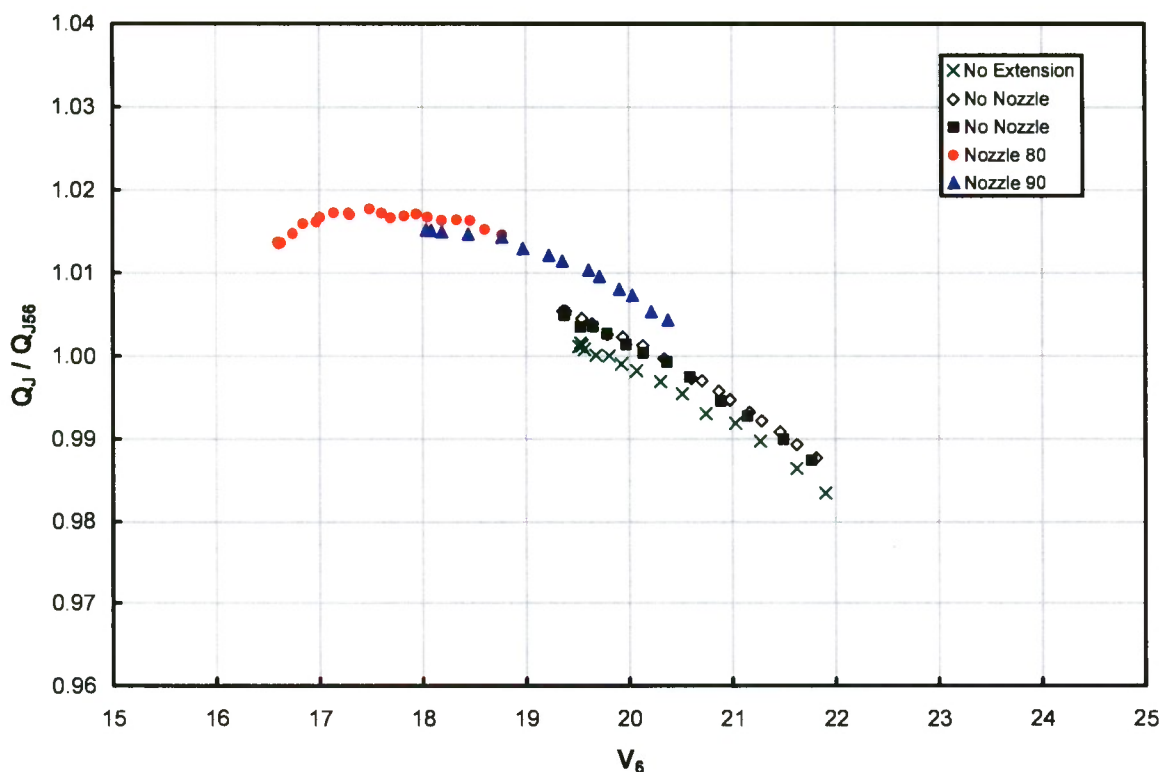
Fig. 17. Ratio of flowrate calculated from bellmouth vs. from nozzle.

Flow rates through the pump were calculated from the pressure differential across the upstream bellmouth inlet as outlined in the *Procedure: Data Reduction* section. In theory, flow rate could also be calculated from the pressure differential across the pump nozzle. Using the nozzle pressure differential would be advantageous for other pump system tests, such as in tow tank tests and shipboard tests, where the bellmouth inlet is not used. If uniform flow is assumed at stations 5 and 6, and the pressure loss is presumed to be proportional to the dynamic head

$$Q_{J56} = \sqrt{\frac{2(p_5 - p_6)}{\rho} \cdot \frac{A_5^2 A_6^2}{A_5^2 - mA_6^2}} = const \cdot \sqrt{\frac{p_5 - p_6}{\rho}} \tag{20}$$

where $1 - m$ is the fraction of dynamic head lost from station 5 to station 6. The flow rate calculated in this way, assuming no losses in the nozzle ($m = 1$) is plotted against the flow rate calculated from the bellmouth pressure

differential in Fig. 17. The figure shows that the flow rate calculated from the nozzle matches that from the bellmouth to only ±2%. The ratio between the two flow rates is not a constant, so including a loss factor through the nozzle or adjusting the flow areas will not improve the match. It appears that the character of the flow changes with flow rate, making the nozzle pressure drop not ideally suited for measuring flow rate.

Flow Fields

Station 3

The velocity ahead of the rotor at station 3 was measured with the purpose of calibrating the bellmouth flow coefficient, and quantifying the flow non-uniformity. Previous measurements in this facility with this bellmouth inlet showed the inflow to the pump to be uniform in the circumferential coordinate. Thus, to characterize the flow at station 3, only a line survey of the velocity was required. Measurements of the axial velocity at station 3 at $Q^* = 0.783$ are shown in Fig. 18. Velocity in this figure has been normalized by the average velocity for the flow. Over about 85% of the radius the axial velocity is $1 - 2\%$ higher than the average velocity, while at the small regions near the casing and the shaft the velocity is lower. The profiles are nearly identical for other measured speeds.

These measurements were used to calculate the velocity non-uniformity coefficients at station 3. The coefficients were nearly identical for all measured speeds, with $\beta_{M3} = 1.004$ and $\beta_{E3} = 1.011$.
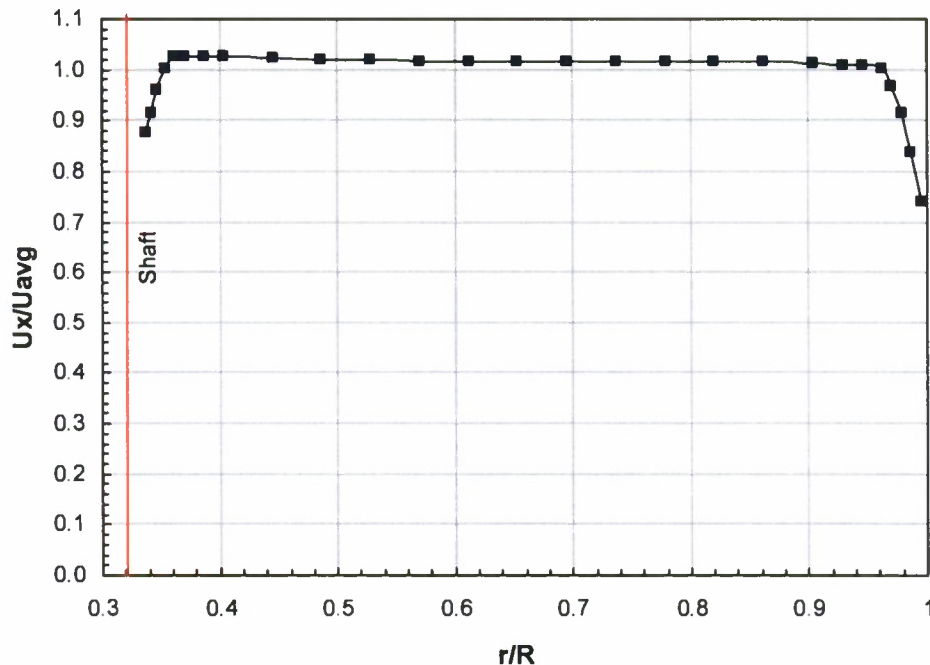
Fig. 18. Axial velocity variation with for station 3 pump inlet flow, from LDV, $Q^* = 0.783$.

Station 6

Velocity data were acquired at station 6 for two flow conditions, $Q^* = 0.850$ and 0.938. These data are shown in Figs. 19 – 22. The flowfields as measured are shown in Figs. 19 and 20, and the flowfields with the missing data at the top and bottom of the jet filled in as described in the *Data Reduction* section are shown in Figs. 21 and 22. In these figures, the stator and hub wakes are clearly visible. The flowfields are very similar for both flow conditions. The only notable difference, other than the generally higher velocity at the higher flow rate, is the slightly stronger hub vortex at $Q^* = 0.850$. At the lower flow rate, the axial velocity is a bit lower, and the negative swirl (in the opposite direction of the rotor motion) is a little greater. These differences are better seen in the plot of the circumferential average velocity, Fig. 23. In the outer portion of the flow, swirl is nearly zero. As the hub is approached, the swirl first becomes positive, and then negative. This results in swirl angles of from -6° to +4°, as seen in Fig. 24. The mild level of swirl and the low velocity deficit at the center of the flowfield show that there is no strong hub vortex.

The circumferential average flow at station 6 as calculated with both Fluent and CFX is shown in Figs. 25 and 26. The CFX calculated axial velocity matches the measured velocity well outside the hub wake, but the tangential velocity magnitude and the axial velocity wake deficit are overpredicted near the hub. The Fluent calculated axial velocity also matches the measured velocity well outside the hub wake, but the tangential velocity magnitude matches the measured less well, and the differences near the hub are more pronounced. It should be noted that the Fluent domain only extends from about 6% radius on out. The Fluent computational domain had a rather large center body after the hub in order to avoid singularities in the grid at zero radius. The CFX domain included a center body as well, but it extended only to $r/R = 0.0015$. The center body in the Fluent calculation appears to significantly distort the flow near the hub.

The calculated circumferential average pressure through the stator and nozzle are shown in Figs. 27 and 28. These plots show that the relatively long nozzle has allowed the flow to equilibrate by the nozzle exit, and that the pressure field is nearly uniform at station 6. This is better illustrated in the plot of the pressure at station 6, Fig. 26. The CFX results show a nearly uniform pressure at station 6, while the Fluent results show the pressure increasing slightly from wall to hub. Since in other comparisons, the CFX results match the experimental data better than the Fluent results,, one would tend to give greater credence to the CFX results. It may be that the constant pressure boundary condition at the exit of the Fluent computational domain may be overly restrictive. It would therefore be expected that the wall pressure measured in the test should be very close to the average pressure at station 6.

The energy non-uniformity coefficients calculated from integrating the measured flow fields are shown in Table 5. The coefficients for both cases are very close. For pump performance calculations a value of $\beta_{E6} = 1.016$ was used. Most of the non-uniformity comes from the variation in axial velocity. For this pump, the secondary flow contributes very little to β_{E6}.
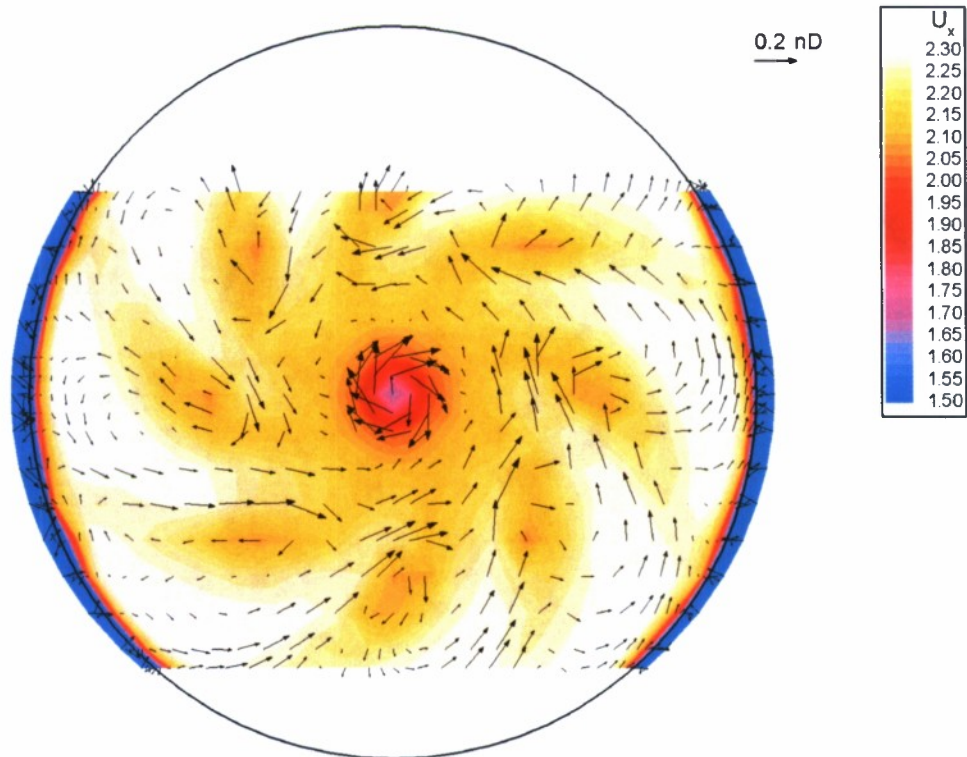
Fig. 19. Measured flow, station 6, $Q^* = 0.850$.
Velocity measurements at tail of each shown vector. Velocity normalized by nD.
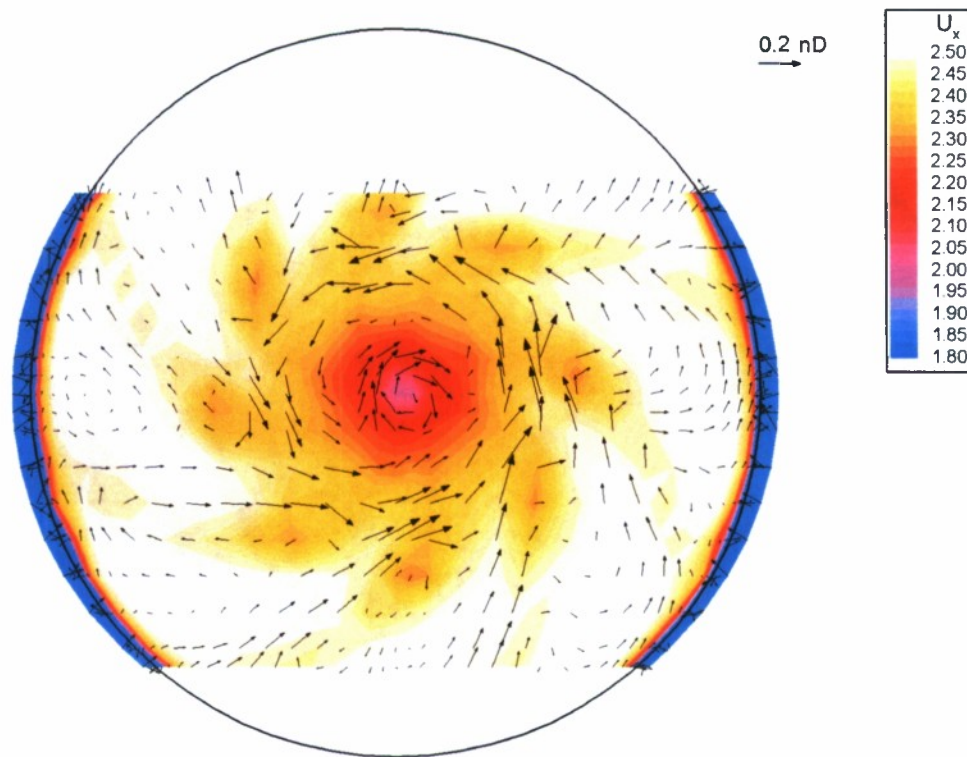
Fig. 20. Measured flow, station 6, $Q^* = 0.938$.
Velocity measurements at tail of each shown vector. Velocity normalized by nD.
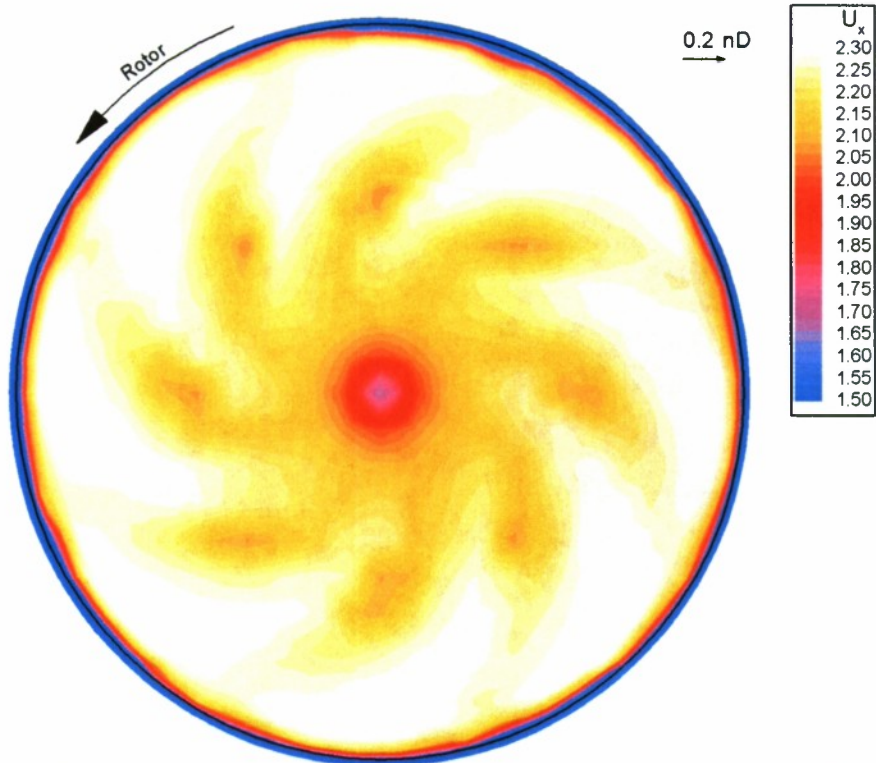
Fig. 21. Measured flow, station 6, $Q^* = 0.850$, with missing data filled.
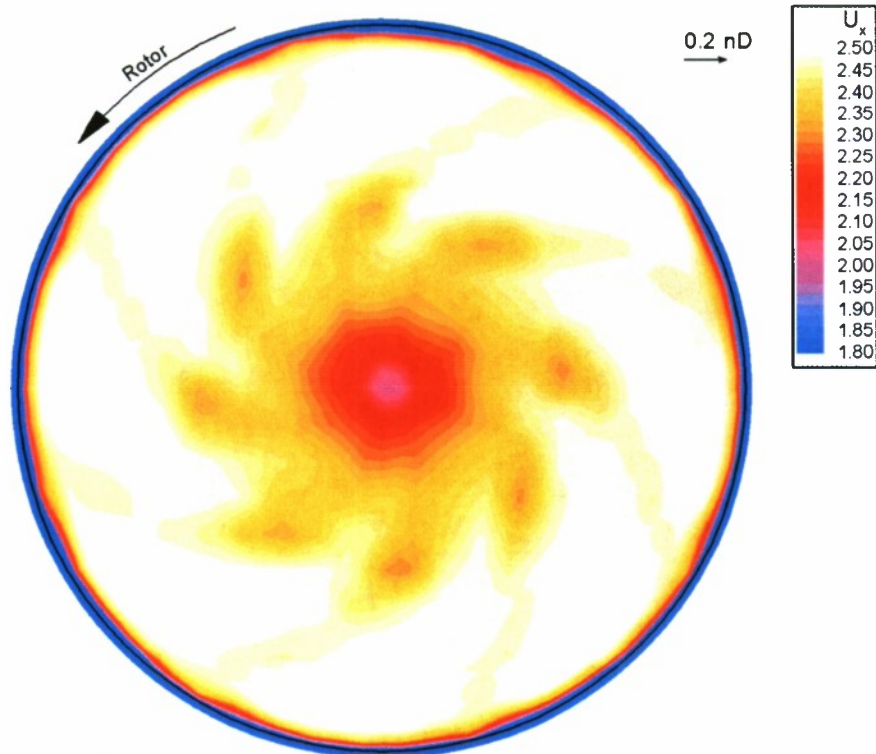
Fig. 22. Measured flow, station 6, $Q^* = 0.938$, with missing data filled.
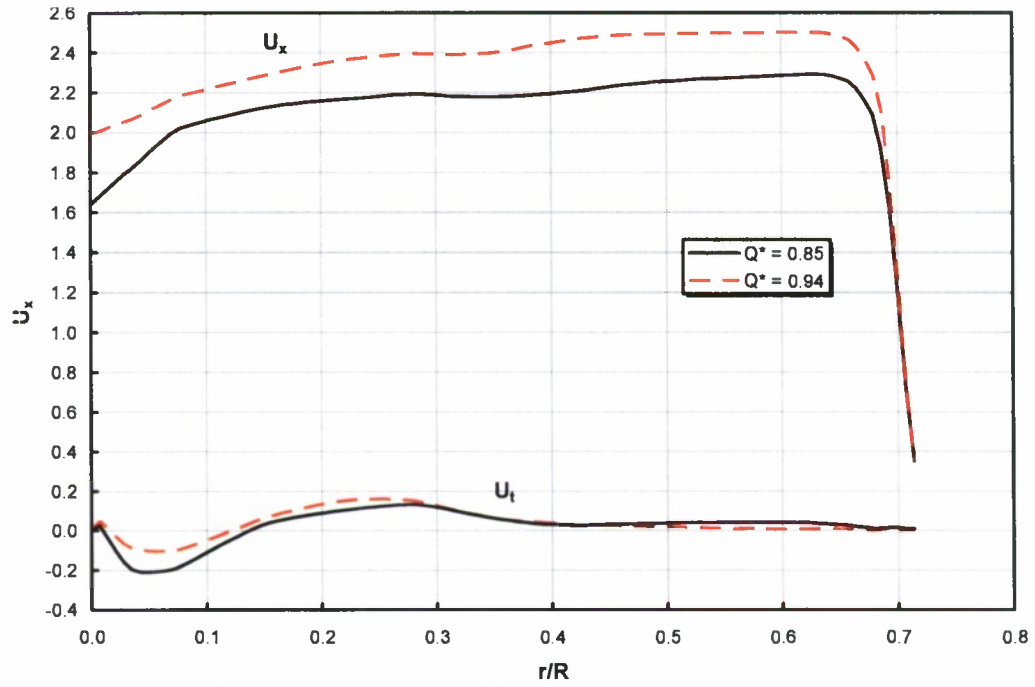
Fig. 23. Circumferential average velocity, station 6.
Velocity normalized by *nD*.
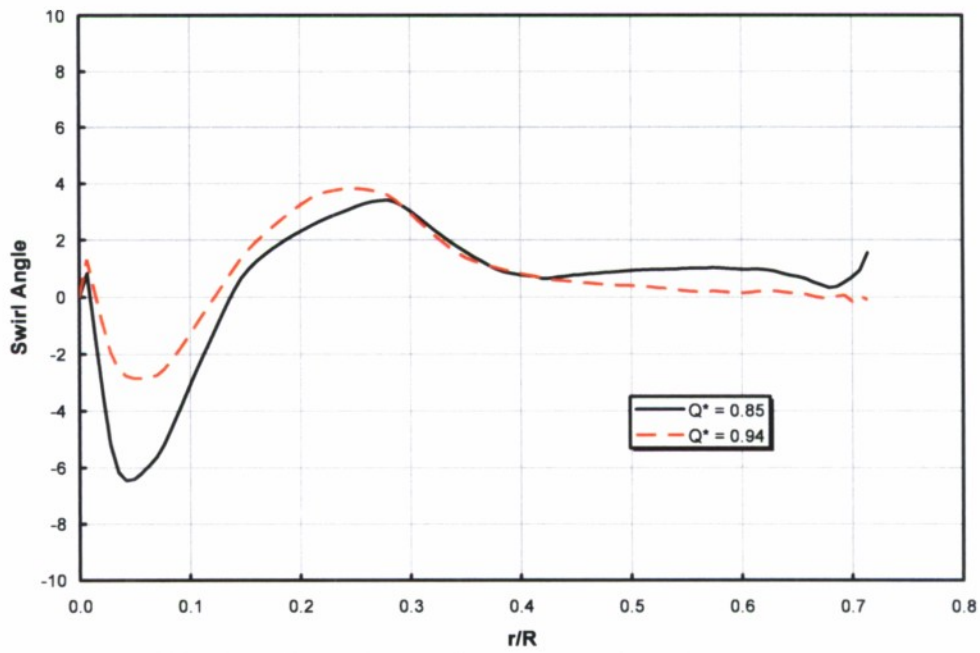
Fig. 24. Circumferential average swirl angle, station 6.
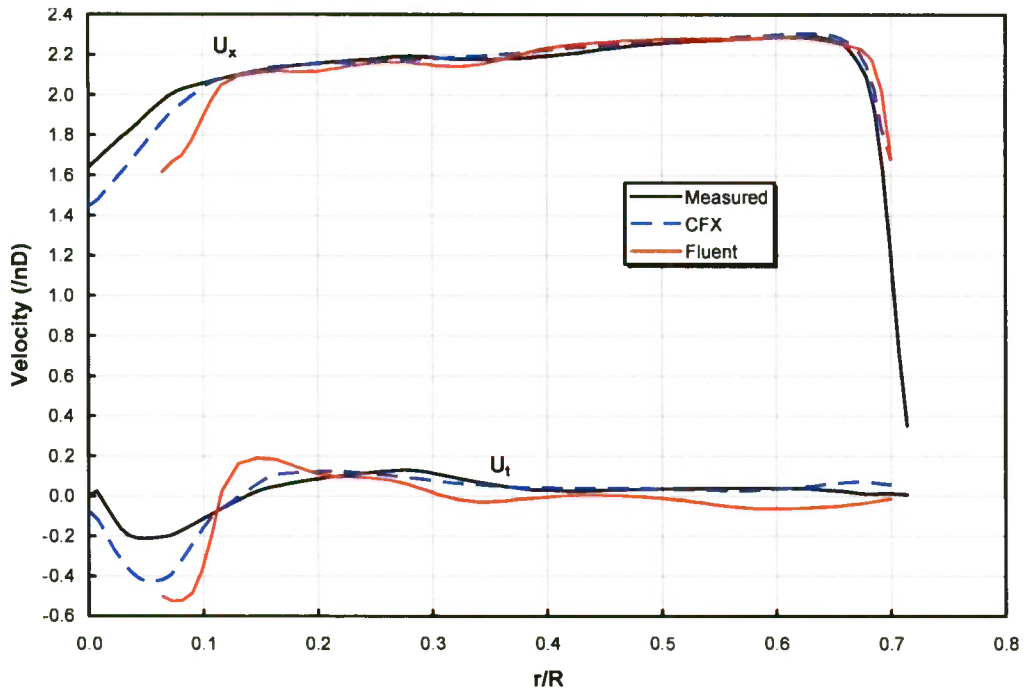
Fig. 25. Circumferential average velocity, station 6, $Q^* = 0.85$.
Velocity normalized by nD.
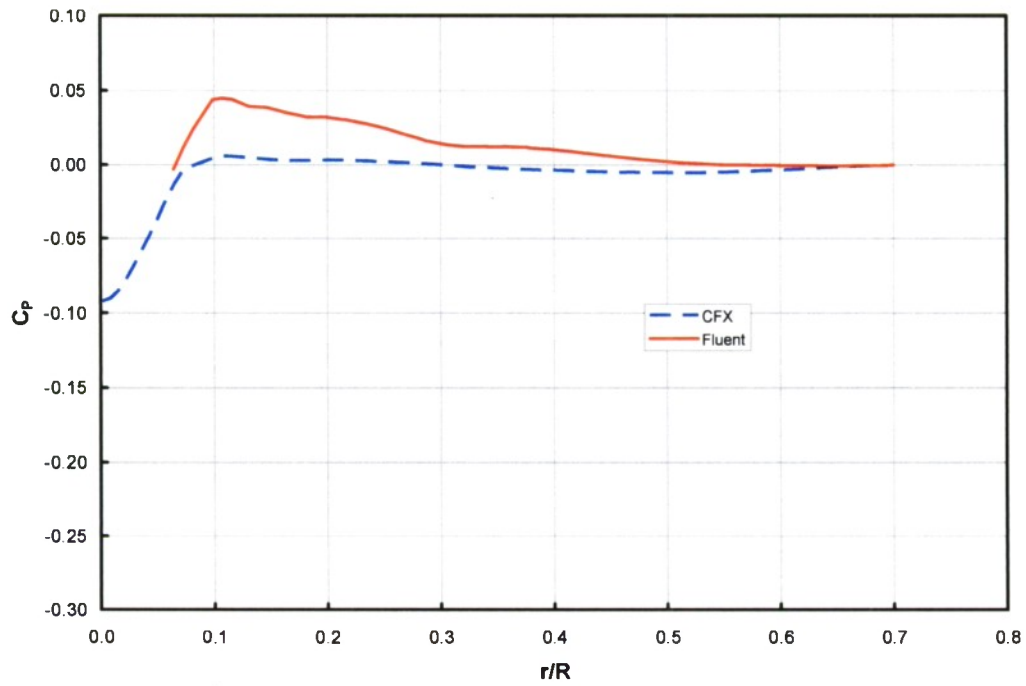
Fig. 26. Circumferential average pressure, station 6, $Q^* = 0.85$.
Pressure relative to wall pressure, normalized by $\rho V_6^2/2$.
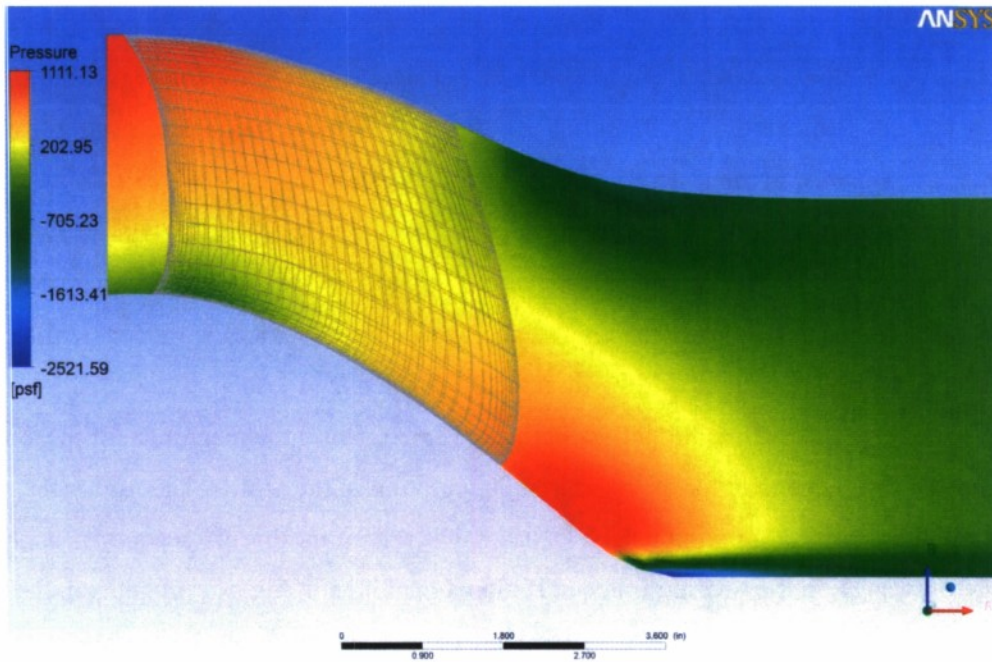
Fig. 27. Circumferential average pressure through stator and nozzle, from CFX, $Q^* = 0.85$.
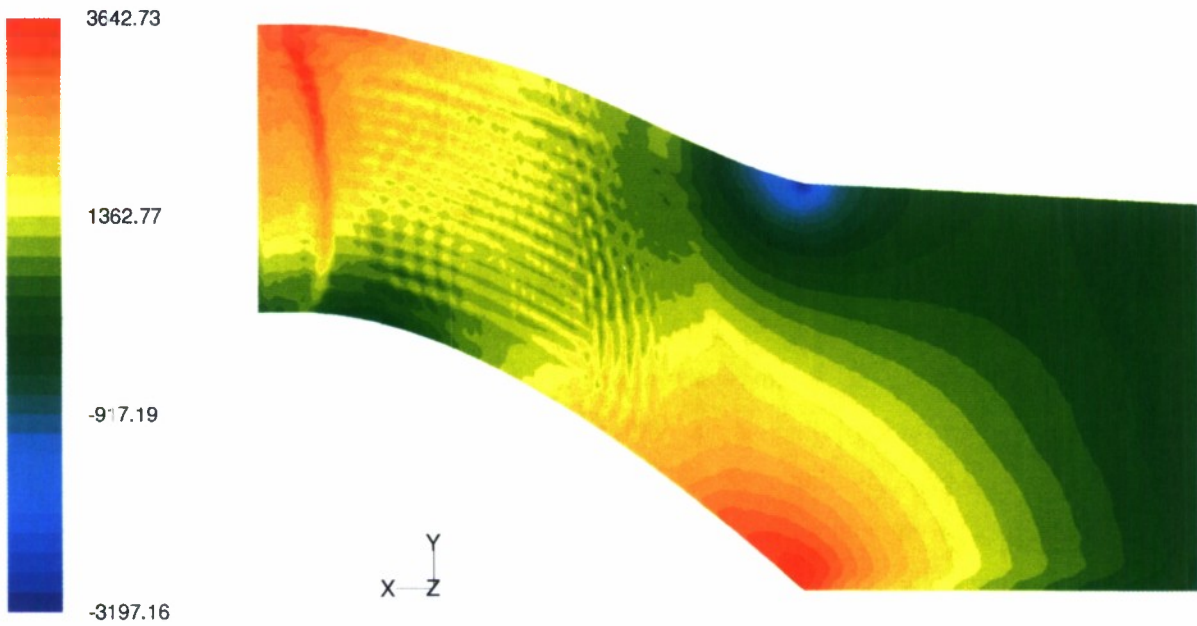
Fig. 28. Circumferential average pressure through stator and nozzle, from Fluent, $Q^* = 0.85$.

Table 5. Flowfield velocity integrations, station 6.

Q^*	Q_J (ft^3/s)	Rotor RPM	Impeller RPM	β_M	β_{Ex}	β_{Et}	β_{Er}	β_E
0.850	19.83	1400	53.3	1.005	1.014	0.001	0.001	1.016
0.938	21.89	1400	140	1.005	1.014	0.001	0.000	1.015

Station 4

Measurements of the flow between the rotor and stator at station 4 are shown in Figs. 29 – 39. The circumferentially averaged velocities are shown in Figs. 29 – 31, and the velocities resolved into the rotating frame of the rotor, as explained in the *Data Reduction* section, are shown in Figs. 32– 39.

The measured circumferential average axial velocity is plotted in Fig. 29 along with the values calculated with Fluent. The tangential velocity is similarly plotted in Fig. 30. The axial velocities are nearly constant across the blade span outside of the hub and tip regions. The calculated velocities are very similar to those measured with the following exceptions. At the tip region, the calculated velocities deviated from the measured, presumably due to the complex nature of the flow in the tip region. Also, the magnitude of the axial velocity is slightly higher for the computed than for the measured. Integration of the profiles shows that the measured circumferential axial velocity was approximately 3% low. The reason for this discrepancy is unclear.

The average flow angle in the rotating frame at station 4 is plotted in Fig. 31. In general, the relative flow angle decreases from hub to tip, and is from 5° to 10° higher than the blade pitch angle. The relative flow angle varies only slightly with Q^*. As explained in the *Data Reduction* section, in order to view the secondary flow, it is first necessary to define a primary flow direction. That primary flow direction is defined here with a curve fit to the circumferentially averaged relative flow angle for $Q^* = 0.772$ plotted in Fig. 31. The curve fit yields

$$\phi_0 = -27066 + 226178r - 775858r^2 + 1404662r^3 - 1417733r^4 + 757005r^5 - 167165r^6 \qquad (21)$$

where ϕ_0 is in degrees and r is normalized by the pump radius R.

The station 4 flowfields in the rotating frame of the rotor are shown in Figs. 32 – 39. Figs. 32 – 34 show the streamwise velocity, V_S^*, for the entire measured propeller disc for the three measured flow conditions. Each of these plots consists of a grid of 55 × 1024 points. In all three plots, the low-velocity regions six blade wakes are clearly visible, as are the boundary layers at the hub and the wall. At the wall, between the blade wakes, lies a region of low velocity which is due to the tip leakage flow. As the flow goes from the design Q^* of 0.850 to the higher loading condition of $Q^* = 0.712$, the blade wake near the root becomes much thicker, and the region of low velocity from the tip leakage flow comes closer to the blade and becomes much more pronounced. In comparison to pumps previously measured at NSWCCD[8], these figures show that at the design flow rate of $Q^* = 0.850$ the rotor wakes are relatively thin and the secondary flows are relatively mild.

The plots of single blade wakes in the pitch-normal projection, Figs. 35 and 36, show this more clearly, and also show that the blade wake becomes weaker near the outer blade radii as Q^* decreases. In these figures, the secondary flow vectors have been plotted only for $Q^* = 0.850$ since they are difficult to discern at this scale. The vectors show that the flow moves radially outward in the blade wake, and that there is considerable swirl near the blade tip.

The plots of the flow at the blade tip region, Figs. 37 – 39, show that the tip trailing edge vortex is distinct from the leakage flow. The trailing edge vortex is located very near the blade wake, and the leakage flow is

farther from the blade wake and exhibits very little streamwise vorticity.   At the low flow rate of $Q* = 0.712$, these two regions are starting to merge.
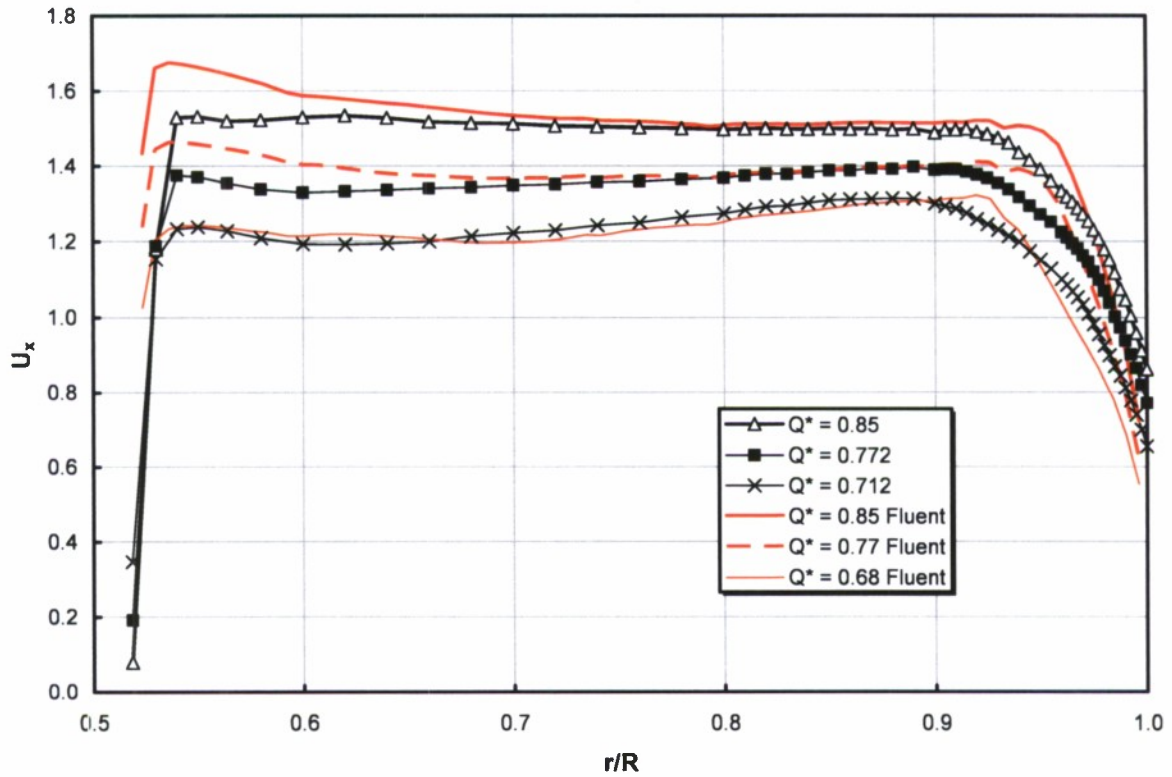
Fig. 29.   Circumferential average axial velocity, station 4.
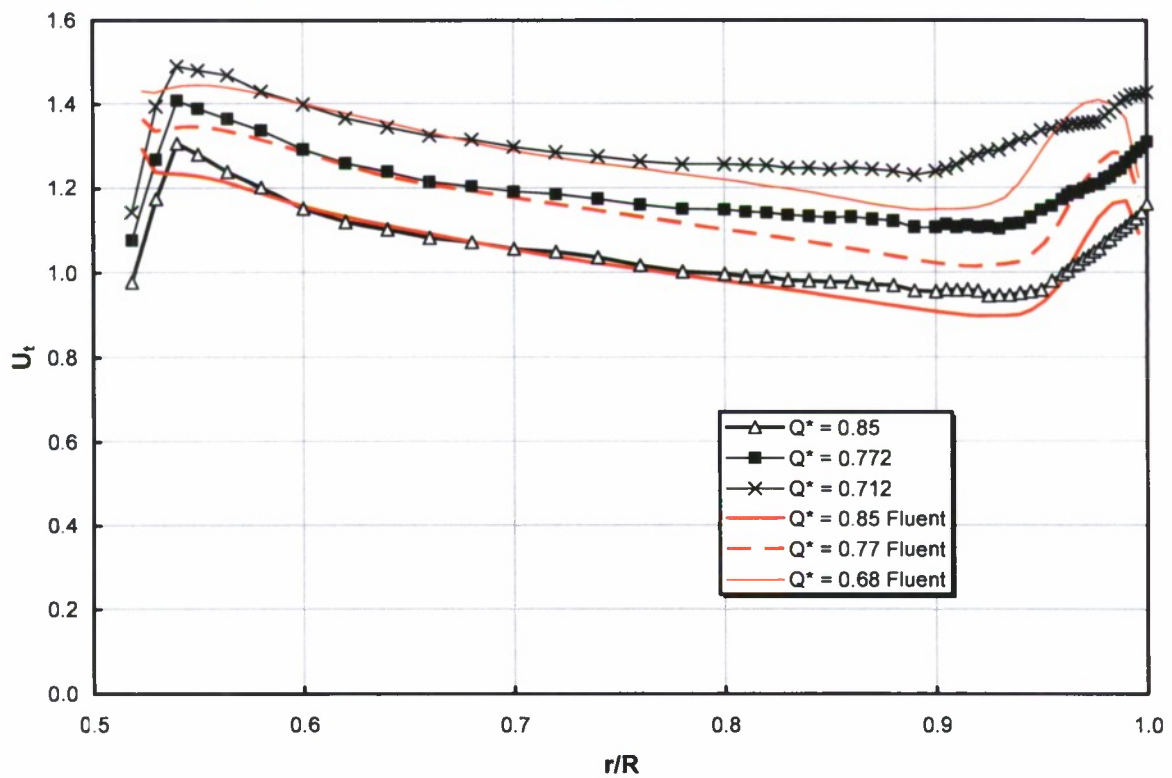
Fig. 30.   Circumferential average tangential velocity, station 4.
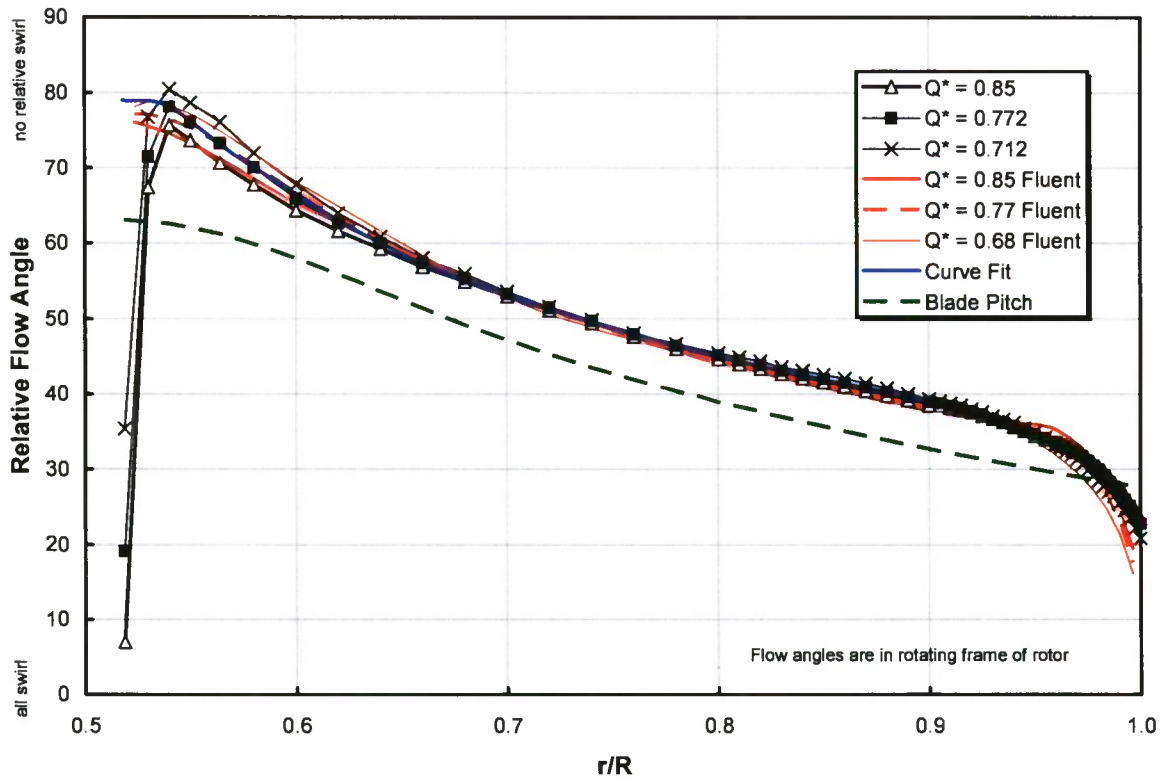
Fig. 31. Circumferential average flow pitch angle, station 4.
"Curve Fit" line used to determine streamwise flow angle, ϕ_0, on all station 4 plots.
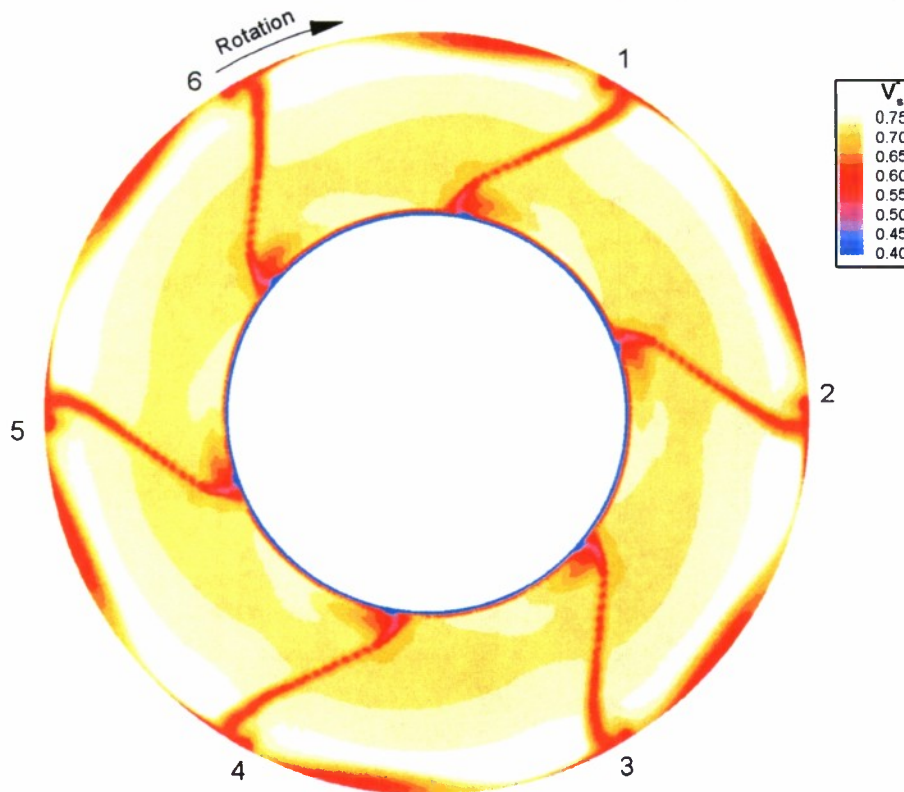
Fig. 32. Streamwise velocity measured at station 4, Q^*=0.85.
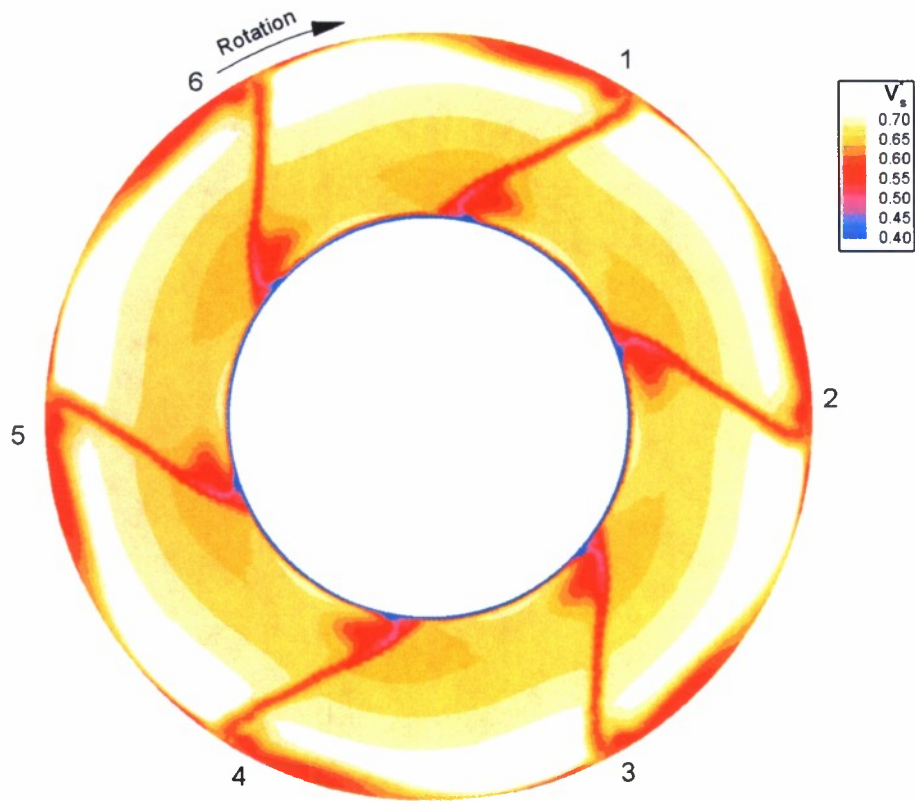
Fig. 33. Streamwise velocity measured at station 4, $Q^*=0.772$.
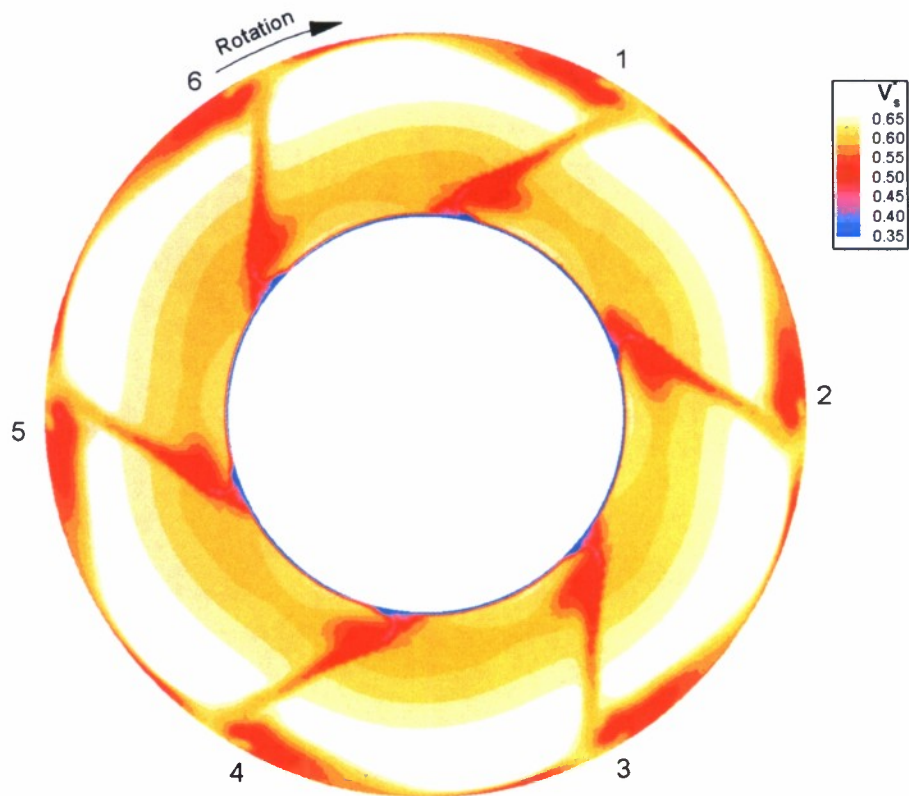
Fig. 34. Streamwise velocity measured at station 4, $Q^*=0.712$.
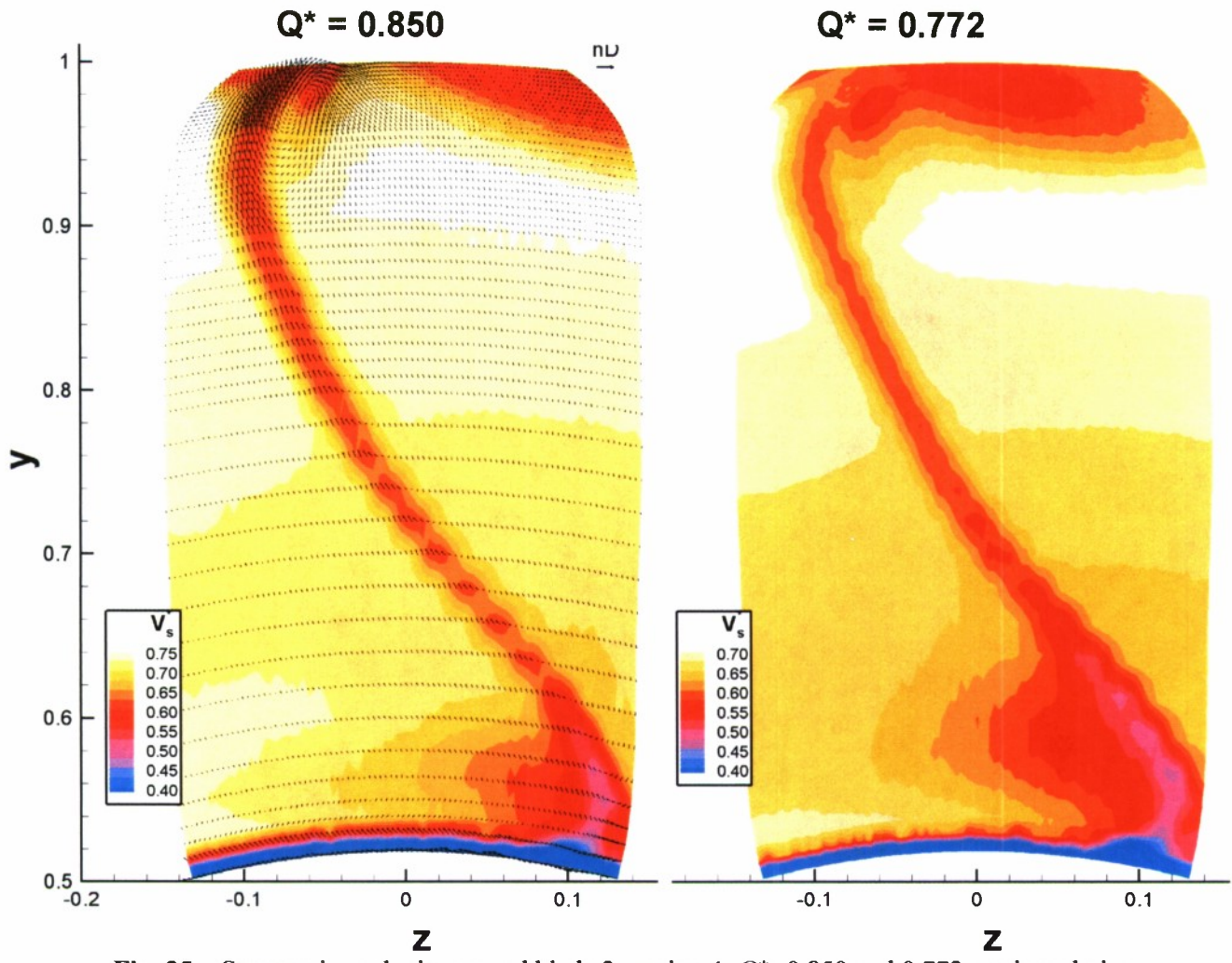
Fig. 35. Streamwise velocity around blade 2, station 4, Q^*=0.850 and 0.772, projected view.
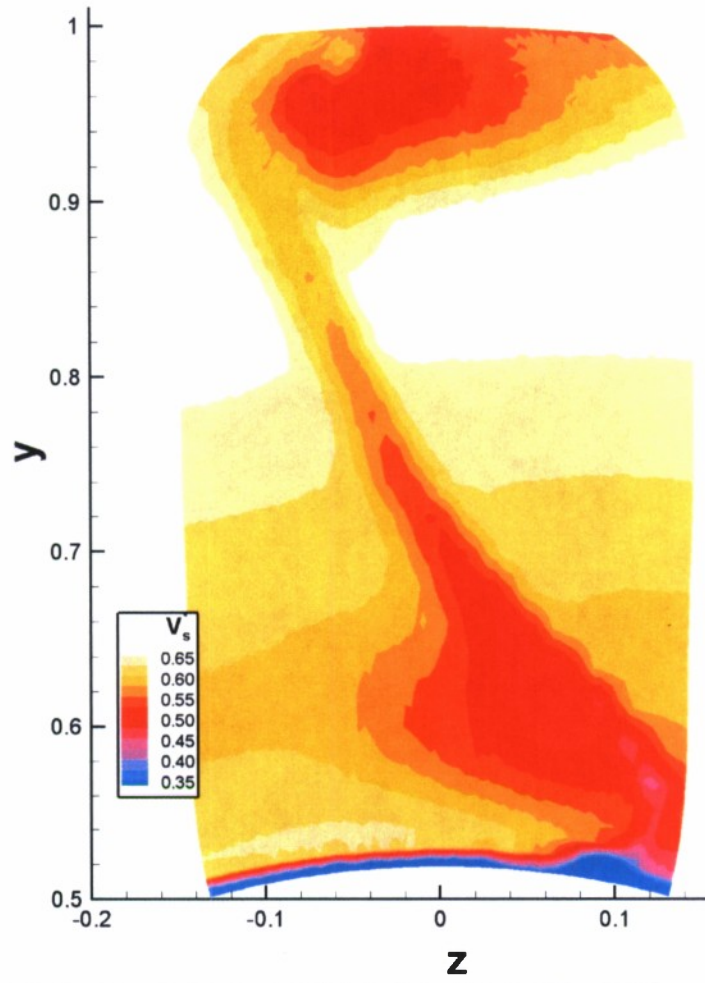
Fig. 36. Streamwise velocity around blade 2, station 4, $Q^* = 0.712$, projected view.
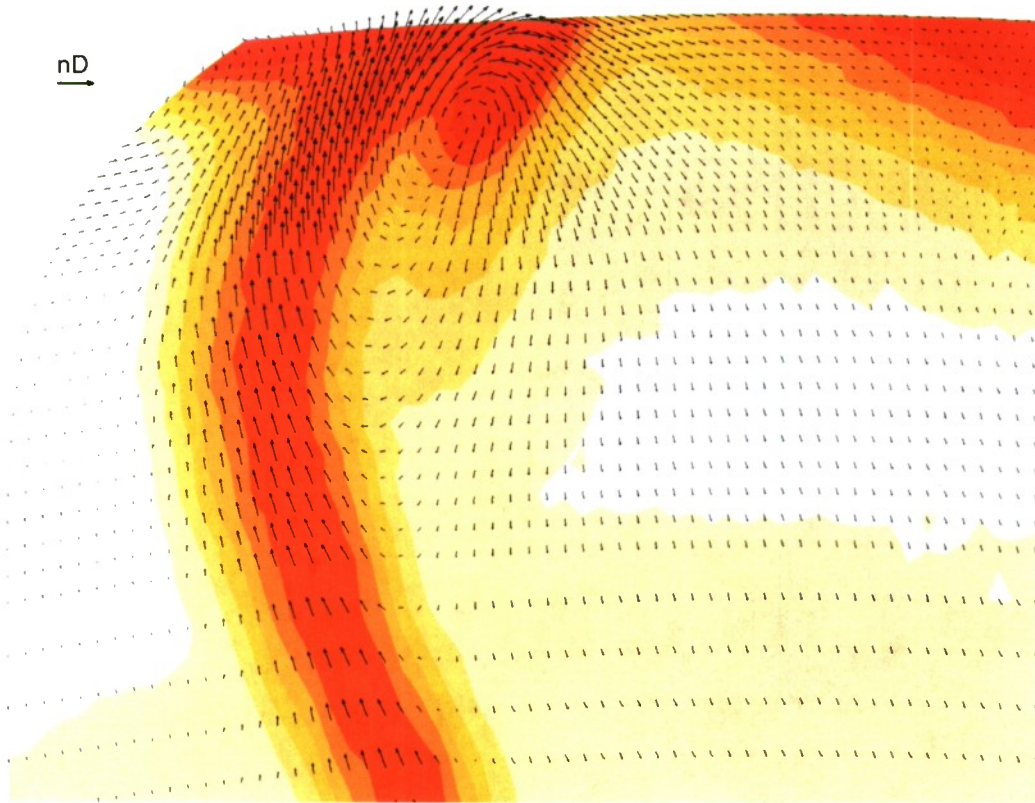
Fig. 37. Streamwise velocity around blade 2 tip, station 4, $Q^*=0.850$, projected view.
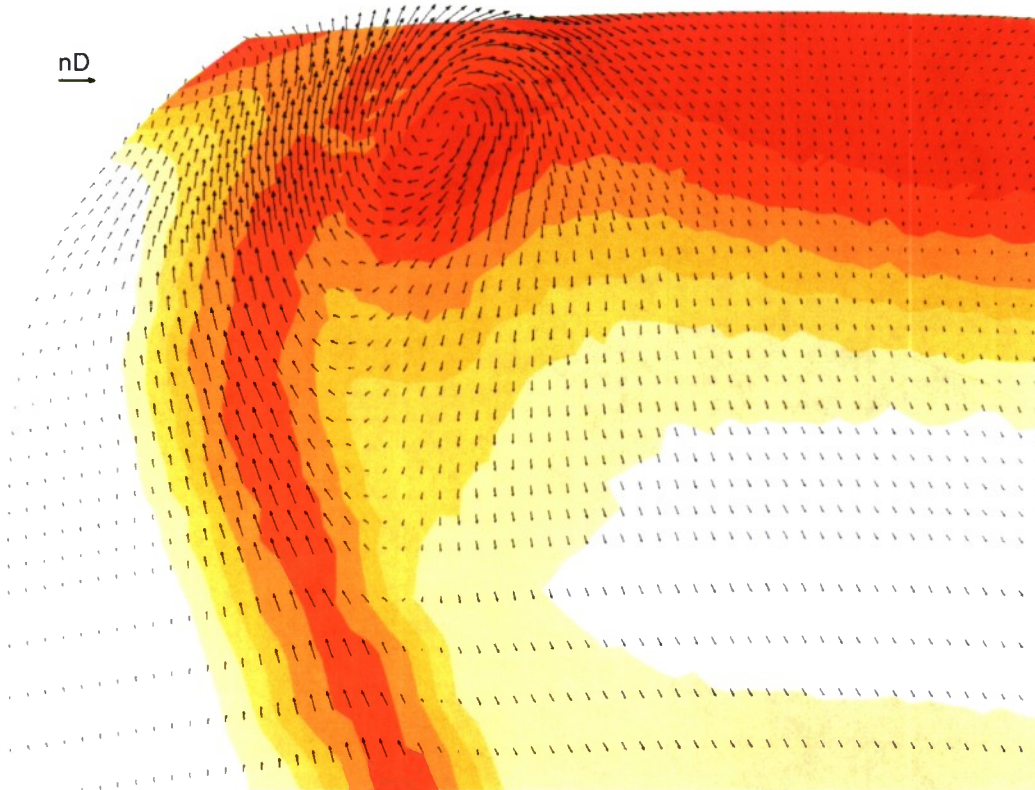
Fig. 38. Streamwise velocity around blade 2 tip, station 4, $Q^*=0.772$, projected view.
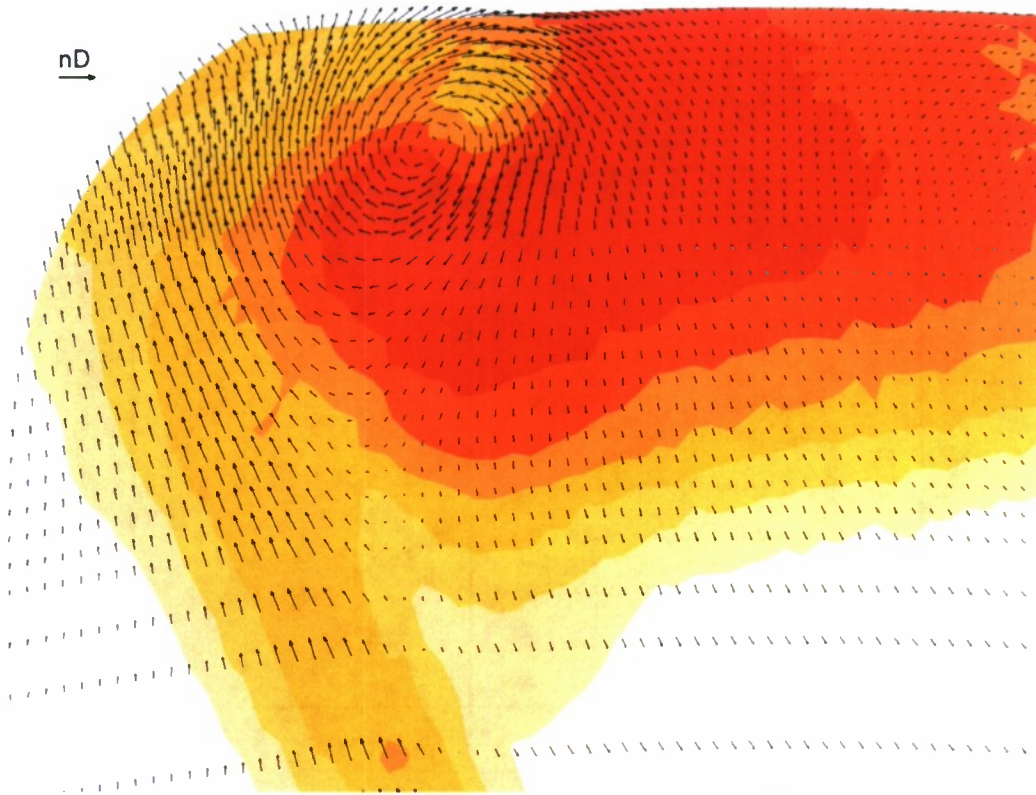
Fig. 39. Streamwise velocity around blade 2 tip, station 4, Q^*=0.712, projected view.

Pump Powering Performance

The pump powering performance calculated from the measurements in the 36-Inch Variable Pressure Water Tunnel is shown in Fig. 40. Pump performance was found using the method outlined in the *Data Analysis* section, and was calculated by combining data from shaft dynamometry, pressure measurements, and laser velocity measurements. Data from three flow-control nozzle configurations — nozzle extension only, 90% area nozzle, and 80% area nozzle — are shown in the plot. Data from the no flow-control nozzle configuration covers the region of $0.830 \leq Q^* \leq 0.935$, data from the 90% area flow-control nozzle configuration covers the region of $0.773 \leq Q^* \leq 0.873$, and data from the 80% area flow-control nozzle configuration covers the region of $0.711 \leq Q^* \leq 0.804$. On these plots the solid black lines are curve fits to the data, and the dashed black lines show the uncertainty bands. No uncertainty bands are shown for P^*, since the uncertainty is on the order of the size of the symbols. Peak efficiency of 89% occurs at flow coefficient, Q^*, equal to 0.76.
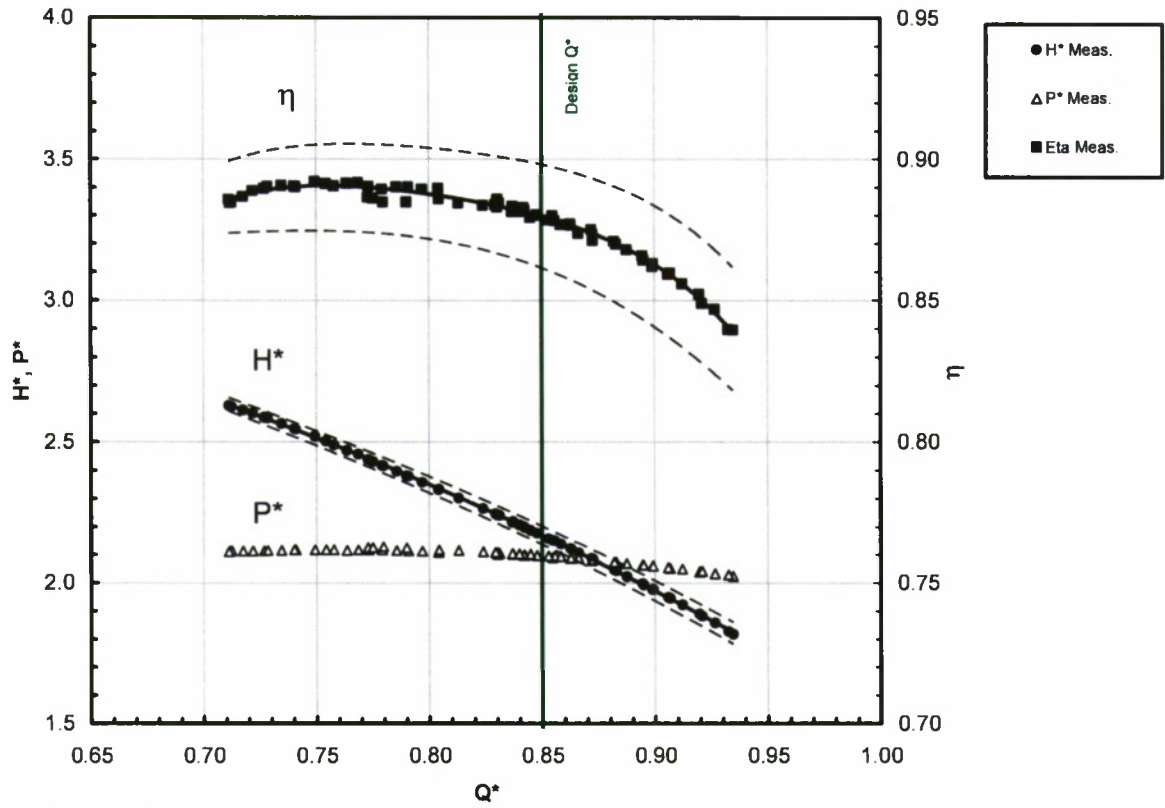
Fig. 40. Measured pump head, power, and efficiency, with uncertainty bands.
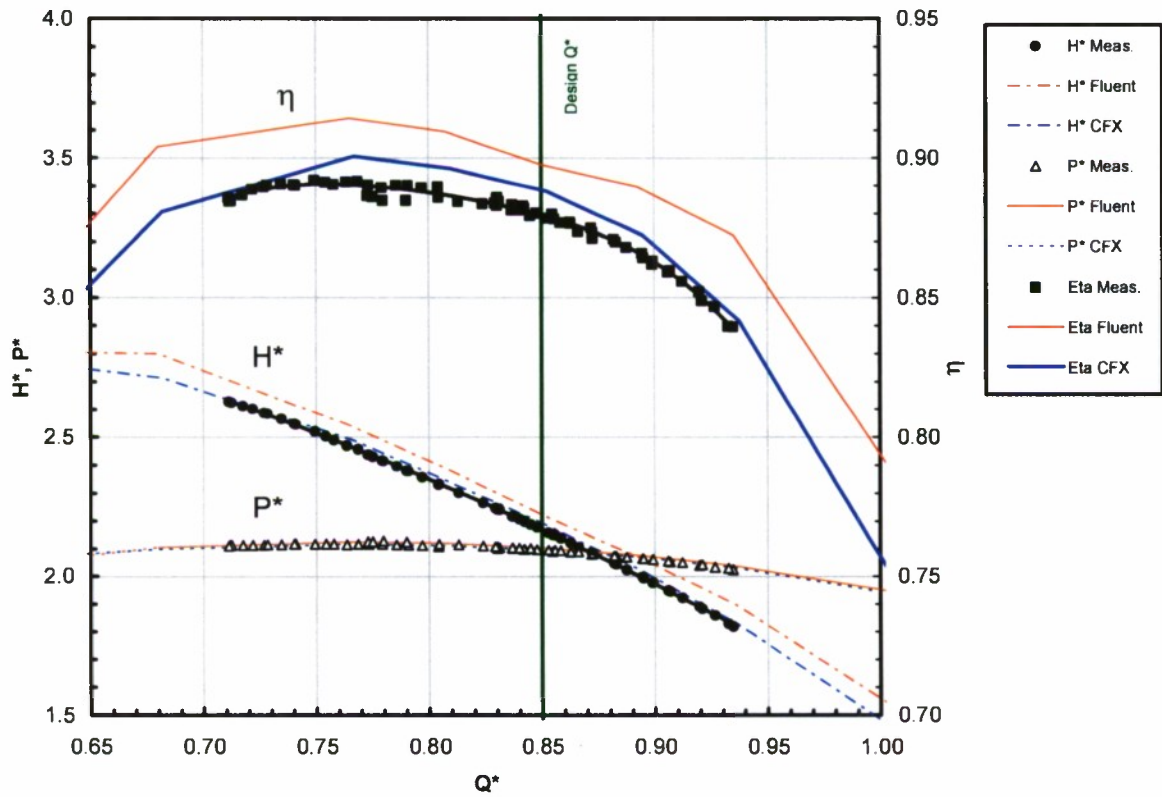
Fig. 41. Measured and calculated pump head, power, and efficiency.

The measured performance is shown along with the predicted performance from the Fluent (in red) and CFX (in blue) calculations in Fig. 41. The CFX solution predicts pump performance very close to that measured in the 36-inch VPWT; both the head and the efficiency predictions fall within the uncertainty bands of the measured data. The Fluent calculations predict both head rise and efficiency a bit higher than that measured, with the predicted efficiency about 2.5% higher than the measured values.

The results plotted in Fig. 40. account for the non-uniform distribution of energy in the flow through the energy non-uniformity factors, β_{E3} and β_{E6}. If these factors had not been used, and the flow energy was calculated from the average velocity, the head rise and efficiency would be about 1.3% lower. The non-uniformity at station 6 was relatively low with this pump due to good stator design and the relatively long nozzle. More typical pumps with larger non-uniformity in the nozzle flow would see a larger discrepancy in measured performance using the uniform flow assumption.

Cavitation Performance

Thrust Breakdown

Thrust breakdown runs were performed for each of the flow rate restriction conditions: 100% nozzle, 90% nozzle, 80% nozzle, and nozzle extension removed as summarized in Table 6. The nozzle extension removed condition results were very similar to that of 100% nozzle and are not included in this report.

Torque, headrise, and thrust all drop off at low N^* due to the effects of cavitation. The drop in torque and thrust are measured directly, while headrise, represented non-dimensionally as H^*, is a calculated quantity. Loss of pump performance, or thrust breakdown, is defined in the literature several ways: a 1% drop in torque, a 3% drop in headrise, or a 1% drop in efficiency. The definition of a 1% drop in torque from the non-cavitating torque has the advantage of being a directly measured quantity during the test. Headrise and efficiency are both computed from other measured parameters, adding to their uncertainty. In certain cases these values cannot be computed as the pressure measurements are impacted by the amount of cavitation in the nozzle. Thrust breakdown was therefore defined as when the rotor torque dropped 1% from the value of the torque at high pressure. All approaches, however, will be shown.

Table 6. Thrust breakdown run summary.

Condition	p_0 (psia)	N^*_0	Q^*_0	$N^*_{1\%}$	$N^*_{3\%}$
100% Nozzle	47.61	3.285	0.830	0.993	1.036
90% Nozzle	59.27	4.048	0.774	0.901	0.964
80% Nozzle	59.26	4.047	0.711	0.742	0.913

For a thrust breakdown test it would be preferable to reduce only the static pressure in the pump loop. Due to large amounts of cavitation, the flow rate through the pump is also reduced. Attempts to offset this loss in

flow rate by increasing the tunnel impeller speed were not successful as this device also cavitates and cannot reliably produce the small changes in flowrate required. Therefore, in the thrust breakdown plots shown here, all values of torque, headrise, and thrust are normalized by the non-cavitating values of those quantities at that particular flow rate. Thus, the normalization for each point on the plot changes as the flowrate changes. The quantities used for normalization, T_0, Q_0, and H^*_0 (the non-cavitating values of thrust, torque, and head rise) were calculated as a function of Q^* from a 5th order polynomial fitted to the non-cavitating performance data.
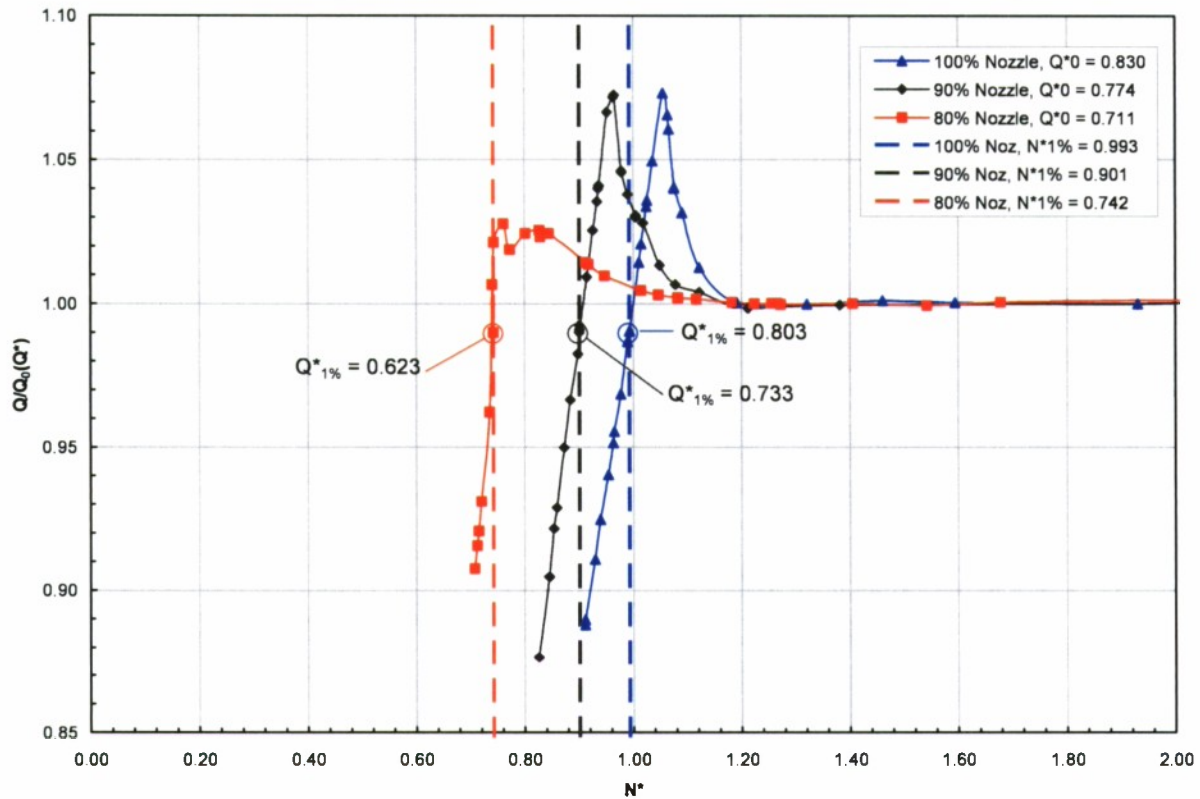
Fig. 42. Normalized impeller torque vs. N^*.
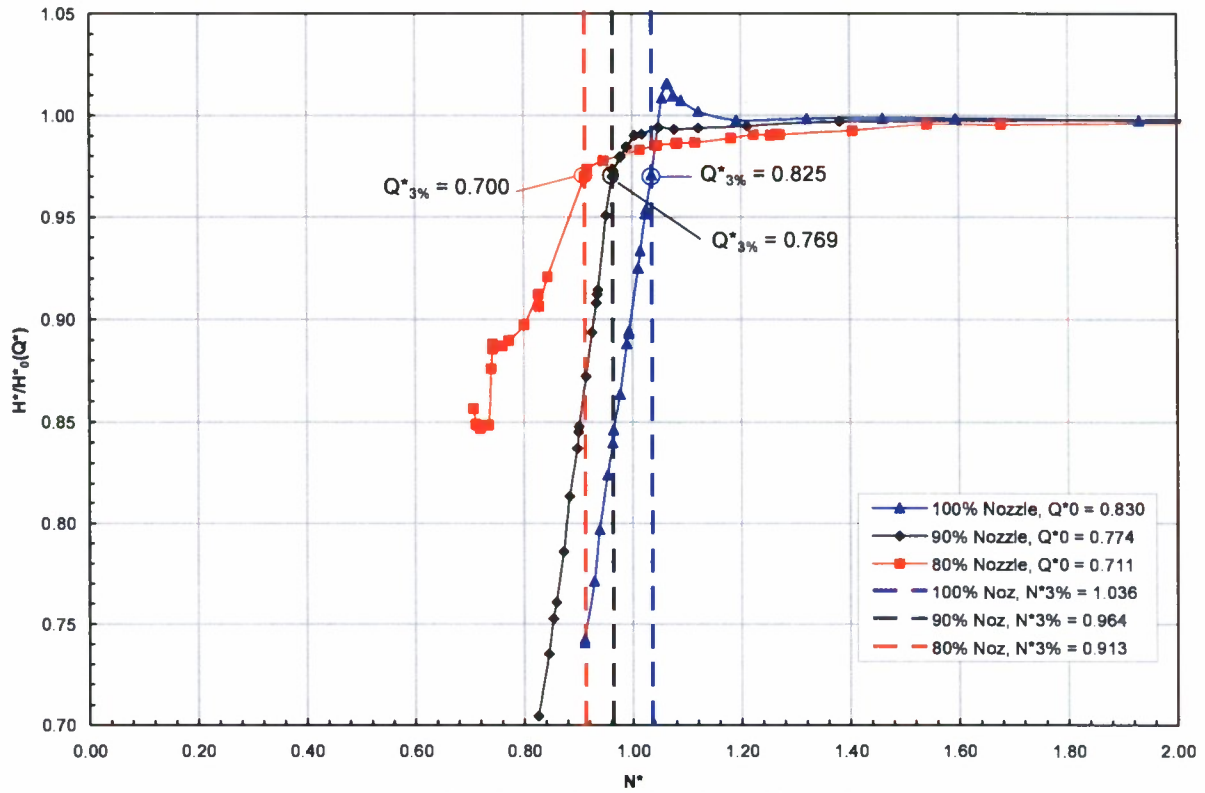
Fig. 43. Normalized non-dimensional total headrise vs. N^*.
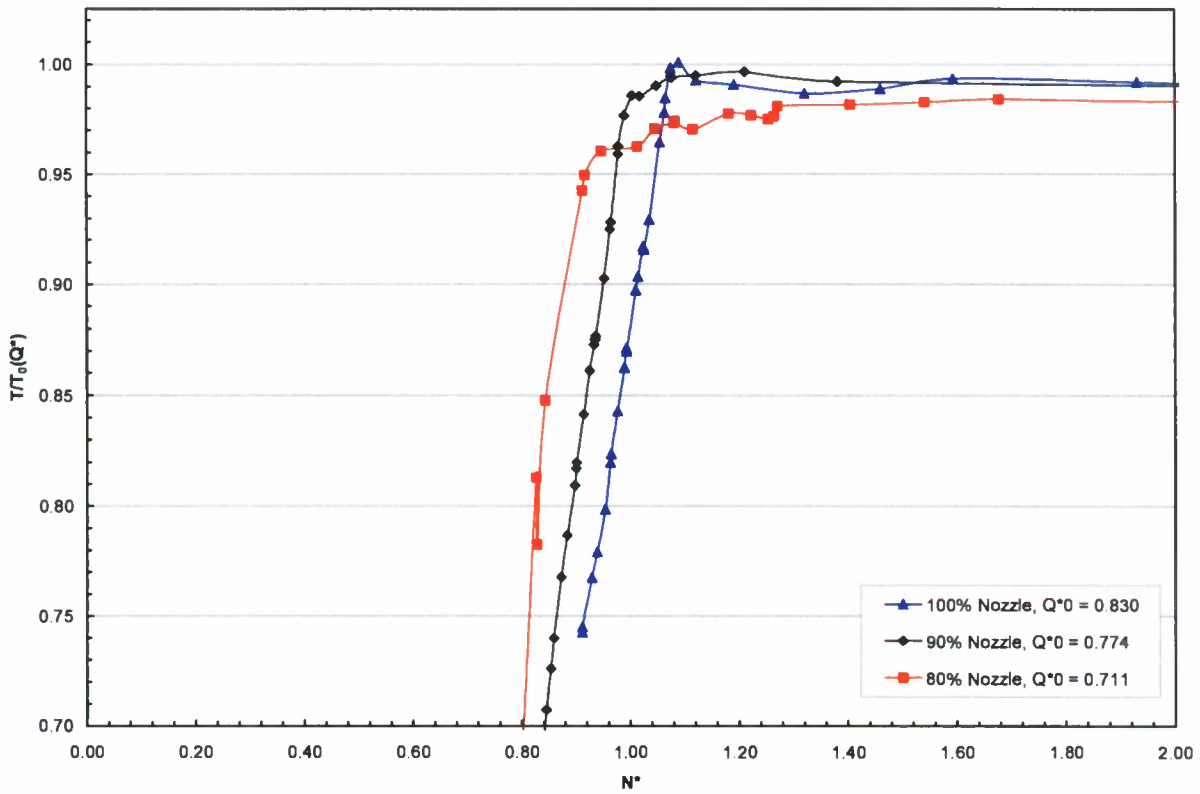
Fig. 44. Normalized impeller thrust vs. N^*.
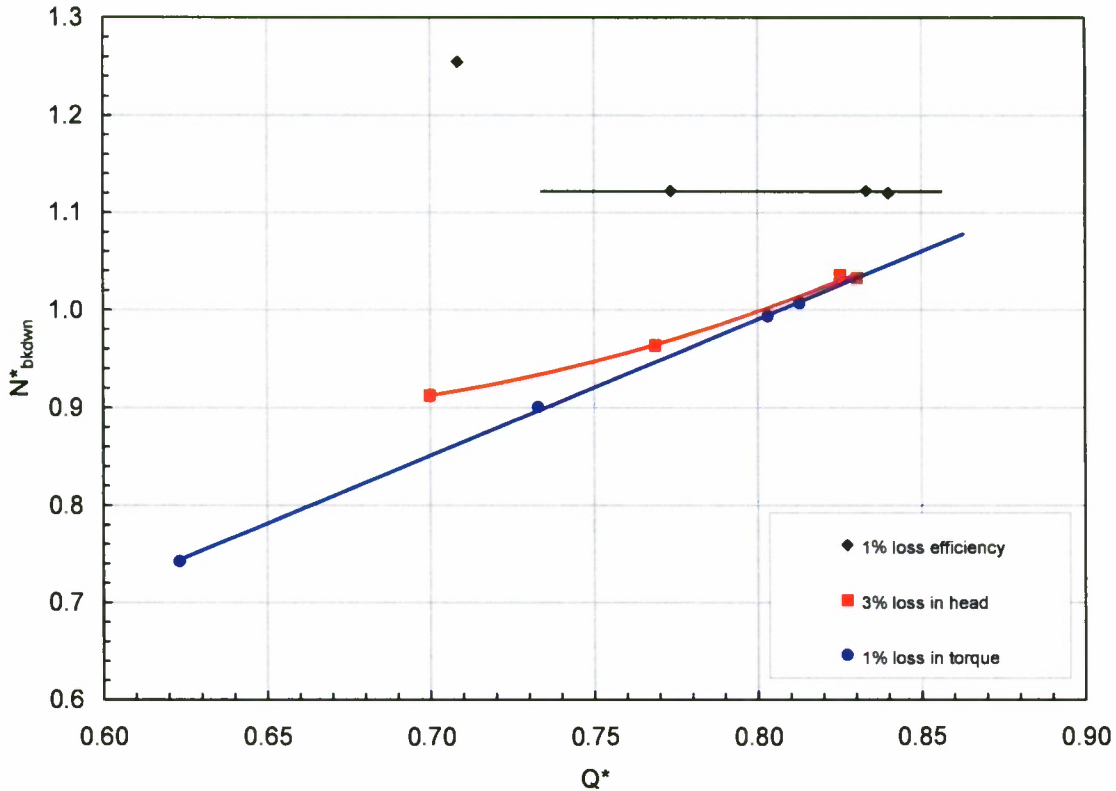
Fig. 45. Thrust breakdown results summary.

Data from the thrust breakdown runs is shown in Figs. 42, 43, and 44. These figures show only the region of N^* near breakdown to emphasize detail. These data show how the torque, headrise, and thrust change as the tunnel static pressure, represented non-dimensionally by N^*, is lowered at a constant waterjet rotor RPM. The breakdown points based on torque and headrise are shown on their respective plots, Figs. 42 and 43. The N^* as defined by the 1% loss in torque is denoted as $N^*_{1\%}$, while the N^* as defined by 3% loss in headrise is denoted as $N^*_{3\%}$. Fig. 42 shows that, when approaching breakdown, the torque increases and then drops off quickly. For the two highest flow rate conditions the torque increased about 7%. At the lowest flow rate condition, torque increased only 3% before breakdown. The headrise and thrust breakdown plots, Figs. 43, and 44, show no rise in values for the two lowest flowrate conditions, but for the highest flow rate condition, the values do increase slightly before dropping. The results of the thrust breakdown runs using all three definitions of breakdown stated above are shown in Fig. 45. When using 1% loss of efficiency as a thrust breakdown condition, a single N^* value is typically used for all flow rates (as is indicated in Fig. 45). At higher flow rates it can be seen that the different definitions of breakdown approach a similar value (though still are different by as much as 5% at design $Q^* = 0.85$) while at lower flow rates they deviate significantly.
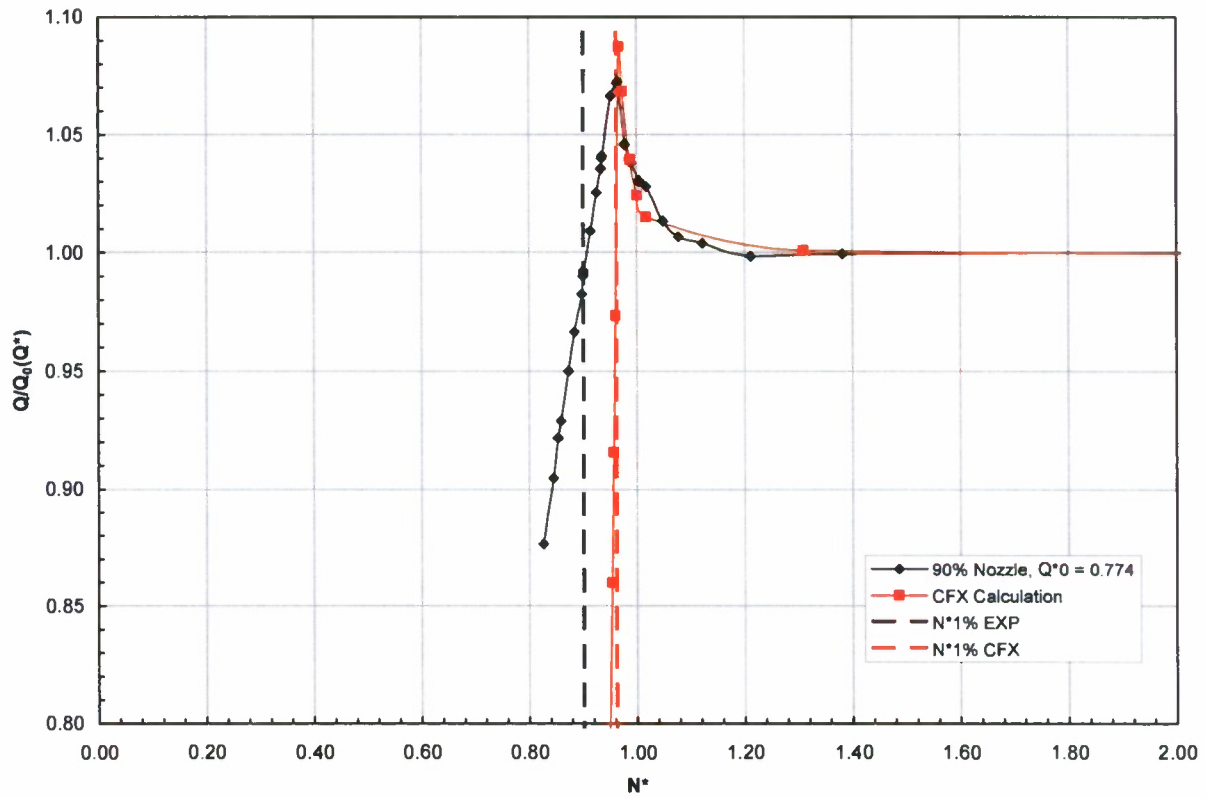
Fig. 46. Torque vs. N^*, CFX calculation and experiment, results, 90% nozzle.
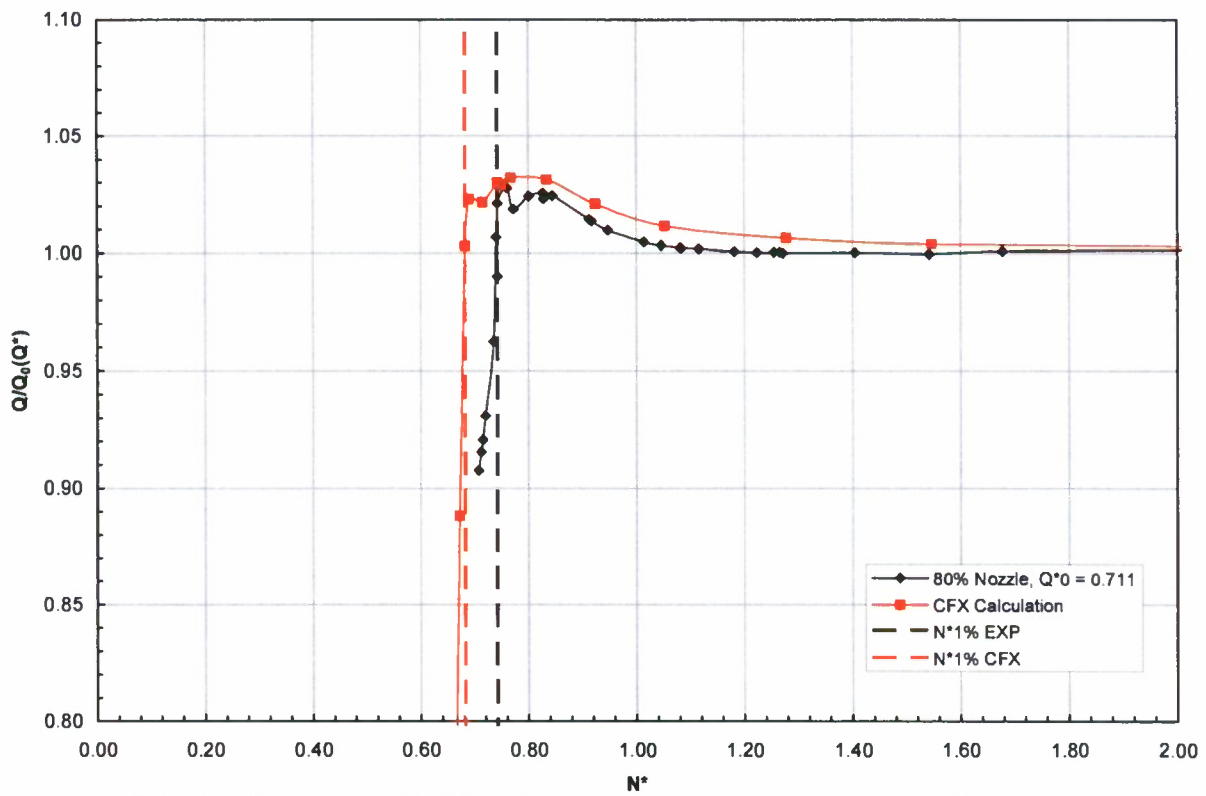
Fig. 47. Torque vs. N^*, CFX calculation and experiment, results, 80% nozzle.
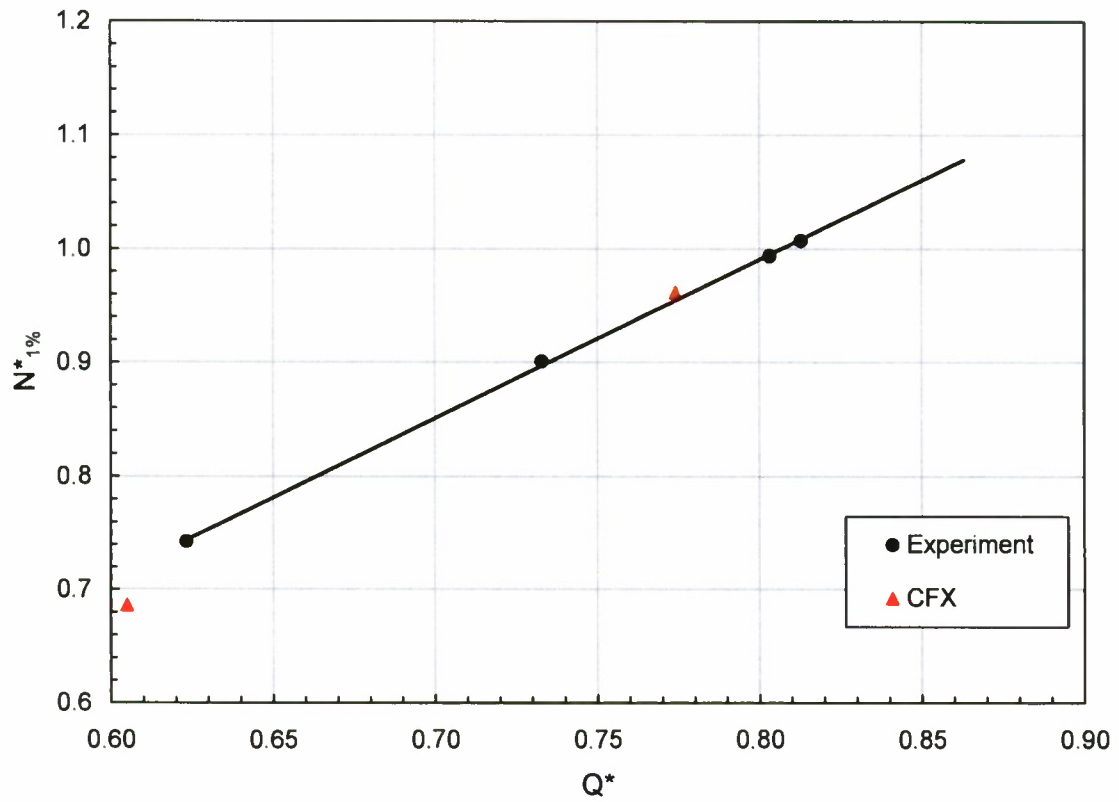
Fig. 48. Thrust breakdown results summary, CFX calculation and experiment.
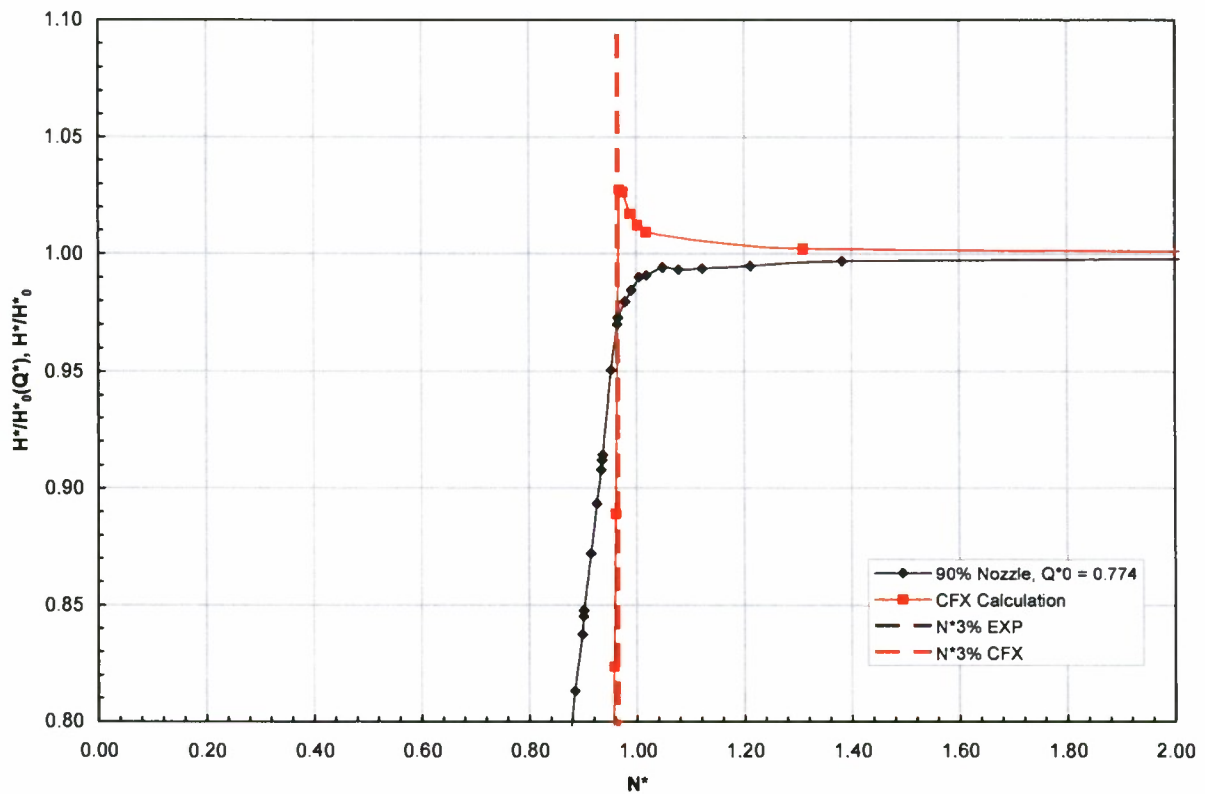
Fig. 49. H^* vs. N^*, CFX and experimental results, 90% nozzle.
CFX head is rotor only, experiment is rotor and stator.
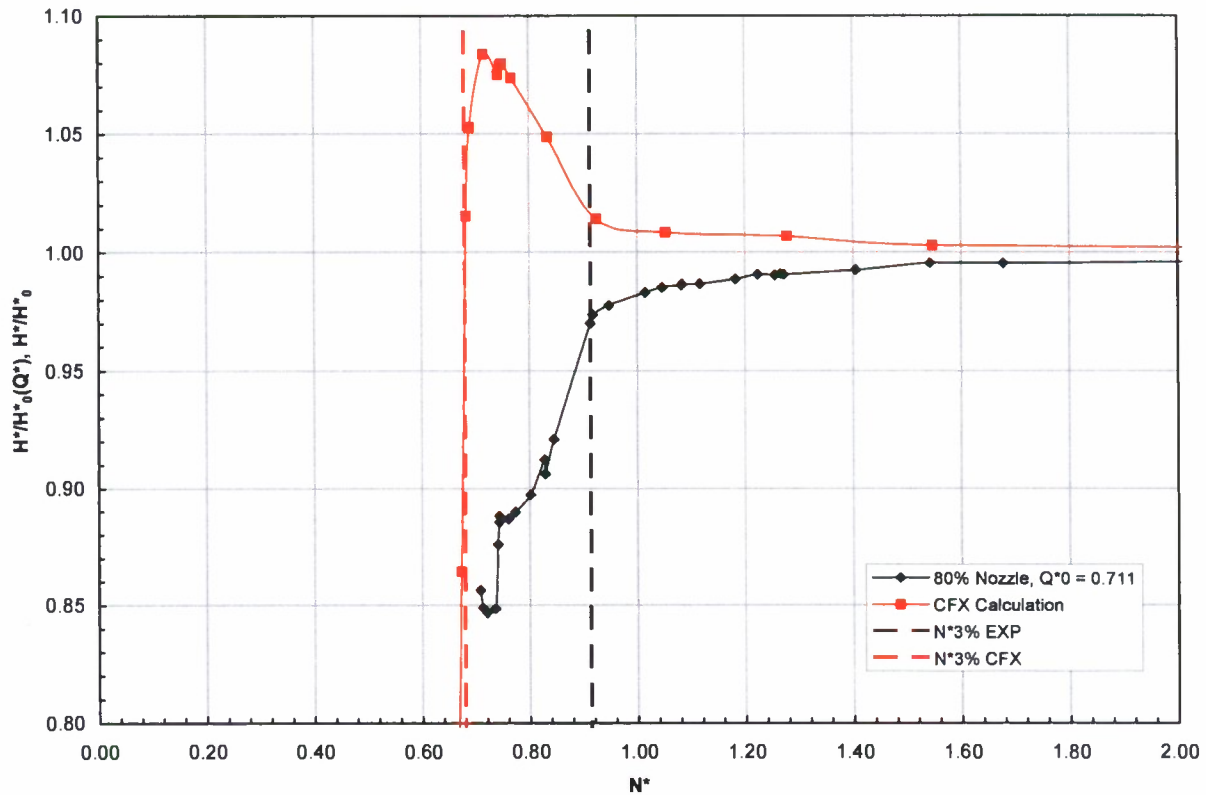
Fig. 50. H^* vs. N^*, CFX and experimental results, 80% nozzle.
CFX head is rotor only, experiment is rotor and stator.

Shown in Figs. 46 – 48 is the cavitation performance predicted using CFX plotted against the experimental results for two thrust breakdown runs (90% nozzle and 80% nozzle). The prediction uses the Rayleigh Plesset cavitation model in ANSYS CFX. Cavitation performance was computed using an impeller-only grid, unlike the performance calculations which utilized an impeller, stator configuration. In the calculation, N^* was first set to a value matching the measurements which was sufficient to suppress any cavitation in the waterjet. This calculation yields the same performance as the non-cavitating case. The N^* was then lowered in successive steps to determine the torque or headrise breakdown value as is done in the 36-inch water tunnel. In order to exactly match the measurements the flow rate was set to match the flow rate obtained at the corresponding experimental data point. As with the experimental data, the normalizing Q_0 values were calculated as a function of Q^* from the non-cavitating performance data. The H^* values from CFX are normalized somewhat differently. Since thrust breakdown runs from CFX were calculated with the rotor only, no map of rotor H^* vs. Q^* was available to normalize the thrust breakdown runs. The plotted CFX H^* data is therefore normalized by the initial non-cavitating H^*, and does not change with changes in Q^* . In Figs. 46 and 47, the CFX calculations match the experimental results for the peak torque ratio value within 2% while the $N^*_{1\%}$ value is 9% lower for the 80% nozzle condition and 7% higher for the 90% nozzle condition. In addition, the CFX torque ratio calculations drop off significantly faster (over 3 times) than the experimental results. Because of the different drop off rates and a shift in the breakdown curve between the CFX and the experimental runs, the $N^*_{1\%}$ values

occur not only at a different N^* values, but at different flow rates as well. If the $N^*_{1\%}$ values are plotted against the flow rate at breakdown as in Fig. 48, it can be seen that the CFX calculations predict breakdown better than is apparent in Fig. 46. The differences between CFX and experimental results for headrise shown in Figs. 49 and 50 are partially due to the difference between total headrise (experimental calculation) and impeller only headrise (CFX calculation). The impeller headrise in the CFX calculations increases prior to breakdown, while the total headrise experimental results show a gradual decrease before dropping off sharply. Also, as with the torque calculations, the CFX calculations drop off rate is much steeper than the experimental results.

The extent of blade surface cavitation causing thrust breakdown is shown in the photos of the impeller from the upstream shaft mounted camera. Fig. 51 shows predicted cavitation volume from CFX for the points plotted in Fig. 47 along with photos of the cavitation observed in the 36VPWT at similar conditions. The photos show that cavitation is forming at the leading edge of the impeller at $N^* = 4.044$, well before thrust breakdown is reached at $N^* = 0.742$. In the last photo of Fig. 51, $N^* = 0.827$ and the cavitation has covered a significant portion of the blade, but not until N^* reaches 0.742 does breakdown occur. The CFX calculations slightly under predict the blade surface cavitation coverage. In the water tunnel, cavitation starts a little earlier than predicted using CFX as can be seen in the first image of Fig. 51 where at $N^* = 4.044$ there is significant cavitation at the leading edge in the photo, while in the CFX model, there is no cavitation present.

Rotor Cavitation Coverage

The percentage of the blade covered by cavitation was found by analyzing shaft camera photos in Fig. 51. The photos show the cavitation region used in the calculation outlined in green and the total blade area outlined in red. The results of this analysis are plotted for 90% nozzle and 80% nozzle runs against equivalent calculations made from the CFX results in Figs. 52 and 53. Fig. 53 shows that for the 80% nozzle configuration 89.6% of the blade is covered as measured from shaft camera images, and 85.8 % of the blade is covered as calculated by CFX at the point of thrust breakdown as defined by 1% loss in torque. Photos of the cavitation from the side of the pump in Fig. 54 reveal the cavitation in the tip region. The interaction of the tip leakage cavitation with the suction side cavitation forms a wedge shaped cavitation pattern along the pump casing. The angle this wedge makes with an axial line was found to be relatively constant at about 74 degrees throughout thrust breakdown.
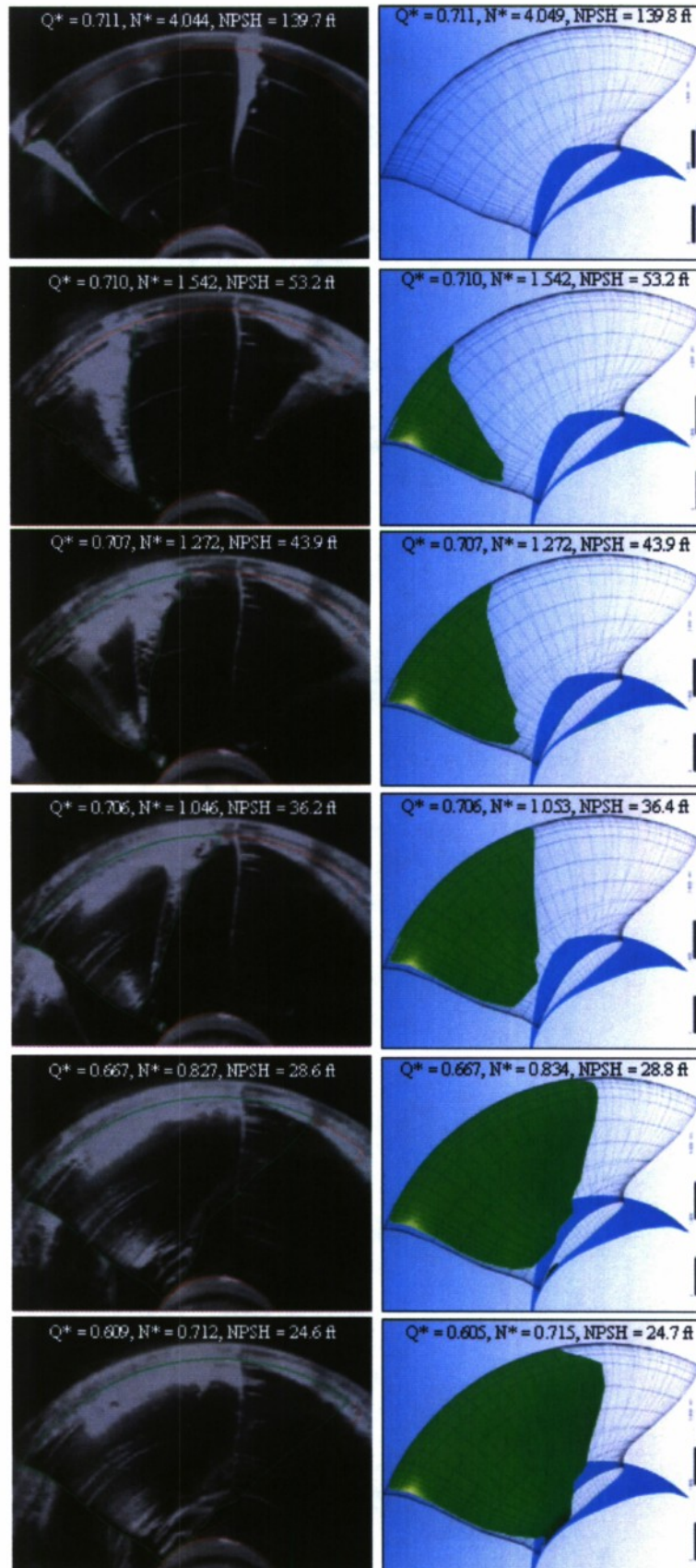
Fig. 51. Blade cavitation areas from shaft camera and CFX calculation.
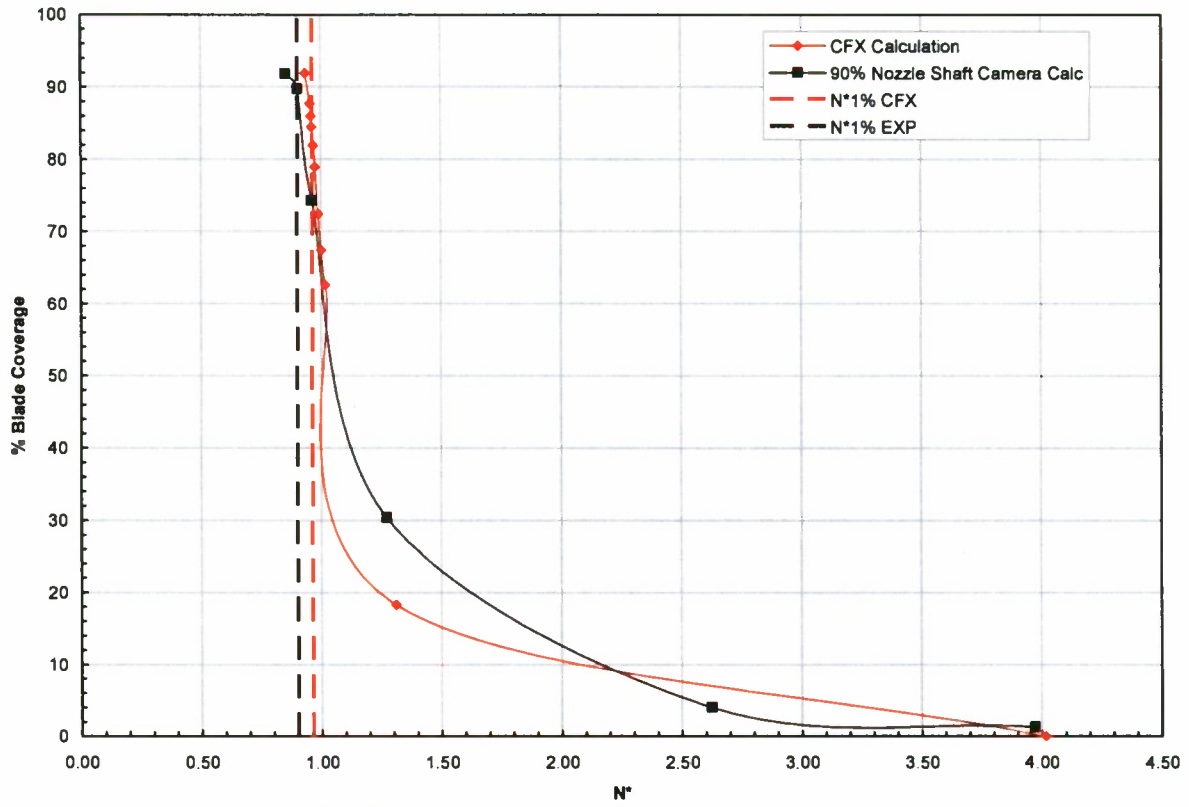
Fig. 52. Blade cavitation coverage, 90% nozzle.
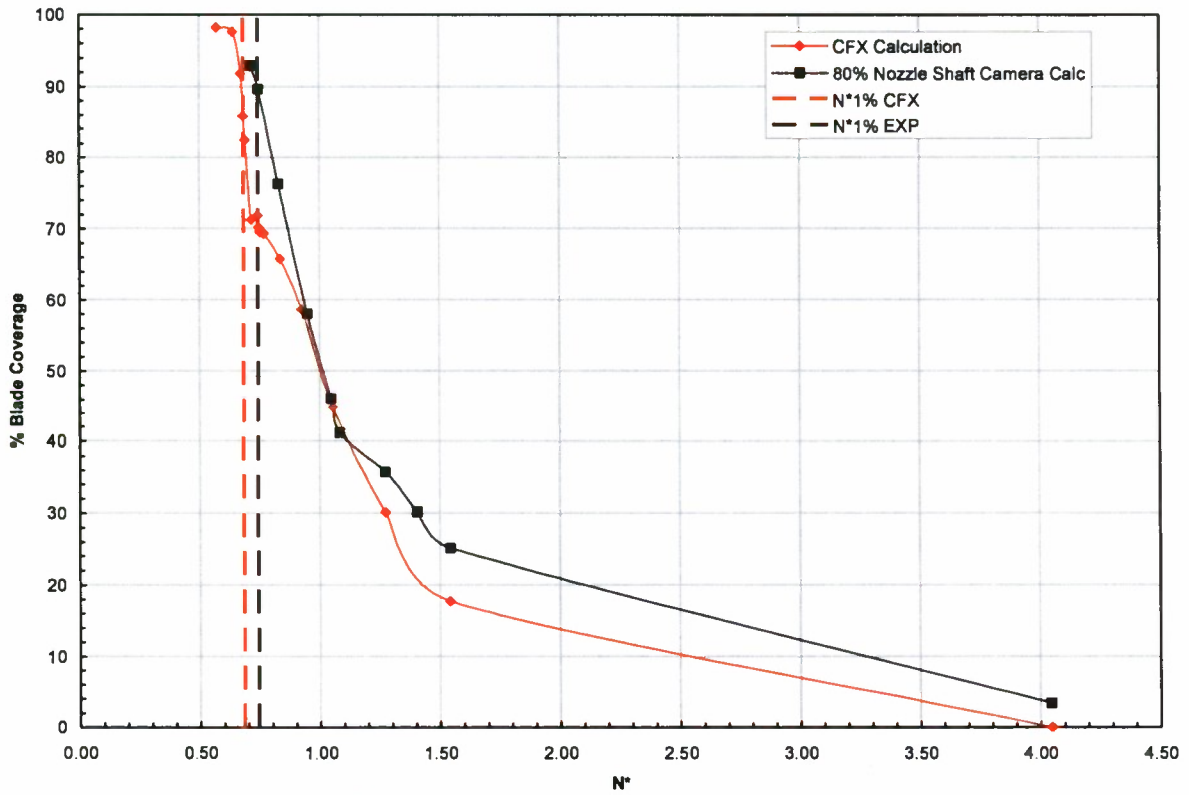
Fig. 53. Blade cavitation coverage, 80% nozzle.
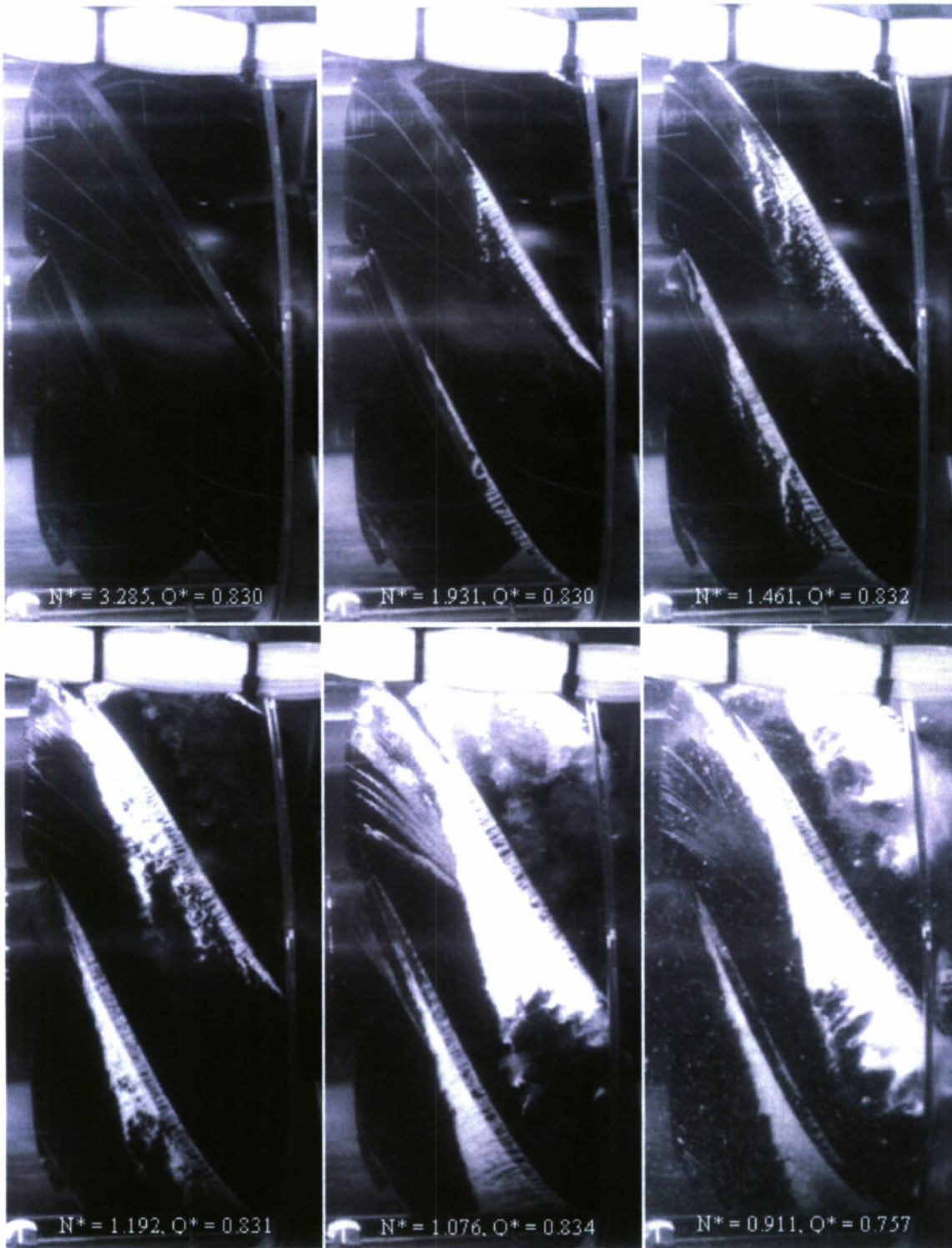
Fig. 54. Tip gap leakage cavitation, from side camera.

Cavitation Inception

Inception of suction side leading edge, tip gap leakage, and hub vortex cavitation were investigated in this test and the results are presented in Fig. 55. Breakdown points and design $Q*$ are also plotted in Fig. 55 to show the onset of all forms of cavitation well before breakdown.
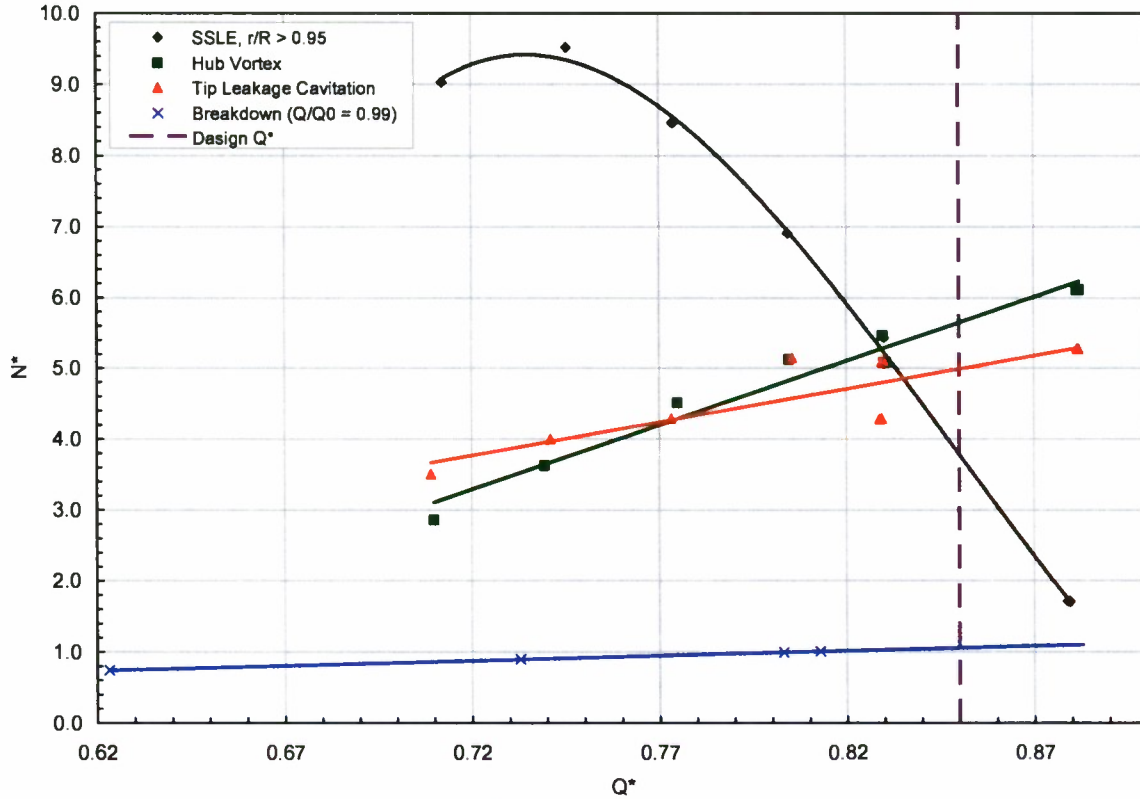
Fig. 55. Cavitation inception.

Cavitation Intensity and Erosion

Using pump casing acceleration (G_{rms}) measured on by the accelerometers mounted on the acrylic pump casing, cavitation intensity can be calculated using the following equations.

$$G_{rms}^{\bullet} = \frac{G_{rms}}{n^2 D} \tag{22}$$

$$I^{\bullet} = a \times \left(G_{rms}^{\bullet}\right)^b \tag{23}$$

$$I = I^{\bullet}\left(\frac{P_w}{D^2}\right) \tag{24}$$

Where P_w is shaft power and D is the pump inlet diameter. Coefficients a and b were derived by correlating cavitation intensity to pump casing vibration levels by the Turbomachinery Society of Japan[9]. The values used are $a = 2 \times 10^{-7}$ and $b = 1.58$. We are unsure how the intensity was measured to perform this correlation. Figs. 56 – 58 show the cavitation intensity calculated from two accelerometers during the 3 thrust breakdown runs

(100%, 90%, and 80% nozzles). The intensity of the cavitation at breakdown, defined by 1% loss in torque, increases with decreasing Q^* (i.e. it is lower at 100% nozzle breakdown condition than at 80% nozzle breakdown condition). During a single thrust breakdown run, the cavitation intensity increases gradually as N^* decreases, dips prior to thrust breakdown, and then increases sharply just before the thrust breakdown condition is reached.

The intensity calculations are on the same order of magnitude as the ASTM G32[10] acoustic cavitation erosion intensity measurements from material coupon tests performed by DynaFlow. G32 acoustic cavitation tests consist of using a vibrating horn to impinge acoustically generated cavitation on a material coupon. The coupon can then be analyzed for erosion volume and mass loss. Performing a G32 test on a material sample identical to the material used in the AxWJ-2 impeller would allow estimation of cavitation erosion incubation times and pitting depths after a given amount of time running at a condition where the intensities were similar to the G32 test.

The accelerometer signals were also analyzed for frequency content. Fig. 59 is a detail of the power spectral density surrounding the blade rate frequency of 200 Hz at three different N^* conditions in the 100% nozzle breakdown run. As N^* is decreased it is apparent that frequency content (i.e. the blade rate peak) becomes obscured by broadband noise. The $N^* = 0.991$ condition, where the blade rate peak is completely hidden by noise, is just past the condition defined by 1% loss in torque.

Stencil ink was used to indicate areas on the rotor blade which could potentially experience cavitation erosion. This test was run with the 100% nozzle with a 5% loss of torque from cavitation ($Q^* = 0.786$, $N^* = 0.964$) for 122 minutes. Fig. 60 shows before and after photos of the rotor with stencil ink, indicating that the most likely location for cavitation erosion at this condition is on the suction side of the rotor near the trailing edge tip.
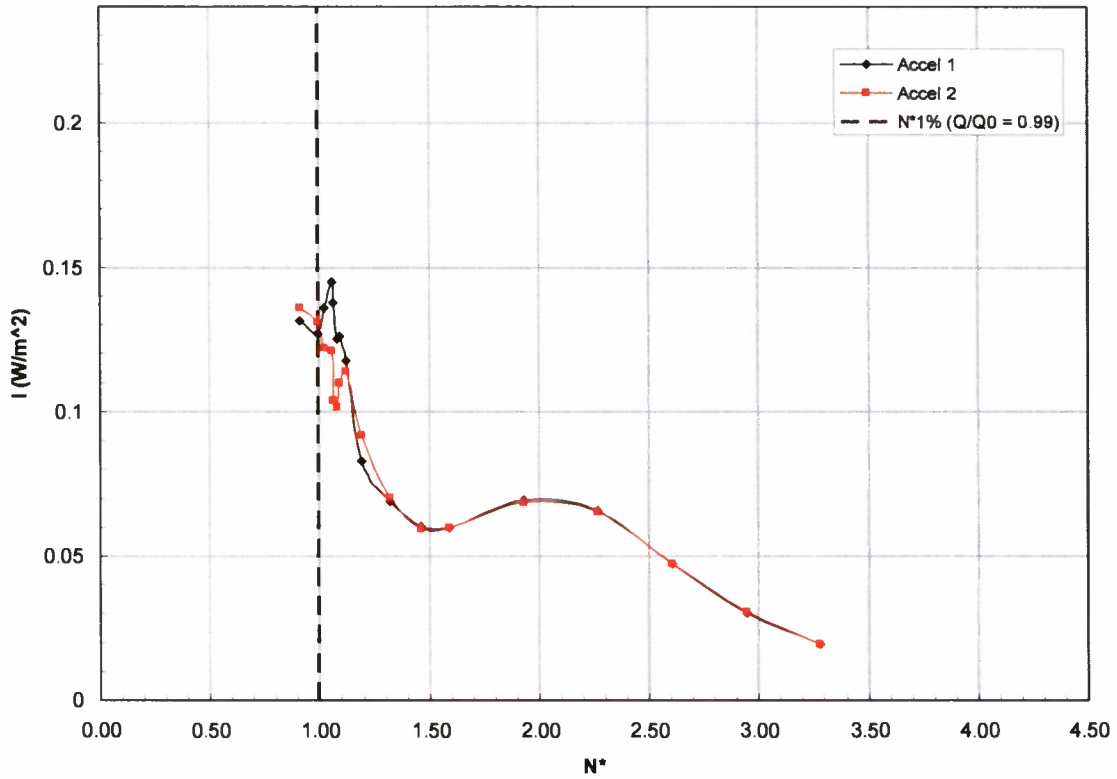
Fig. 56. Cavitation intensity during 100% nozzle breakdown run.
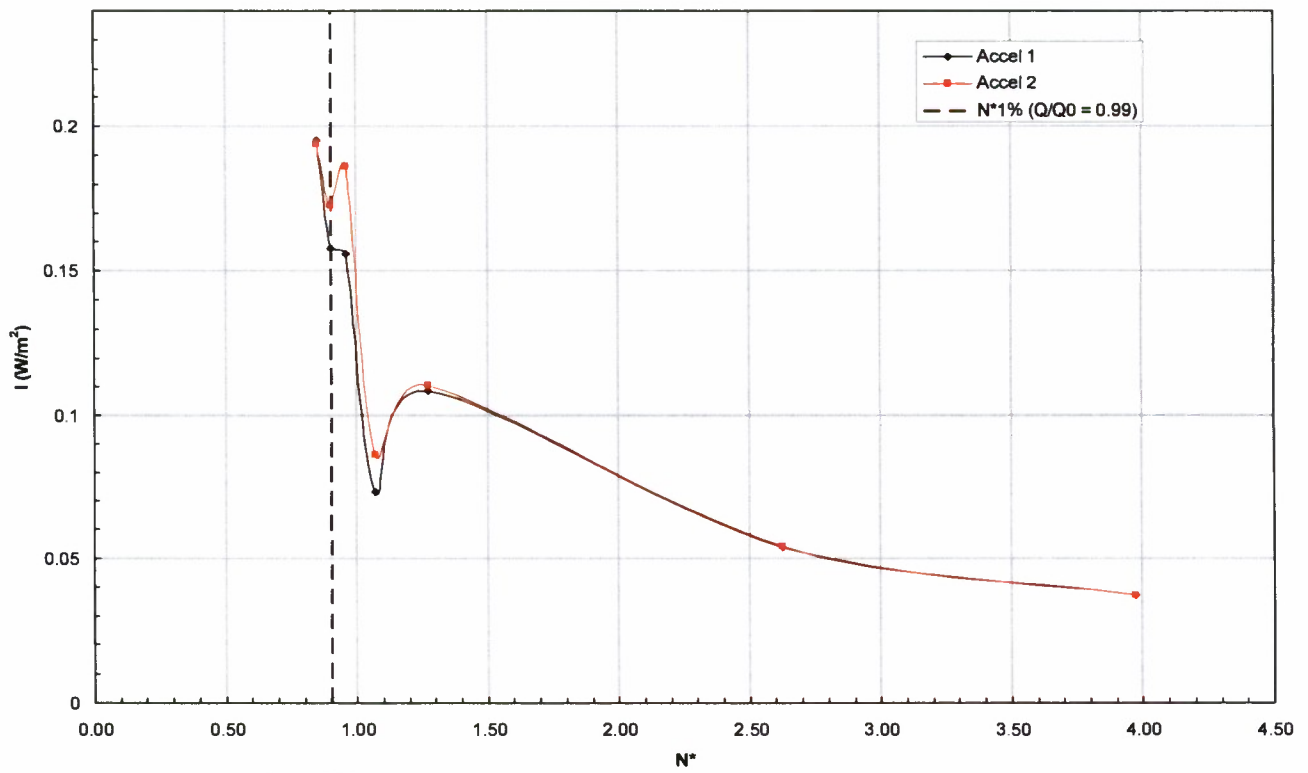
Fig. 57. Cavitation intensity during 90% nozzle breakdown run.
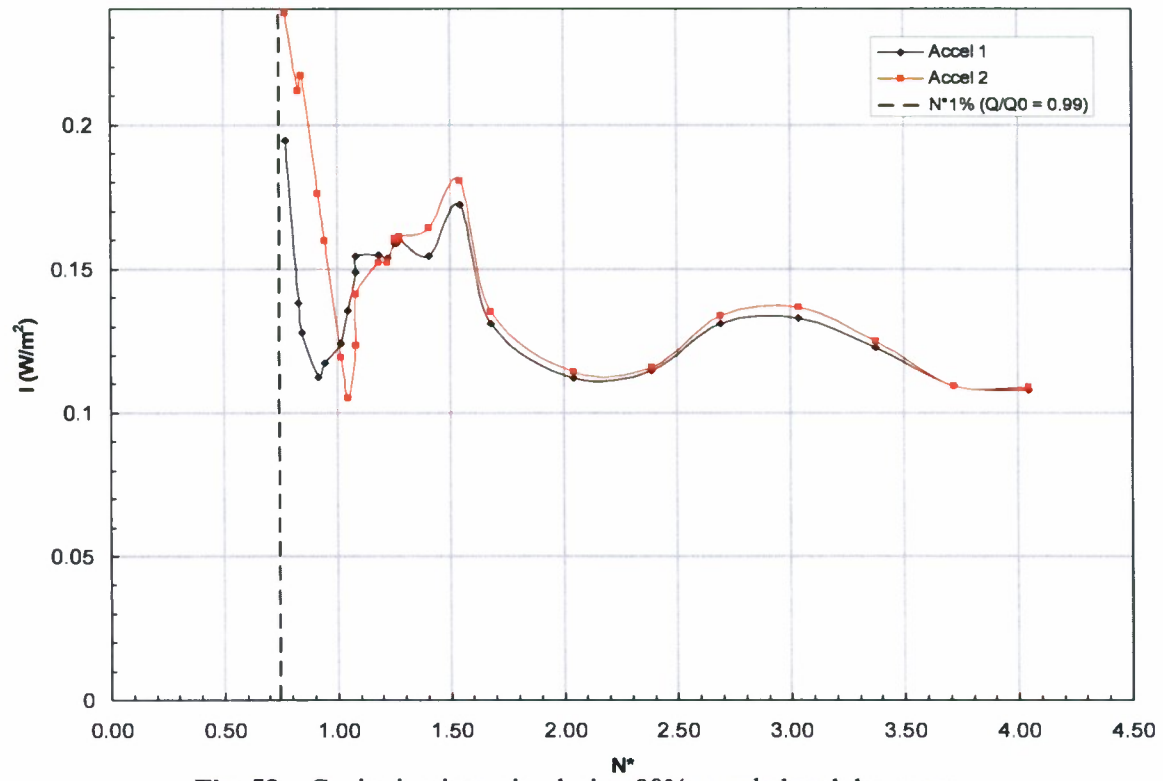
Fig. 58. Cavitation intensity during 80% nozzle breakdown run.
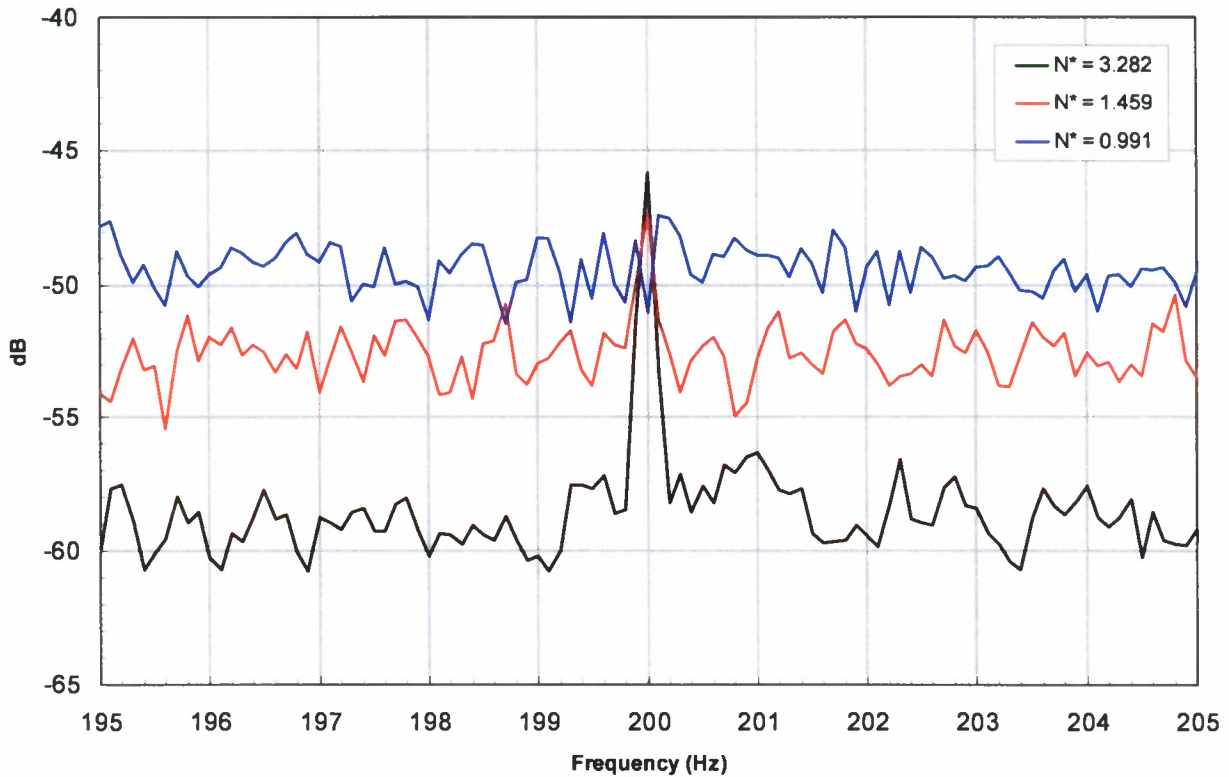
Fig. 59. Frequency content of 100% nozzle thrust breakdown configuration.
Blade rate of 200 Hz.
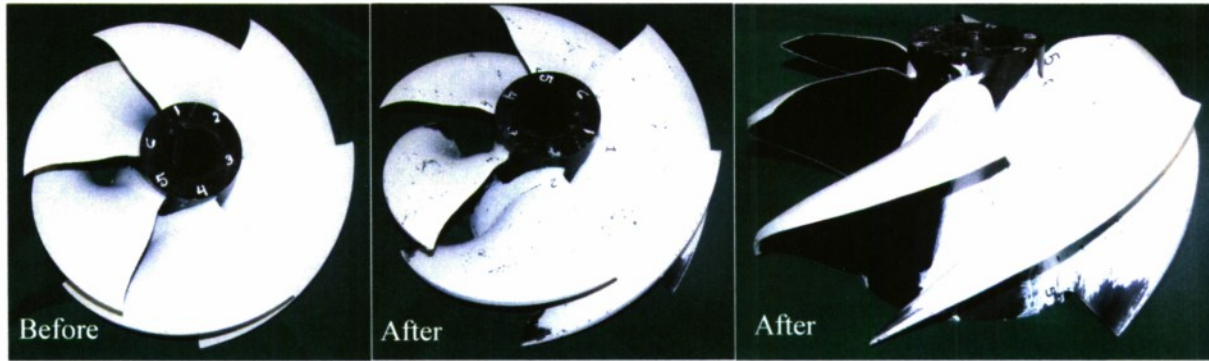
Fig. 60. Stencil ink erosion on impeller.

Full-Scale Powering Predictions

The performance specifications for the waterjets operating on JHSS were outlined in the original BAA documentation[1] and later modified with agreement from both vendors. These requirements are:

Power: The waterjet shall be designed for a maximum continuous shaft power of 36 MW. Maximum ship speed shall be determined by using the total ship resistance shown in Table 7, and maximum sustained speed shall be defined as the speed achieved in calm water at 85% maximum continuous power. Total effective power (*PE*) in calm water as a function of ship speed is provided in Table 7 for a notional JHSS ship. The required thrust should be determined with the assumption that the ship will be propelled by four waterjets, each providing ¼ of the total thrust.

Pump size: The internal pump diameter shall not exceed 10 feet. A maximum internal diameter as small as 9 feet will be considered favorably when assessing overall performance.

Cavitation performance: The pump shall operate within Zone 1 up to the required operating speed of 36 knots. The Zone 1 boundary is defined by *NPSH(A)* = 1.2 x *NPSH*(1%). Values of *NPSH*(1%) are defined as the *NPSH* at the pump inlet face, or ITTC Station 3, for a 1% drop in measured impeller torque relative to the non-cavitating torque.

Efficiency: Propulsive efficiency shall be made as high as possible while meeting other requirements. Propulsive efficiency (*PC*) is defined as the *EHP* / *DHP* or effective horsepower divided by delivered horsepower. *PC* can also be defined as the multiplication of component efficiencies,

$$PC = \eta_P \times \eta_J \times \eta_R \times \eta_H \tag{25}$$

Where,

η_P is the model-scale pump efficiency, $Q^* \cdot H^* / P^*$

η_J is the jet efficiency

$$\eta_J = \frac{2\mu\ (1-\mu)}{1-\mu^2(1-\xi_{13})} \qquad \mu = \frac{V_1}{V_6} \tag{26}$$

η_R is the relative rotational efficiency as defined by the ratio of pump efficiency measured in a system test to the pump efficiency measured in a pump-loop facility. This factor was later set to 1 as the difference in pump efficiency between the two facilities is characterized by non-uniformity factors determined from measurements of the inflow velocity to the impeller.

η_H is hull efficiency or $\dfrac{(1-t)}{(1-w)}$

In order to simplify the performance assessment, the following factors were specified:

$1-t = 1.045$ (thrust deduction factor = unpropelled hull resistance / waterjet system thrust)

$1-w = 0.90$ (wake fraction at ITTC Station 1a)

$\zeta_{13} = 0.13$ (inlet loss coefficient, non-dimension energy lost from ITTC Station 1 to 3)

Additional assumptions used to simplify the analysis of waterjet performance on JHSS included: no Reynolds number scaling is applied to model-scale efficiency, and no shaft losses are applied to the 36 MW delivered shaft power.

Table 7. Estimated Effective Power for a notional JHSS.

Ship Speed (knots)	Effective Power PE (kW)	Effective Power PE (hP)
10	1772	2376
12	3024	4055
14	4752	6373
16	7043	9445
18	10015	13430
20	13752	18442
22	18223	24437
24	23334	31291
26	29354	39364
28	36269	48638
30	43477	58304
32	50136	67233
34	57849	77577
35	63601	85290
36	70966	95167
37	79895	107141
38	90389	121214
39	102955	138065
40	118357	158719

Notes: 1.) PE = Total Resistance × Ship Speed
2.) The PE includes the estimated appendage drag, air drag, 8% margin, and the correlation allowance (C_A) of 0.0002.

Vendor Powering Prediction Method

Using polynomial curve fits to the data generated in the uniform inflow pump-loop facility the full-scale performance of the ONR AxWJ-2 on the JHSS is evaluated. The pump-loop data used incorporates both the

inflow and nozzle exit non-uniformity factors in the computation of the non-dimensional head rise, H^*. These predictions are made utilizing an Excel spreadsheet to execute an approach provided by one of the vendor's under the ONR BAA. This approach involves determining the system thrust of the waterjet for a constant input power over a range of flow coefficients, Q^*. System thrust is defined as the net change in momentum from ITTC Station 1A to ITTC Station 7. The equations used in this analysis are shown in Table 8. The point at which the constant power curve intersects the resistance curve for the vessel, as defined in Table 7, defines the speed of the vessel and waterjet rpm for the selected input power. The results of this analysis are shown in Table 10 for a constant input power of 36 MW over a flow coefficient range from $Q^* = 0.735$ to 0.82.

In addition to defining the operating point these results are used to define the Zone 2 cavitation boundary or a line along which $NPSH(A) = NPSH(1\%)$. In the literature this is sometimes referred to as $NPSH$ required, or $NPSH(R)$. The value of $NPSH(1\%)$ is derived from the cavitation constant N^* at which the impeller has experienced a 1% drop in torque from its non-cavitating value. These values are determined from pump-loop tests as discussed earlier in this report. The results of this procedure are shown graphically in Fig. 61. This procedure is repeated for each line of constant power. The Zone 1 and Zone 3 cavitation boundaries are defined similarly with Zone 1 defined as $NPSH(A) = 1.2 \times NPSH(1\%)$, and Zone 3 as $NPSH(A) = 0.8 \times NPSH(1\%)$.

Final results for ten input powers from 9 MW to 36 MW are shown in Table 9. These results are presented graphically as a waterjet performance map in Fig. 62. The inlet diameter is specified as 9 ft. (2.743 m) with a nozzle to inlet diameter ratio of 0.63. The predicted sustainable ship speed at 85% maximum continuous rating (MCR) or 30,600 kW is 37.8 knots meeting the stated 36 knot requirement in the ONR BAA. The ship resistance curve falls completely within Zone 1, or below the Zone 1 boundary, with a cavitation margin of 5.4 knots. The cavitation margin is defined as the speed difference between the full power, 36,000 kW, intersection with the ship resistance curve, 39.0 knots, and the full power intersection with the Zone 1 boundary, 33.6 knots.

The propulsive coefficient, PC, is defined as the effective horsepower, EHP, divided by the delivered or shaft horsepower, DHP. The DHP is a chosen input to the procedure described above and is based on the installed power available on the vessel. EHP is defined as the ship speed x waterjet system thrust. The computation of PC for the JHSS hull form with four ONR AxWJ-2 waterjets is included in Table 10. This computation is in agreement with the component efficiencies detailed in Equation 25 and shown in Table 11.

As was stated in the original ONR BAA documentation, a reduction in inlet diameter would be considered favorably in the evaluation process for a Phase II award. Additional analysis indicates a reduction in inlet diameter to 7.4 ft. (2.256 m) would be possible and still meet the requirement stated in the ONR BAA. With this reduced size pump the ship would have a speed of 37.3 knots at 85% MCR and would still meet the requirement to operate completely within Zone 1 up to 36 knots. The maximum ship speed obtainable at 36 MW would be 38.5 knots. This point would be within the Zone 2 area of operation. The results of this analysis are shown in Table 12 and Fig. 63. This decrease in inlet diameter would result in a 12-13% increase in the JVR

reducing PC by 7-8% across the speed range. The comparison of propulsive coefficient for JHSS at the initial and reduced inlet diameters is shown in Fig. 64. The component efficiency breakdown is shown in Table 13 showing that the only component impacted is η_J. It should be noted that a change in Reynolds number due to the reduction in size of the pump is not accounted for in the pump efficiency, η_P. There is a potential that this reduction in PC due to increased JVR could be offset by a reduced hull resistance made possible by a reduction in the transom width due to a reduced waterjet inlet diameter.

Table 8. Equations utilized in powering predictions.

Value	Definition	Source
Head coefficient H*	function of Q*	CFD or pump-loop test
Power coefficient P*	function of Q*	CFD or pump-loop test
N*$_{1\%}$	cavitation number at 1% loss in torque, determined as a function of Q*	Pump-loop test
Pump efficiency	= Q* H* / P*	
RPM (rev/min)	$(\dfrac{P_D(kW)*1000}{P*\rho D^5})^{\frac{1}{3}}*60$	
Flow rate (m³/s)	$Q*\ RPS\ D^3$	
RPS (rev/sec)	RPM / 60	
Head (m)	$H*RPS^2\ D^2/g$	
Jet velocity (m/s), V_j	Flowrate / nozzle area (A_6)	
Nozzle dynamic head (m)	$V_6^2/2g$	
Head recovery (m)	nozzle dynamic head – head	
Inlet loss coefficient	input parameter, function of inlet velocity ratio, IVR	System test or full-scale installation
Intake velocity (m/s)	$\sqrt{\dfrac{2g\ head\ recovery(m)}{(1-inlet\ loss\ coeff)}}$	
Wake fraction, (1-w)		CFD or tow-tank test
Ship speed (knots)	intake velocity / (1-w)	
NPSH(A) (m)	9.85 + head recovery	9.85 meters = Patm – Pv seawater
NPSH(1%) (m)	N* RPS² D² / g	
Thrust deduction fraction, t	Input parameter, function of ship speed	Full-scale or tow-tank test
Jet system thrust (kN)	$\rho Q_J (V_6 - V_{1avg})$	
Propulsive efficiency (%)	function of Q*	CFD or pump-loop test

Table 9. Range of system thrust for 36MW input power.

	D = 9 ft					
D6/D3 = 0.63				Power = 36 MW		
Flow coefficient Q*	0.735	0.752	0.769	0.786	0.803	0.82
Head coefficient H*	2.5603	2.5071	2.4525	2.3965	2.3388	2.2795
Power coefficient P*	2.1174	2.1197	2.1201	2.1187	2.1154	2.1102
Cavitation constant N*	0.8942	0.9180	0.9417	0.9655	0.9892	1.0130
Pump efficiency	0.889	0.889	0.890	0.889	0.888	0.886
RPM (rev/min)	284.7	284.5	284.5	284.6	284.7	285.0
Flow rate (m³/s)	71.98	73.62	75.28	76.96	78.67	80.40
Head (m)	44.22	43.27	42.32	41.38	40.42	39.46
Jet velocity (m/s)	30.69	31.38	32.09	32.81	33.54	34.27
Nozzle dynamic head (m)	48.01	50.22	52.51	54.88	57.34	59.90
Head recovery (m)	3.79	6.95	10.19	13.51	16.92	20.43
Inlet loss coefficient	0.130	0.130	0.130	0.130	0.130	0.130
Intake velocity (m/s)	9.24	12.52	15.15	17.45	19.53	21.46
Wake fraction, (1-w)	0.850	0.850	0.850	0.850	0.850	0.850
Ship speed (knots)	21.1	28.6	34.7	39.9	44.7	49.1
NPSH(A) (m)	13.64	16.80	20.04	23.36	26.77	30.28
NPSH(1%) (m)	15.45	15.84	16.25	16.67	17.10	17.54
Thrust deduction fraction, t	-0.045	-0.045	-0.045	-0.045	-0.045	-0.045
Thrust (kN)	1653.3	1487.7	1365.7	1266.0	1180.1	1103.2
Propulsive efficiency (%)	49.94	60.86	67.63	72.20	75.32	77.38
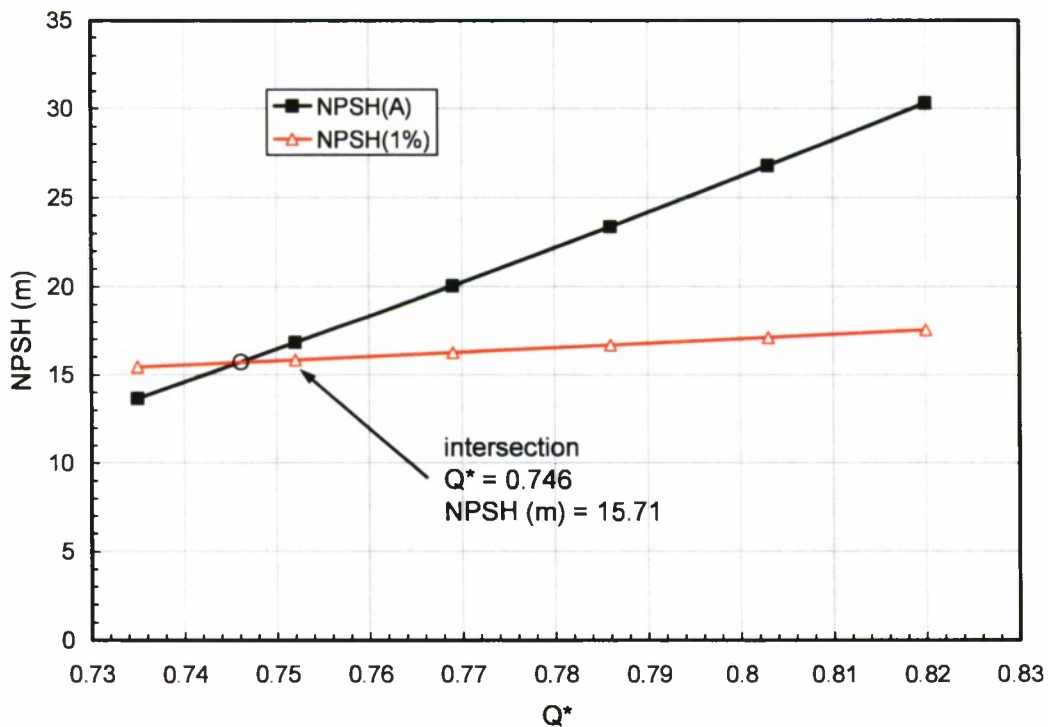
Fig. 61. Definition of Zone 2 boundary for 36 MW input power.

Table 10. Powering performance for JHSS with 9 ft (2.743 m) inlet diameter pumps.

					$D_6/D_3 = 0.63$					
Power at jet, P_D (kW)	9000	12000	15000	18000	21000	24000	27000	30600	33000	36000
Percent MCR	25%	33%	42%	50%	58%	67%	75%	85%	92%	100%
4 x Power (DHP)	48276	64368	80460	96552	112644	128736	144828	164138	177012	193104
Flow coefficient Q*	0.785	0.785	0.787	0.791	0.792	0.790	0.788	0.786	0.785	0.783
Head coefficient H*	2.4010	2.3988	2.3937	2.3807	2.3778	2.3827	2.3889	2.3962	2.4009	2.4067
Power coefficient P*	2.1189	2.1188	2.1186	2.1180	2.1178	2.1181	2.1184	2.1187	2.1189	2.1191
Cavitation constant N*	0.9636	0.9645	0.9666	0.9720	0.9732	0.9712	0.9686	0.9656	0.9636	0.9612
Efficiency	0.889	0.889	0.889	0.889	0.889	0.889	0.889	0.889	0.889	0.889
RPM (rev/min)	179.3	197.3	212.6	225.9	237.8	248.6	258.6	269.6	276.5	284.6
Flow rate (m³/s)	48.40	53.31	57.54	61.46	64.77	67.59	70.13	72.91	74.63	76.66
Head (m)	16.45	19.91	23.06	25.90	28.67	31.40	34.05	37.12	39.11	41.55
Jet velocity (m/s)	20.63	22.73	24.53	26.20	27.61	28.81	29.90	31.08	31.82	32.68
Nozzle dynamic head (m)	21.70	26.34	30.68	35.00	38.87	42.33	45.57	49.26	51.61	54.45
JVR = Vjet / Vship	1.611	1.605	1.590	1.555	1.547	1.560	1.577	1.597	1.611	1.629
Head recovery (m)	5.25	6.43	7.63	9.10	10.20	10.93	11.52	12.13	12.50	12.90
Inlet loss coefficient	0.130	0.130	0.130	0.130	0.130	0.130	0.130	0.130	0.130	0.130
Intake velocity (m/s)	10.88	12.04	13.11	14.32	15.17	15.70	16.11	16.54	16.78	17.05
Wake fraction, (1-w)	0.850	0.850	0.850	0.850	0.850	0.850	0.850	0.850	0.850	0.850
Ship speed (knots)	24.9	27.5	30.0	32.8	34.7	35.9	36.9	37.8	38.4	39.0
NPSH(A) (m)	15.10	16.28	17.48	18.95	20.05	20.78	21.37	21.98	22.35	22.75
NPSH(1%) (m)	6.60	8.01	9.31	10.57	11.73	12.80	13.81	14.96	15.70	16.59
Thrust deduction, t	-0.045	-0.045	-0.045	-0.045	-0.045	-0.045	-0.045	-0.045	-0.045	-0.045
Thrust (kN)	505.4	610.4	703.8	781.8	863.4	949.6	1035.1	1135.7	1201.5	1282.8
Propulsive efficiency	0.719	0.720	0.724	0.732	0.734	0.731	0.727	0.722	0.719	0.715

Table 11. Breakdown of component efficiencies for D = 9 ft.

Power at jet, PD (kW)	9000	12000	15000	18000	21000	24000	27000	30600	33000	36000
% MCR	25%	33%	42%	50%	58%	67%	75%	85%	92%	100%
η_p	0.889	0.889	0.889	0.889	0.889	0.889	0.889	0.889	0.889	0.889
V_6/V_1	1.896	1.888	1.871	1.829	1.821	1.836	1.855	1.879	1.895	1.916
μ	0.527	0.530	0.535	0.547	0.549	0.545	0.539	0.532	0.528	0.522
η_j	0.658	0.659	0.662	0.670	0.671	0.669	0.665	0.661	0.658	0.654
η_d	1.229	1.229	1.229	1.229	1.229	1.229	1.229	1.229	1.229	1.229
η_r	1.000	1.000	1.000	1.000	1.000	1.000	1.000	1.000	1.000	1.000
PC	0.719	0.720	0.724	0.732	0.734	0.731	0.727	0.722	0.719	0.715

Fig. 62. Powering performance for JHSS with 9 ft (2.743 m) inlet diameter pumps. Single pump. Nozzle diameter = 0.63 D_i.
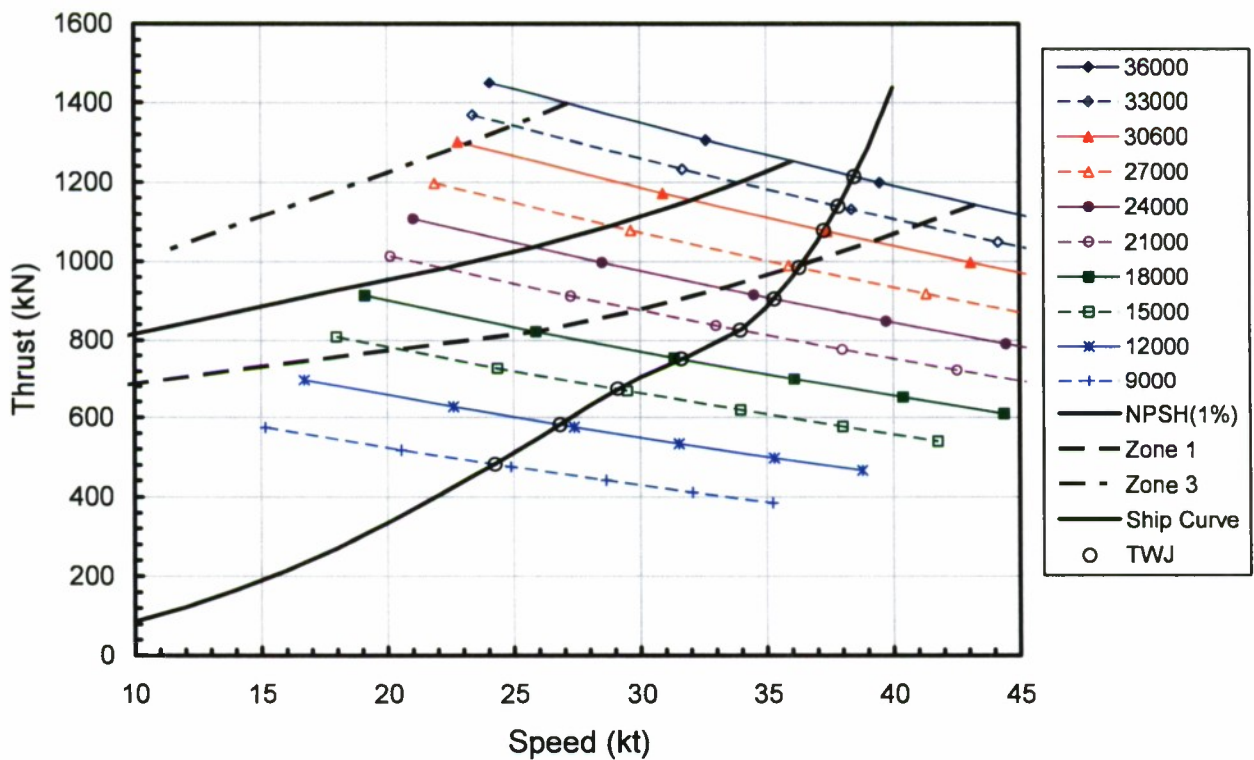
Fig. 63. Powering performance for JHSS with 7.4 ft (2.256 m) inlet diameter pumps. Single pump. Nozzle diameter = 0.63 D_i.
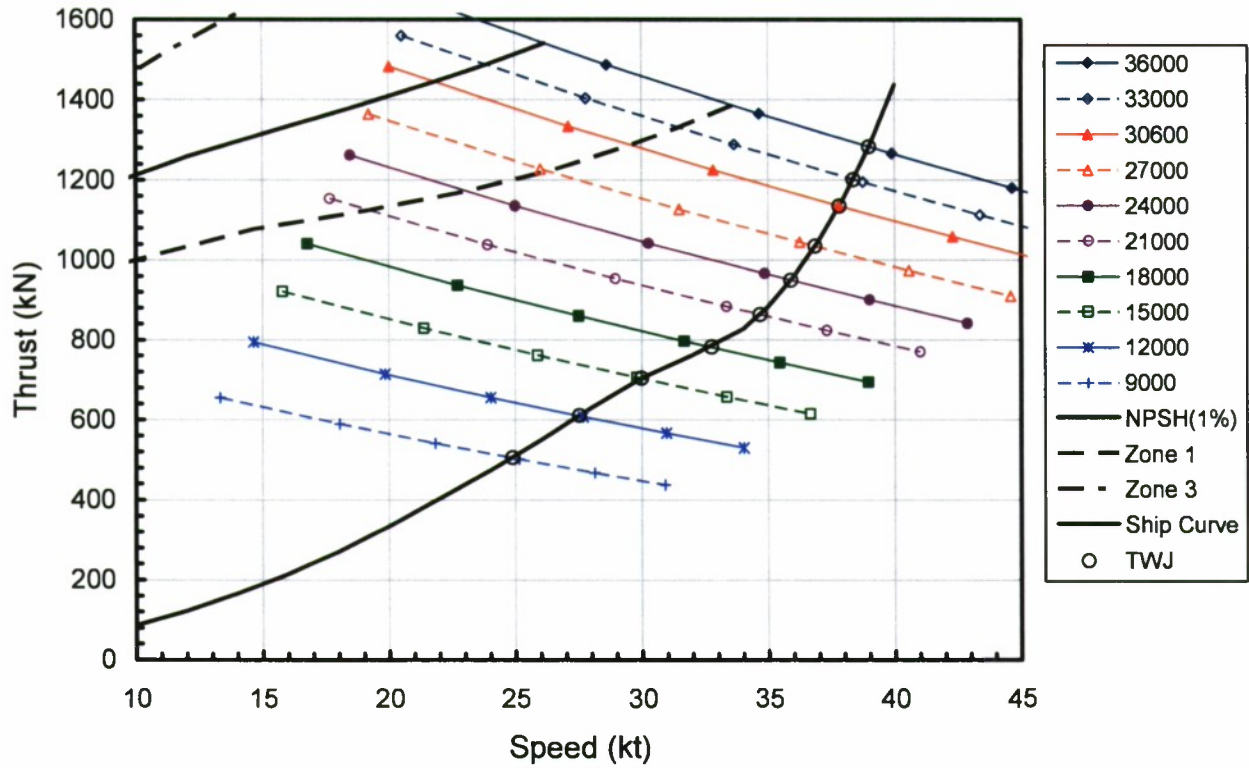
Table 12. Powering performance for JHSS with 7.4 ft (2.256 m) inlet diameter pumps.

$D_6/D_3 = 0.63$										
Power at jet, P_D (kW)	9000	12000	15000	18000	21000	24000	27000	30600	33000	36000
Percent MCR	25%	33%	42%	50%	58%	67%	75%	85%	92%	100%
4 x Power (DHP)	48276	64368	80460	96552	112644	128736	144828	164138	177012	193104
Flow coefficient Q*	0.766	0.767	0.768	0.770	0.772	0.772	0.770	0.769	0.768	0.766
Head coefficient H*	2.4611	2.4594	2.4569	2.4493	2.4423	2.4443	2.4484	2.4537	2.4571	2.4612
Power coefficient P*	2.1202	2.1202	2.1202	2.1201	2.1200	2.1200	2.1201	2.1201	2.1202	2.1202
Cavitation constant N*	0.9380	0.9388	0.9398	0.9431	0.9461	0.9452	0.9435	0.9412	0.9397	0.9380
Efficiency	0.890	0.890	0.890	0.890	0.890	0.890	0.890	0.890	0.890	0.890
RPM (rev/min)	248.4	273.4	294.5	312.9	329.4	344.4	358.2	373.5	383.0	394.3
Flow rate (m³/s)	36.40	40.10	43.23	46.08	48.65	50.82	52.77	54.90	56.23	57.79
Head (m)	21.88	26.49	30.71	34.57	38.20	41.79	45.28	49.33	51.94	55.14
Jet velocity (m/s)	22.95	25.28	27.26	29.06	30.68	32.05	33.28	34.62	35.45	36.44
Nozzle dynamic head (m)	26.87	32.59	37.89	43.05	47.98	52.37	56.46	61.11	64.09	67.70
JVR = Vjet / Vship	1.840	1.832	1.820	1.786	1.756	1.764	1.782	1.805	1.821	1.841
Head recovery (m)	4.99	6.10	7.19	8.49	9.78	10.57	11.18	11.79	12.15	12.56
Inlet loss coefficient	0.130	0.130	0.130	0.130	0.130	0.130	0.130	0.130	0.130	0.130
Intake velocity (m/s)	10.60	11.73	12.73	13.83	14.85	15.44	15.87	16.30	16.55	16.83
Wake fraction, (1-w)	0.850	0.850	0.850	0.850	0.850	0.850	0.850	0.850	0.850	0.850
Ship speed (knots)	24.2	26.8	29.1	31.6	34.0	35.3	36.3	37.3	37.8	38.5
NPSH(A) (m)	14.84	15.95	17.04	18.34	19.63	20.42	21.03	21.64	22.00	22.41
NPSH(1%) (m)	8.34	10.11	11.75	13.31	14.80	16.16	17.45	18.92	19.87	21.01
Thrust deduction, t	-0.045	-0.045	-0.045	-0.045	-0.045	-0.045	-0.045	-0.045	-0.045	-0.045
Thrust (kN)	481.7	582.0	673.0	751.6	824.7	904.1	983.7	1077.4	1138.6	1213.9
Propulsive efficiency	0.668	0.669	0.672	0.679	0.686	0.684	0.680	0.675	0.672	0.667

Table 13. Breakdown of component efficiencies for D = 7.4 ft.

Power at jet, PD (kW)	9000	12000	15000	18000	21000	24000	27000	30600	33000	36000
% MCR	25%	33%	42%	50%	58%	67%	75%	85%	92%	100%
η_p	0.890	0.890	0.890	0.890	0.890	0.890	0.890	0.890	0.890	0.890
V_6/V_1	2.165	2.155	2.142	2.101	2.066	2.076	2.096	2.124	2.142	2.166
μ	0.462	0.464	0.467	0.476	0.484	0.482	0.477	0.471	0.467	0.462
η_j	0.610	0.612	0.614	0.621	0.627	0.626	0.622	0.617	0.614	0.610
η_d	1.229	1.229	1.229	1.229	1.229	1.229	1.229	1.229	1.229	1.229
η_r	1.000	1.000	1.000	1.000	1.000	1.000	1.000	1.000	1.000	1.000
PC	0.668	0.669	0.672	0.679	0.686	0.684	0.680	0.675	0.672	0.667
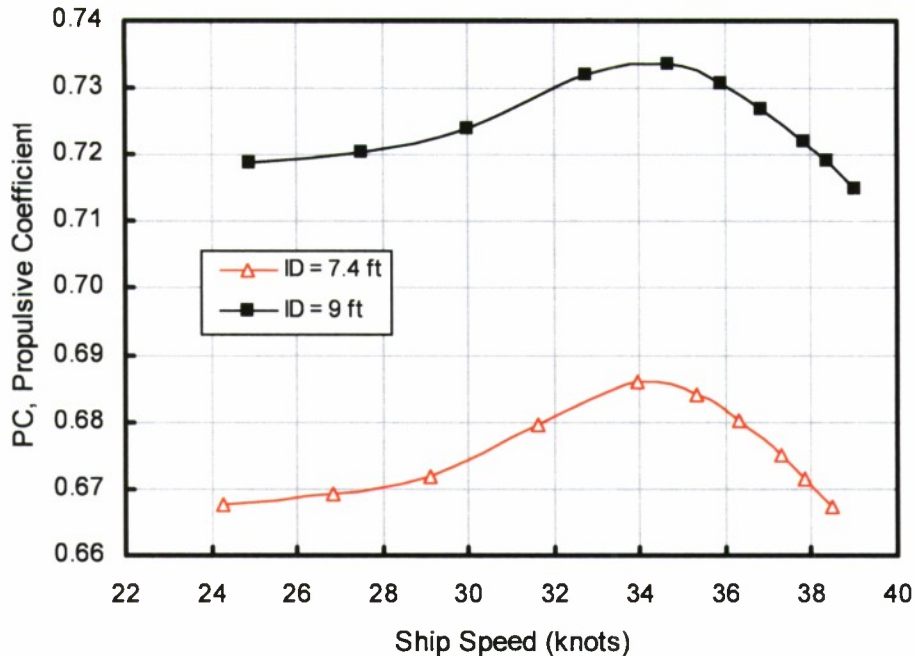
Fig. 64. Predicted propulsive coefficient for JHSS.

Modified Powering Prediction Approach

A more accurate prediction of full-scale powering can be obtained through the execution of a waterjet powering test. These tests involve a series of bare hull resistance measurements with the inlets covered, followed by a waterjet self-propulsion test in which it is critical to accurately measure the flow rate through each waterjet. The procedure for conducting a waterjet powering test was initially detailed in Scherer et al.[11] and later modified in the execution of these tests for the JHSS hull form in Jessup et al.[12]. In order to improve the accuracy of the full-scale predictions the tow tank testing can provide measured values for wake fraction (1-w), thrust deduction (1-t), inlet loss coefficient (ζ_{13}), and hull resistance. Under the ONR BAA guidance all of these values were provided, and 1-w, 1-t, and ζ_{13} were assumed constant across the speed range of the vessel. Measured model-scale hull resistance is scaled to full-scale using standard practices outlined by the ITTC. The wake fraction is Reynolds number scaled using a wake scaling procedure outlined in Scherer and Wilson[13]. Both thrust deduction and inlet loss coefficient are assumed to remain constant from model to full-scale. The omission of Reynolds number scaling from the inlet loss coefficient is a known inaccuracy in this approach as it does not account for a known reduction in frictional losses.

In order to utilize in the results of the tow tank testing in the vendor approach the inlet diameter and ratio between nozzle diameter (ITTC Station 6) and inlet diameter (ITTC Station 3) must be the same at model scale and at full scale. This insures that the values for 1-t, 1-w, and ζ_{13} are interpolated over the same scaled flow rate range as measured during the self-propulsion tests. The JHSS self-propulsion tests discussed in Scherer et al.[11] use a scaled inlet diameter of 10 ft. with nozzle diameter / inlet diameter = 0.63. The vendor powering

prediction approach is repeated with this geometry, and values for 1-t, 1-w, and ζ_{13} from both the ONR BAA and tow tank testing. In addition, both these predictions utilize the scaled tow tank hull resistance to eliminate this discrepancy. The two resistance curves, ONR BAA predicted, and tow tank measured are shown in Fig. 65. The ONR BAA prediction of JHSS hull resistance is approximately 16% greater than the scaled tow tank results across the speed range of the vessel. The authors have been unable to determine the source of these predictions. The total resistance is shown divided by the number of waterjets, with the assumption all four waterjets produce the same system thrust in straight ahead operations. Figs. 66, 67, and 68 show the ONR assumed values for 1-t, 1-w, and ζ_{13} plotted as a function of full-scale flow rate versus the values determined from tow tank self-propulsion tests. The values indicated as interpolated are generated by the vendor powering prediction utilizing the tow tank values. The values labeled as ONR BAA are generated by the vendor powering prediction utilizing the ONR BAA assumptions. On Fig. 68 is also shown the model-scale wake fraction. The full-scale or Reynolds number scaled wake fraction is determined through a wake scaling procedure discussed in Reference 13.

The results of the two vendor powering predictions are shown in Tables 14 and 15. The speed-power curves for the two vendor approach predictions and the tow tank powering prediction are shown in Fig. 69. It should be noted that the tow tank powering prediction uses an assumed pump efficiency of 0.89, equal to the values determined from pump-loop tests for the ONR AxWJ-2. The powering predictions utilizing the ONR BAA assumptions for the hull interaction coefficients, 1-t, 1-w, and inlet loss coefficient are approximately 15% lower than the tow tank prediction as shown by the dashed line. The Detail Specification, Waterjet Propulsion Systems, MIL-DTL 32334[14] indicates an uncertainty of 13% for a prediction made with only a bare hull effective horsepower model test. The fact that this prediction falls outside this range can be attributed to the large discrepancy in the thrust deduction value predicted in the ONR BAA and the measured tow tank value, Fig. 66. The 1-t value of 1.045 was likely obtained from a high speed catamaran or planning monohull, not a large displacement vessel like the JHSS. The powering prediction which incorporates the hull interaction coefficients and inlet loss coefficients from the tow tank waterjet self-propulsion test agree to within 5%, as shown by the dashed line on Fig. 69, from the towing tank prediction alone. This value is in agreement with a uncertainty of 6% for this prediction as discussed in the waterjet MilSpec[14].

As was discussed earlier the use of the self-propulsion towing tank results is limited to cases in which the inlet diameter and nozzle diameter match the waterjet size for which the vendor prediction is being used. This is a severe limitation of the tow tank powering prediction approach, as the waterjet sizing study must be conducted without the benefit of the hull interaction coefficients. A solution to this problem would be to conduct the tow tank self-propulsion tests with nozzles of various sizes effectively running over a range of jet velocity ratios. This approach was undertaken in Wilson[15] but the work focused on hull pressure distribution and documenting the changes to the inflow boundary layers not powering predictions.
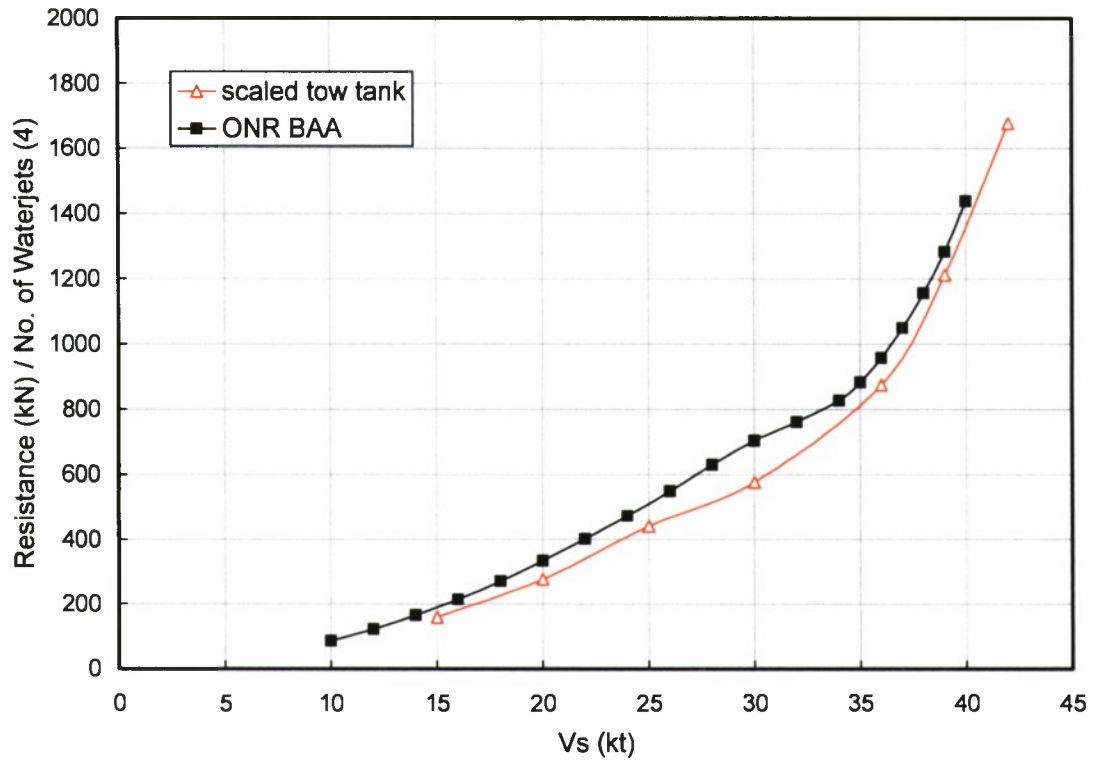
Fig. 65. JHSS resistance curves from ONR BAA and JHSS tow tank testing.
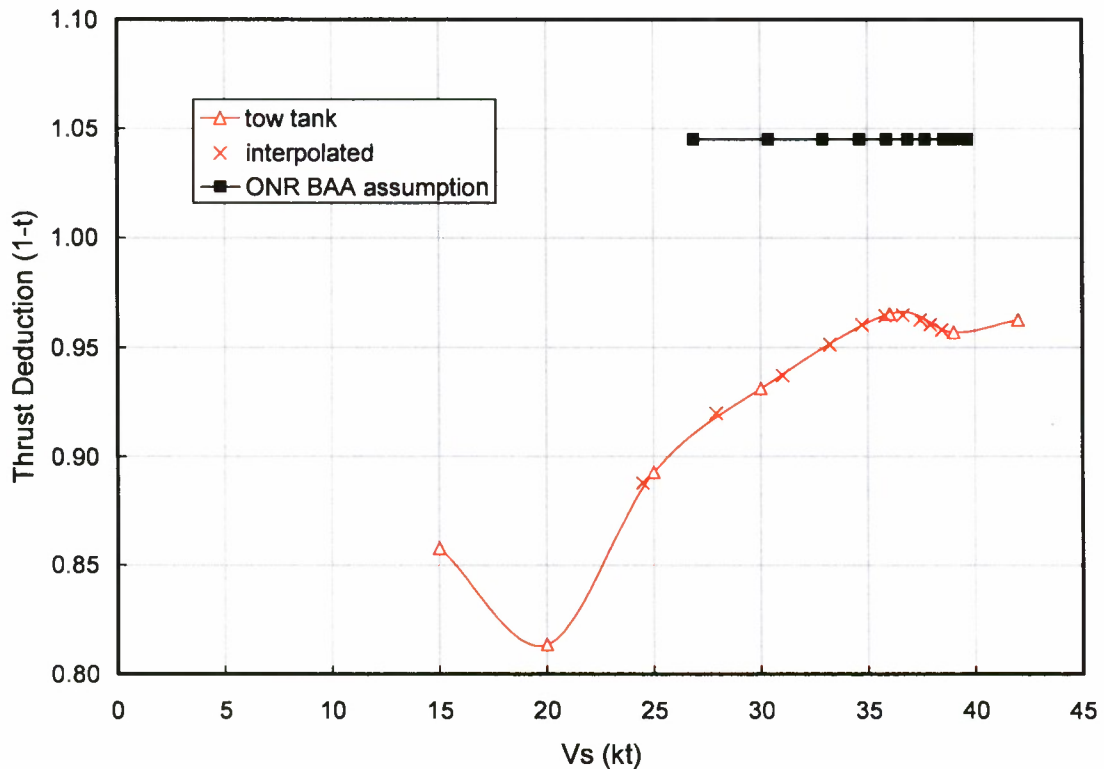

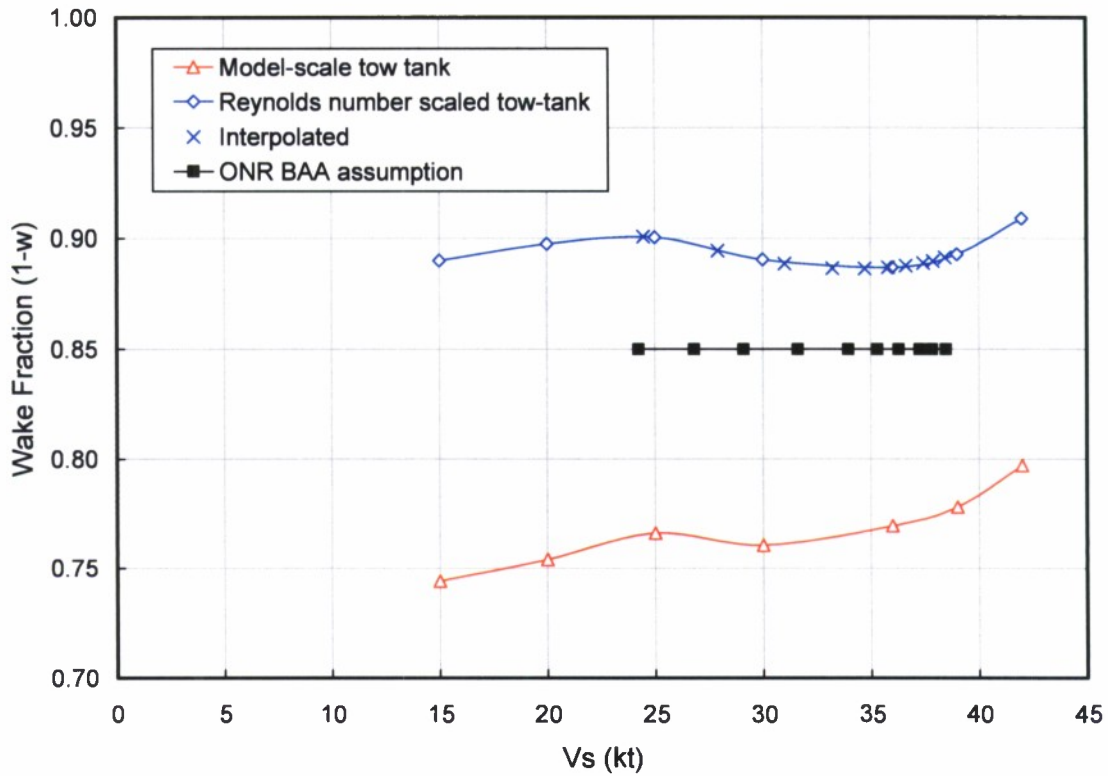**Fig. 66.** Thrust deduction, 1-*t*, from ONR BAA and tow tank testing.

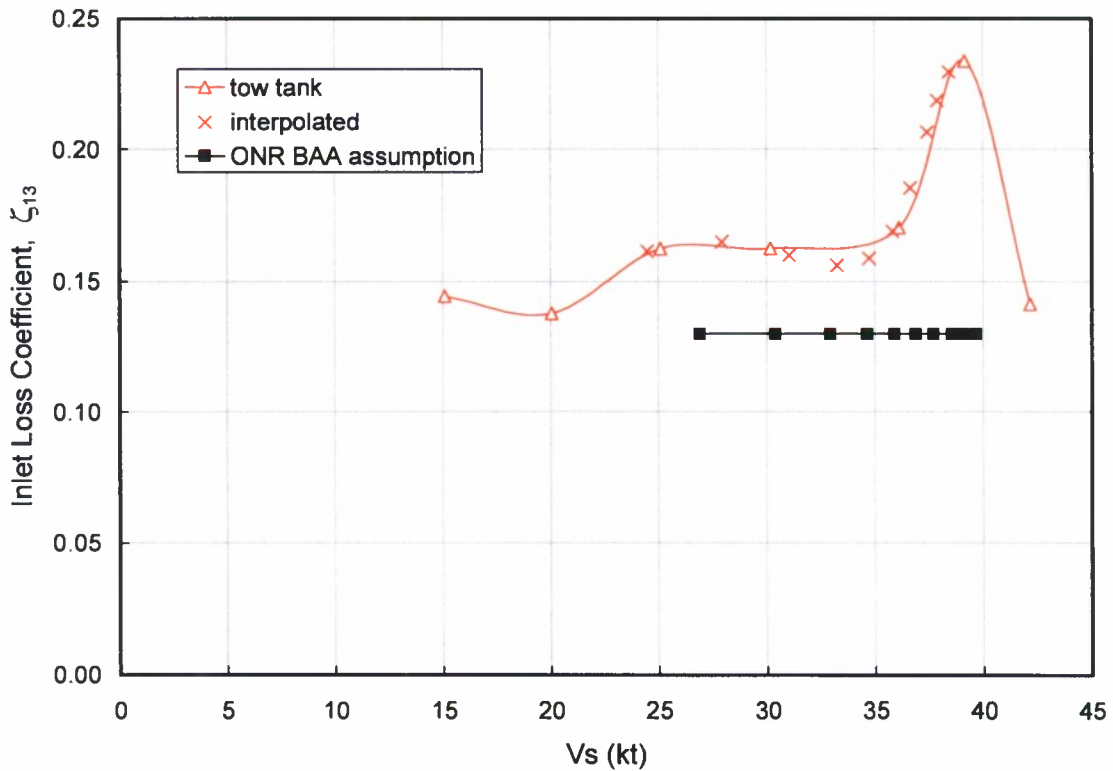**Fig. 67.** Wake Fraction, 1-*w*, from ONR BAA and tow tank testing.

Fig. 68. Inlet loss coefficient, ζ_{13}, from ONR BAA and tow tank testing.

Table 14. Powering performance for JHSS with 10 ft (3.048 m) inlet diameter pumps using ONR BAA assumptions for hull interaction coefficients.

$D_6/D_3 = 0.63$										
Power at jet, P_D (kW)	9000	12000	15000	18000	21000	24000	27000	30600	33000	36000
Percent MCR	25%	33%	42%	50%	58%	67%	75%	85%	92%	100%
4 x Power (DHP)	0.798	0.803	0.807	0.809	0.807	0.804	0.799	0.795	0.792	0.789
Flow coefficient Q*	0.807	0.812	0.813	0.811	0.808	0.805	0.802	0.799	0.797	0.795
Head coefficient H*	2.3244	2.3081	2.3043	2.3108	2.3206	2.3310	2.3408	2.3515	2.3580	2.3654
Power coefficient P*	2.1143	2.1129	2.1126	2.1131	2.1140	2.1148	2.1155	2.1163	2.1167	2.1171
Cavitation constant N*	0.9951	1.0016	1.0031	1.0005	0.9966	0.9924	0.9884	0.9840	0.9814	0.9784
Efficiency	0.887	0.887	0.887	0.887	0.887	0.888	0.888	0.888	0.888	0.888
RPM (rev/min)	150.5	165.7	178.5	189.7	199.6	208.7	217.0	226.3	232.0	238.8
Flow rate (m³/s)	57.34	63.49	68.49	72.61	76.16	79.32	82.19	85.35	87.31	89.63
Head (m)	13.86	16.68	19.32	21.88	24.34	26.72	29.02	31.68	33.40	35.50
Jet velocity (m/s)	19.80	21.92	23.65	25.07	26.30	27.39	28.38	29.47	30.15	30.95
Nozzle dynamic head (m)	19.99	24.51	28.51	32.05	35.26	38.25	41.07	44.29	46.35	48.84
JVR = Vjet / Vship	1.432	1.403	1.396	1.407	1.425	1.444	1.463	1.486	1.500	1.517
Head recovery (m)	6.13	7.83	9.19	10.17	10.92	11.53	12.05	12.61	12.94	13.34
Inlet loss coefficient	0.130	0.130	0.130	0.130	0.130	0.130	0.130	0.130	0.130	0.130
Intake velocity (m/s)	11.76	13.28	14.40	15.14	15.69	16.12	16.48	16.86	17.08	17.34
Wake fraction, (1-w)	0.850	0.850	0.850	0.850	0.850	0.850	0.850	0.850	0.850	0.850
Ship speed (knots)	26.9	30.4	32.9	34.6	35.9	36.9	37.7	38.6	39.1	39.7
NPSH(A) (m)	15.98	17.68	19.04	20.02	20.77	21.38	21.90	22.46	22.79	23.19
NPSH(1%) (m)	5.93	7.24	8.41	9.47	10.45	11.38	12.25	13.26	13.90	14.68
Thrust deduction, t	-0.045	-0.045	-0.045	-0.045	-0.045	-0.045	-0.045	-0.045	-0.045	-0.045
Thrust (kN)	494.0	587.5	678.8	772.1	865.3	957.3	1047.4	1153.1	1222.1	1306.7
Propulsive efficiency	0.759	0.765	0.766	0.764	0.761	0.757	0.752	0.747	0.744	0.740

Table 15. Powering performance for JHSS with 10 ft (3.048 m) inlet diameter pumps using tow tank values for hull interaction coefficients.

| $D_6/D_3 = 0.63$										
Power at jet, P_D (kW)	9000	12000	15000	18000	21000	24000	27000	30600	33000	36000
Percent MCR	25%	33%	42%	50%	58%	67%	75%	85%	92%	100%
4 x Power (DHP)	0.798	0.803	0.807	0.809	0.807	0.804	0.799	0.795	0.792	0.789
Flow coefficient Q*	2.3552	2.3405	2.3246	2.3195	2.3251	2.3365	2.3509	2.3678	2.3775	2.3873
Head coefficient H*	2.1165	2.1155	2.1143	2.1139	2.1143	2.1152	2.1162	2.1173	2.1178	2.1183
Power coefficient P*	0.9825	0.9885	0.9950	0.9970	0.9948	0.9902	0.9843	0.9774	0.9734	0.9693
Cavitation constant N*	0.888	0.888	0.887	0.887	0.887	0.888	0.888	0.889	0.889	0.889
Efficiency	150.5	165.6	178.5	189.6	199.6	208.7	217.0	226.2	232.0	238.8
RPM (rev/min)	0.798	0.803	0.807	0.809	0.807	0.804	0.799	0.795	0.792	0.789
Flow rate (m³/s)	56.68	62.73	67.98	72.37	76.03	79.16	81.88	84.83	86.67	88.89
Head (m)	14.03	16.90	19.48	21.95	24.39	26.78	29.14	31.89	33.67	35.82
Jet velocity (m/s)	19.57	21.66	23.47	24.99	26.25	27.33	28.27	29.29	29.93	30.69
Nozzle dynamic head (m)	19.53	23.92	28.09	31.84	35.14	38.09	40.76	43.75	45.66	48.03
JVR = Vjet / Vship	1.555	1.508	1.471	1.462	1.469	1.484	1.500	1.521	1.535	1.552
Head recovery (m)	5.50	7.03	8.61	9.89	10.76	11.31	11.63	11.86	12.00	12.21
Inlet loss coefficient	0.161	0.165	0.160	0.156	0.159	0.169	0.185	0.206	0.219	0.229
Intake velocity (m/s)	11.34	12.85	14.18	15.16	15.84	16.34	16.73	17.12	17.35	17.63
Wake fraction, (1-w)	0.901	0.894	0.889	0.887	0.886	0.887	0.888	0.889	0.890	0.891
Ship speed (knots)	24.5	27.9	31.0	33.2	34.7	35.8	36.6	37.4	37.9	38.5
NPSH(A) (m)	15.35	16.88	18.46	19.74	20.61	21.16	21.48	21.71	21.85	22.06
NPSH(1%) (m)	5.85	7.14	8.34	9.44	10.43	11.35	12.20	13.16	13.78	14.54
Thrust deduction, t	0.112	0.080	0.063	0.049	0.040	0.035	0.035	0.037	0.040	0.042
Thrust (kN)	424.6	521.3	607.1	693.9	779.6	860.3	934.9	1018.8	1072.9	1140.0
Propulsive efficiency	0.594	0.624	0.646	0.659	0.663	0.660	0.653	0.641	0.634	0.626
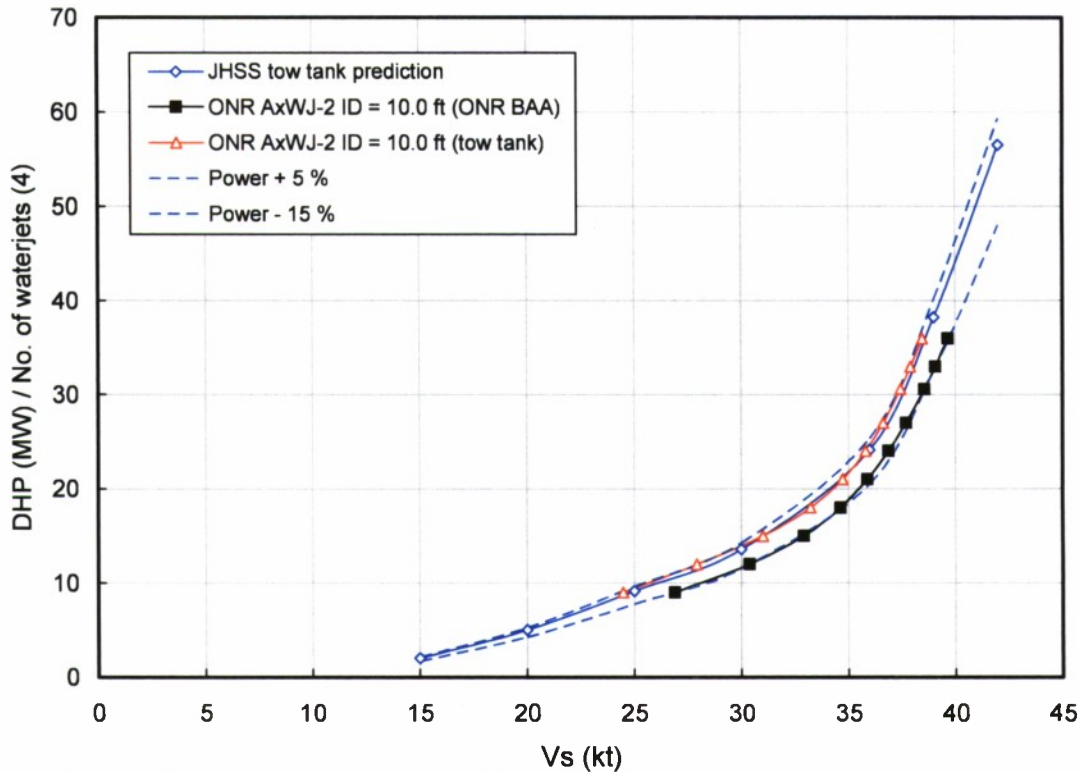
Fig. 69. Powering predictions for JHSS with 10 ft. diameter axial flow waterjets.

SUMMARY AND CONCLUSIONS

Under Phase I of ONR BAA 06-011, designs were solicited for waterjets to power the JHSS, a very large, slender, high-speed ship concept for transport of a single Marine Brigade to overseas theaters. Two vendors responded to this BAA, and the pump designs submitted were tested and evaluated at NSWCCD. The designs and data were proprietary to the vendors, and so are not available for evaluation by the wider hydrodynamic community. ONR tasked NSWCCD to design and test a new axial flow pump that would have both the geometry and the test results in the public domain. In this way, the pump could serve as a test case for pump design and analysis tools.

Pump-loop testing was performed at the 36-inch Variable Pressure Water Tunnel at NSWCCD. Lessons learned in previous pump testing were used to improve the accuracy of the water tunnel results. The water tunnel results were used to make full scale powering predictions, and were used to make comparisons to predictions of the pump operation from the RANS codes CFX and Fluent.

Testing found that the maximum pump efficiency was 0.890 ± 0.017 at a non-dimensional flow rate of Q^* $= 0.76$. Measurements of the rotor wake showed low blade losses, contributing to the good performance. Calculations with CFX matched the pump performance to within the measurement uncertainty. The predictions made using Fluent slightly exceeded the values found in testing. Calculation of thrust breakdown using CFX

yielded results that differed somewhat in the details of thrust breakdown observed in the water tunnel tests, but that matched the measured values of N^* at breakdown well.

The experimental results were used to make predictions of the performance of four 9-foot diameter pumps installed in a notional 970 foot long JHSS hull with a maximum of 36 MW available to power each pump. The predicted sustainable ship speed at 30,600 kW or 85% maximum continuous rating is 37.8 knots, 1.8 knots in excess of the required speed of 36 knots. The ship resistance curve falls completely within Zone 1, or below the Zone 1 boundary, with a cavitation margin of 5.4 knots.

As was stated in the original ONR BAA documentation, a reduction in inlet diameter would be considered favorably in the evaluation process. Additional calculations were also made of the same hull with 7.4 ft. diameter pumps. The predicted sustainable ship speed at 85% MCR with this smaller pump was 37.3 knots. The ship resistance curve crosses the Zone 1 boundary at 36 knots, just meeting the requirement of 36 knots. However, this puts the 85% MCR speed of 37.3 knots within Zone 2.

Performance of the waterjets in the JHSS hull was also calculated with a more sophisticated method utilizing tow tank results for wake fraction ($1-w$), thrust deduction ($1-t$), inlet loss coefficient (ζ_{13}), and hull resistance. Under the ONR BAA guidance all of these values were provided, and $1-w$, $1-t$, and ζ_{13} were assumed constant across the speed range of the vessel. The powering requirements predicted utilizing the tow tank results are approximately 17% higher than those predicted using the BAA specified procedure. The discrepancy is largely due to differences in the tow-tank and BAA specified values of hull resistance and thrust deduction.

Ship propulsive coefficient, PC, is a maximum on both pump sizes at about 34 to 35 kt. The propulsive coefficient is approximately 4.5 points higher for the larger pump over the entire speed range. Maximum PC for the 9 ft. pump is 73.4%, and maximum PC for the 7.4 ft. pump is 68.6%. These calculations were only performed for the tested nozzle geometry. Altering the nozzle diameter will change both the powering and cavitation performance, perhaps improving these numbers somewhat. Optimizing the nozzle diameter requires balancing the requirements for efficiency, cavitation margin, and speed. Deciding how to balance these requirements was beyond the scope of this work.

(THIS PAGE INTENTIONALLY LEFT BLANK)

APPENDIX A: STATOR INSPECTION REPORT

The geometry of the stator was measured with a computerized coordinate measurement machine (CMM) in order to quantify the fidelity of the actual blade surfaces to the specified geometry. Details of the CMM are listed in Table A1.

Table A1. Characteristics of CMM used for stator inspection.

Model	DEA Gamma 1263 with Motorized Probe
Measurement Volume	66" x 44" x 30"
Measurement Accuracy	0.0005"
Measurement Repeatability	0.0004"
Certification Method	American National Standard ASME B89, 4, 1b, 2001

The stator was prepared for measurement by first affixing the upstream face of the stator to the reference table as shown in Fig. A1. The z-axis was then established by measuring 4 points on aft end of the hub, and the x-axis was established by measuring 2 points on the x-axis of world coordinate system. The origin (x_0, y_0) was established by measuring the machined bore of propeller, and blade centerline indexing was established by rotating part coordinate system until the measurement probe aligned with the point extracted from the CAD model at 0.9R on the trailing edge.
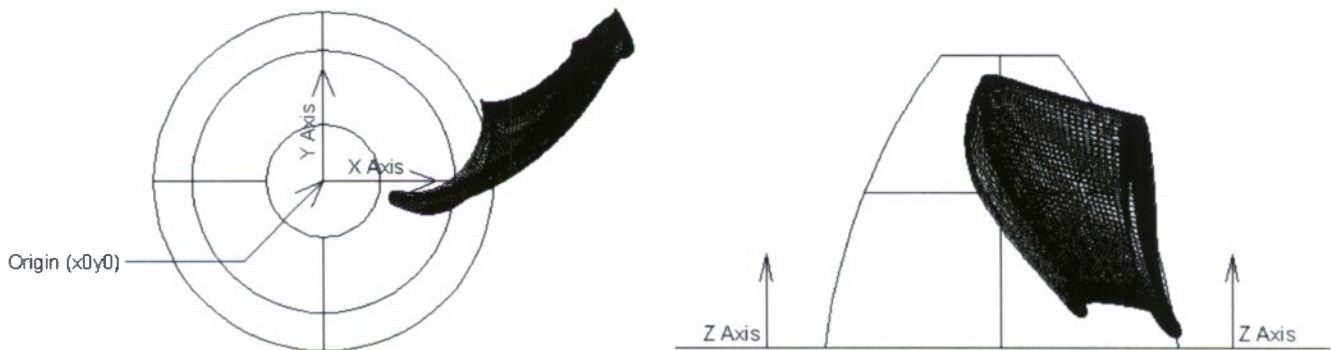

Fig. A1. Coordinate system for inspection of stator 5522.

Measurements were taken at approximately 2237 points taken on each blade. The measurements taken in 3 patches (blade surface, tip region and trailing edge) with a point density of approximately 8 per linear inch in both the spanwise and chordwise directions. The set of measurements for each blade was then rotated and translated (6 degrees of freedom) to best fit to the ideal blade surface.

The results of this inspection are summarized in Table A2. Statistics for all blades are similar, with the rms deviation from the ideal at about 0.003" on each blade, and better than 95% of all measured points within 0.005" of the ideal. Plots of the inspection results for each blade are shown in Figs. A2 – A9.

Table A2. Inspection deviations from design values.

Blade No.	Best Fit RMS Value	Maximum Deviation	Minimum Deviation	Tolerance +/-.003	Tolerance +/-.005	Tolerance +/-.007
1	.0031	+.0091	-.0084	71.684%	96.382%	99.777%
2	.0026	+.0070	-.0080	82.566%	98.480%	99.955%
3	.0026	+.0077	-.0076	82.968%	98.525%	99.911%
4	.0027	+.0085	-.0073	79.526%	97.541%	99.911%
5	.0031	+.0085	-.0053	72.195%	95.351%	99.508%
6	.0031	+.0144	-.0072	78.335%	97.717%	99.150%
7	.0029	+.0152	-.0063	87.104%	97.717%	99.105%
8	.0028	+.0134	-.0058	88.541%	97.941%	98.980%

All values in inches

Pressure Side   Suction Side

Fig. A2. Inspection results for stator blade 1.

Pressure Side   Suction Side

Fig. A3. Inspection results for stator blade 2.

Fig. A4. Inspection results for stator blade 3.

Fig. A5. Inspection results for stator blade 4.

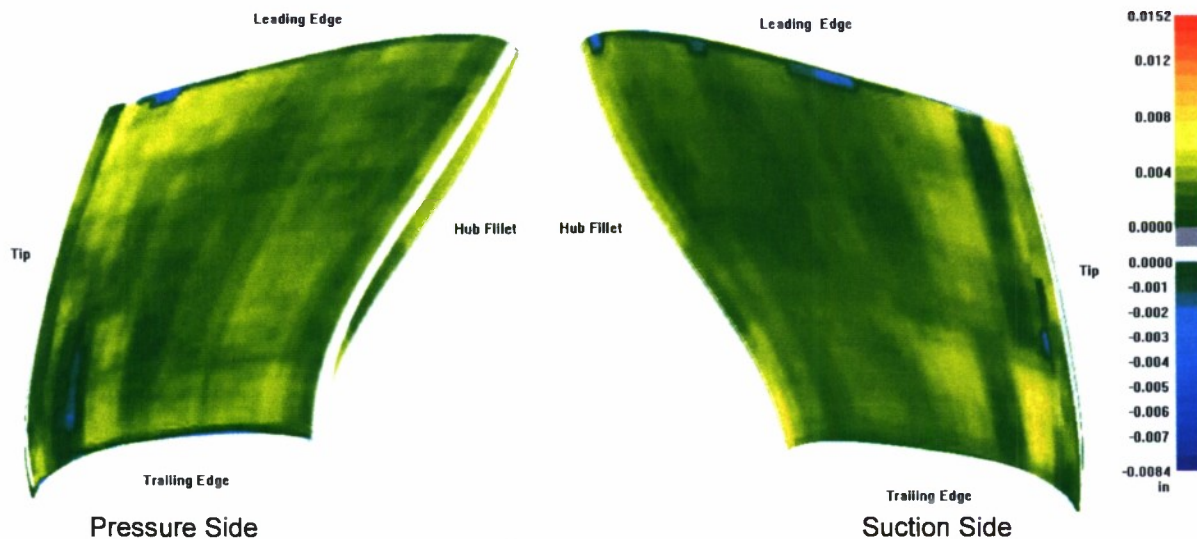**Fig. A6.** Inspection results for stator blade 5.
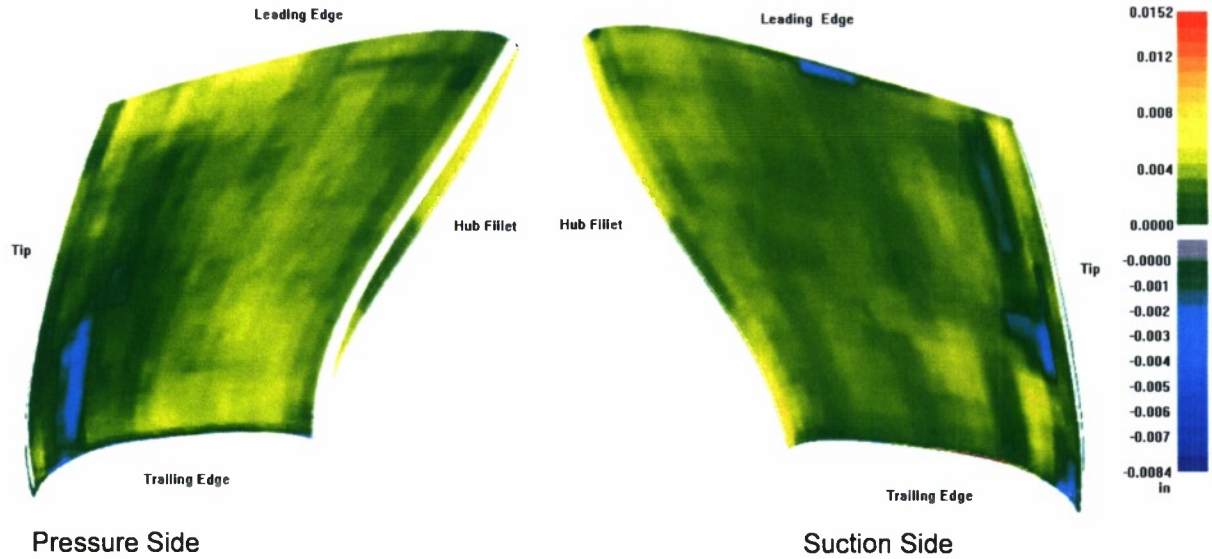

Fig. A7. Inspection results for stator blade 6.

Fig. A8. Inspection results for stator blade 7.

Fig. A9. Inspection results for stator blade 8.

REFERENCES

1   Office of Naval Research, "ONR BAA Announcement # 06-011," Arlington, VA, March 2006.

2   Michael, T. J., Schroeder, S. D., and Becnel, A. J., "Design of the ONR AxWJ-2 Axial Flow Water Jet Pump," NSWCCD-50-TR-2008/066, November, 2008.

3   ITTC 1996, "ITTC Quality Manual for High Speed Marine Vehicles, Waterjets," 21st International Towing Tank Conference, Bergen and Trondheim Norway, 1996.

4   Van Terwisga, T., "Report of the Specialist Committee on Validation of Waterjet Test Procedures" Proceedings 24th International Towing Tank Conference; II:471-508, 2005.

5   "ANSYS ICEM CFD 12.0 User Manual," ANSYS, Inc., April 2009.

6   "Fluent 6.3 User's Guide," Fluent, Inc., September 2006.

7   Brewton, S., Gowing, S., and Gorski, J., "Performance Predictions of a Waterjet Rotor and Rotor/Stator Combination Using RANS Calculations," 26th Symposium on Naval Hydrodynamics, September 2006.

8   Michael, T. J., and Chesnakas, C. J., "Advanced Design, Analysis, and Testing of Waterjet Pumps," 25th Symposium on Naval Hydrodynamics, St. Johns, Newfoundland, 8-13 August 2004.

9   Turbomachinery Society of Japan, "Guideline for Prediction and Evaluation of Cavitation Erosion in Pumps", TSJ G 001, 2003.

10   American Society of Testing and Materials, "Test Method for Cavitation Erosion Using Vibratory Apparatus," ASTM G32, West Conshhohocken, PA, 2009.

11   Scherer, J., Mutnick, I, and Lanni, F., " Procedure for Conducting a Towing Tank Test of a Waterjet Propelled Craft Using Laser Doppler Velocimetry to Determine Momentum and Energy Flux, American Towing Tank Conference, July, 2001.

12   Jessup, S., Donnelly, M., Fry, D., Cusanelli, D., and Wilson, M., "Performance Analysis of a Four Waterjet Propulsion System for a Large Sealift Ship," 27th Symposium on Naval Hydrodynamics, Seoul, Korea, October 5-10 2008.

13   Scherer, J. and Wilson, M., "Waterjet Inlet Wake Scaling," NSWCCD-50-TR-2008/051, Oct 2008.

14   MIL-DTL 32334, "Detail Specification, Waterjet Propulsion Systems" 10 September 2009.

15   Wilson, M., "Analysis of Hull Boundary Layer Velocity Distributions With and Without Active Waterjet Inlets," Waterjet Propulsion IV, RINA, London, England, 26 and 27 May 2004.

INITIAL DISTRIBUTION

Organization	Name	Copies
ONR 331	K. Kim	1
NAVSEA 05Z	J. Schumann	2
DTIC		1

CENTER DISTRIBUTION

Code	Name	Copies
3452	NSWCCD Library	pdf only
5030	S. Jessup	1
5050	A. Reed	1
5060	D. Walden	1
5500	A. Becnel	1
5700	M. Ebert	1
	Y. Lee	1
5800	C. Chesnakas	2
	M. Donnelly	1
	D. Fry	1
	S. Gowing	1
	R. Hurwitz	pdf only
	D. Pfitsch	1
	S. Schroeder	1
	M. Wilson	1
	Files	2